NATIONAL TECHNICAL UNIVERSITY OF ATHENS

School of Electrical and Computer Engineering

Division of Electromagnetics, Electrooptics
and Electronic Materials

Electromagnetic fields and applications for anisotropic/photonic structures

DOCTORAL DISSERTATION

KONSTANTINOS KATSINOS
National Technical University of Athens

SUPERVISOR: JOHN A. ROUMELIOTIS
Professor Emeritus / National Technical University of Athens

ATHENS, GREECE 2021

Ευρωπαϊκή Ένωση
European Social Fund

Operational Programme
Human Resources Development,
Education and Lifelong Learning
Co-financed by Greece and the European Union

ΕΣΠΑ
2014-2020
ανάπτυξη - εργασία - αλληλεγγύη

NATIONAL TECHNICAL UNIVERSITY OF ATHENS

School of Electrical and Computer Engineering

*Division of Electromagnetics, Electrooptics
and Electronic Materials*

Electromagnetic fields and applications for anisotropic/photonic structures
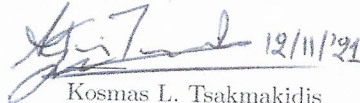
DOCTORAL DISSERTATION

KONSTANTINOS KATSINOS

National Technical University of Athens

Three-member doctoral scientific committee:
John A. Roumeliotis (Supervisor)
Elias N. Glytsis
George J. Fikioris

Approved by the seven-member doctoral scientific committee. Athens, 9th of November 2021.

Ilias Glytsis Ilias Glytsis 12.11.2021 18:30	Georgios Fikioris Georgios Fikioris 11.11.2021 18:07	ΝΤσιτσας 14/11/2021
Elias N. Glytsis	George J. Fikioris	Nikolaos L. Tsitsas
Professor / N.T.U.A.	*Professor / N.T.U.A.*	*Associate Professor / A.U.Th*
12/11/'21	Athanasios Panagopoulos Athanasios Panagopoulos 12.11.2021 13:43	IOANNIS TIGKELIS Digitally signed by IOANNIS TIGKELIS Date: 2021.11.14 15:29:42 +02'00'
Kosmas L. Tsakmakidis	Athanasios D.	Ioannis G. Tigelis
Assistant Professor / N.K.U.A.	Panagopoulos	*Professor / N.K.U.A.*
NIKOLAOS PAPANIKOLAOU Digitally signed by NIKOLAOS PAPANIKOLAOU Date: 2021.11.12 17:35:56 +02'00'	*Professor / N.T.U.A.*	
Nikolaos Papanikolaou		
Researcher / NCSR "Demokritos"		

Athens, 9th of November 2021

—————

Konstantinos Katsinos
Electrical and Computer Engineer, NTUA

Abstract

The topic of this doctoral dissertation is oriented in two directions: the first one includes the designing of a novel dual band implantable antenna for biomedical telemetry applications. The second is in the direction of developing computational techniques for the solution of electromagnetic problems that contain anisotropic materials, such as scattering from anisotropic cylinder, extraction of cutoff wavenumbers for metallic waveguides, with anisotropic infills and the calculation of the whispering gallery mode frequencies (WGM) for the case of a cylindrical resonator.

In the first chapter of this dissertation a novel dual band implantable antenna is designed, for biomedical telemetry purposes. More specifically, the antenna is intended to be implanted inside the human chest, i.e. for pacemaker applications. In order to design the implantable antenna, a 3-layer canonical human chest model was used as an implantation cite. Moreover the HFSS commercial software was used in order to simulate the antenna's performance under the aforementioned situation. The designed antenna is able to operate in two different frequency bands, so it permits the use of wake up and sleep signals in order to extend the battery's lifetime. Another key fact about the designed antenna are the various degrees of freedom that it provides, so the ability to be used in other biomedical applications (retinal implants applications, intracranial pressure monitoring etc), with minimal modification in its design. Furthermore, an extensive comparative study was performed taking into account all the possible combinations of the miniaturization techniques, showing the miniaturization limits of each one of them.

In the second chapter, a coupled-field volume integral equation (CFVIE) method for electromagnetic (EM) scattering on electrically large, highly inhomogeneous gyrotropic circular cylinders, under normal incidence, is developed. The CFVIEs are solved by cylindrical Dini series expansion (CDSE) method where the unknown fields are expanded by entire domain orthogonal vectorial basis functions. The

main advantage of the present method is that it permits the scatterer to have continuously varying highly inhomogeneous gyrotropic characteristics, i.e., the constitutive parameters of the cylinder can be highly inhomogeneous in both gyroelectric and gyromagnetic tensors. Initially the two-dimensional (2-D) Green's function (GF) is expanded in a tensorial form, using the cylindrical vector wave functions (CVWFs). Then, by employing the CDSE for the unknown fields, the 2-D volumetric integrals are carried out analytically, reducing the CFVIEs to a set of algebraic equations. The method is validated by comparisons of the exact solution based on the separation of variables method (SVM) for homogeneous isotropic/gyroelectric/gyromagnetic cylinders, with HFSS commercial software for two- and three-layered gyroelectric/gyromagnetic cylinders, as well as with the recently developed hybrid projection method (HPM) for electrically large continuously varying highly inhomogeneous isotropic cylinders. Results for combined gyroelectric-continuously varying highly inhomogeneous isotropic cylinders are presented and discussed.

In the third chapter, a coupled-field volume integral equation (CFVIE) method is developed for the calculation of the normalized cutoff wavenumbers of circular metallic walled waveguides, having concentric continuously varying highly inhomogeneous gyrotropic (i.e., gyroelectric and gyromagnetic) infill. The normalized cutoff wavenumbers are obtained as the roots of a determinantal equation, formed by solving the CFVIEs using the cylindrical Dini series expansion (CDSE) method, where the unknown fields inside the waveguide are expanded by entire domain orthogonal Dini-type vectorial basis functions. To account for the electric boundary condition (BC) on waveguide's circular perfect electric conducting (PEC) surface, two modified two-dimensional (2-D) tensorial Green's functions (GFs), expanded in cylindrical vector wave functions (CVWFs), are employed in the kernels of the CFVIEs. These modified 2-D tensorial GFs are constructed by enforcing, on their dyadic form, the satisfaction of the electric boundary condition. The CDSE, along with the modified 2-D tensorial GFs, allow for the analytical integration of the volumentric-type integrals and the reduction of the CFVIEs to a set of algebraic equations. We exhaustively demonstrate the validity of the CFVIE-CDSE by a series of comparisons on the normalized cutoff wavenumbers: we firstly construct the solutions for obtaining the normalized cutoff wavenumbers in homogeneous gyrotropic waveguides by the separation of variables method (SVM), and secondly we employ HFSS commercial software for two-layered isotropic and three-layered gyroelectric loaded waveguides. We characterize the type of modes, i.e., TE/TM or hybrid HE/EH, for each configuration presented, and discuss the efficiency of the CFVIE-CDSE method.

In the fourth chapter, asymptotic closed-form expressions for the calculation of the complex TE/TM whispering gallery mode (WGM) frequencies in homogeneous gyroelectric circular cylindrical resonators of infinite length, are derived. In addition, we extend a recently developed volume integral equation-cylindrical Dini series expansion (VIE-CDSE) method, so as to support the prediction of the complex WGMs for continuously varying highly inhomogeneous gyroelectric circular cylindrical resonators. To this end, VIE's entire domain orthogonal vectorial basis is extended to support, via asymptotic closed-form expressions, very large indices of the involved Dini-type cylindrical vector wave functions (CVWFs). This way, the eigenbasis required for the solution of the VIE becomes free of numerical instabilities, arising when very large orders of the involved Bessel functions are employed. The complex frequencies obtained by the asymptotic closed-form expressions for the case of the homogeneous gyroelectric resonator, as well as those obtained by the

VIE, when the multilayered gyroelectric resonator is reduced to one layer, are validated by comparisons with the complex roots extracted by numerically solving the TE/TM characteristic equations, obtained from the separation of variables method (SVM), using complex root finding techniques. We demonstrate the calculation of very high order WGM frequencies for cylindrical resonators composed of homogeneous and highly inhomogeneous permittivity profiles. This asymptotic theory constitutes a rigorous tool, which may serve for verification of method of analytical regularisation (MAR)-based numerical solutions for other non-circular inhomogeneous cylinders, and the interpretation of experimental data for applications such as WGM lasing, refractometric sensing, and magneto-optic coupling.

Key Words: Electromagnetism, Anisotropic Materials, Scattering, Photonics, Waveguides, Cutoff Wavenumbers, Antennas, Biomedical Telemetry

Abstract in greek

Η παρούσα διδακτορική διατριβή χωρίζεται σε δύο μέρη. Το πρώτο μέρος αφορά τον σχεδιασμό κεραίας με σκοπό την εμφύτευση της σε περιβάλλον ανθρώπινου ιστού. Πιο συγκεκριμένα, η κεραία προορίζεται για την ενσωμάτωση της σε εφαρμογές τύπου βηματοδότη, δηλαδή σε εφαρμογές που έχουν ως περιβάλλον την μορφολογία του ανθρώπινου στήθους. Επιπλέον πραγματοποιείται εκτενής συγκριτική μελέτη όλων των συνδυασμών των τεχνικών σμίκρυνσης που αναφέρονται στην βιβλιογραφία, προκειμένου να εξαχθεί ένας οδηγός για τους σχεδιαστές εμφυτεύσιμων κεραιών, όσον αφορά τις δυνατότητες σμίκρυνσης που προσφέρει ο κάθε συνδυασμός και επομένως να διευκολύνει την διαδικασία σχεδίασης.

Το δεύτερο, και κύριο μέρος, της διδακτορικής διατριβής πραγματεύεται την επίλυση ηλεκτρομαγνητικών (ΗΜ) προβλημάτων διαφόρων τύπων. Αρχικά, αναπτύχθηκε μια μέθοδος με σκοπό τον υπολογισμό του σκεδαζόμενου ηλεκτρομαγνητικού πεδίου από κυλινδρικούς σκεδαστές, με άπειρο μήκος. Κύριος πυλώνας της μεθόδου αυτής αποτέλεσε η χρήση των Coupled Fields Volume Integral Equations (CFVIEs),καθώς και η ανάπτυξη των άγνωστων πεδίων σε αναπτύγματα τύπου Δινι. Η μέθοδος αυτή μπορεί να χειριστεί με ευκολία ηλεκτρικά μεγάλες διατάξεις, οι οποίες αποτελούνται από ισοτροπικά/ανισοτροπικά υλικά, ακόμη και με υψηλή ανομοιογένεια. Στην συνέχεια, αναπτύχθηκε υπολογιστική μέθοδος για την εξαγωγή των κυματαριθμών αποκοπής για την περίπτωση του κυλινδρικού κυματοδηγού κυκλικής διατομής, με μεταλλικά τοιχώματα. Η μέθοδος αυτή, επίσης, στηρίχθηκε στις CFVIEs καθώς και στα αναπτύγματα τύπου Dini. Τέλος, αναπτύχθηκε ασυμπτωτική μέθοδος για τον υπολογισμό των μιγαδικών συντονισμών των Whispering Gallery Modes (WGM) για την περίπτωση κυλινδρικού συντονιστή. Για την εξαγωγή των ασυμπτωτικών εκφράσεων χρησιμοποιήθηκε η συνάρτηση Airy.

Λέξεις Κλειδιά: Ηλεκτρομαγνητισμός, Ανισοτροπικά Υλικά, Σκέδαση, Φωτονικά, Κυματοδηγοί, Συχνότητες Αποκοπής, Κεραίες, Βιοϊατρική Τηλεμετρία

Extended Abstract in greek

Το αντικείμενο της παρούσας διδακτορικής διατριβής χωρίζεται σε δύο κύριες κατηγορίες. Η πρώτη αφορά την μελέτη και σχεδίαση μιας πρωτότυπης μικροσκοπικής κεραίας, η οποία προορίζεται για εμφύτευση εντός του ανθρώπινου σώματος, με κύριο σκοπό την επίτευξη τηλεμετρίας μεταξύ μιας συσκευής η οποία βρίσκεται εντός βιολογικού ιστού και μιας συσκευής παρακολούθησης/ελέγχου, η οποία βρίσκεται εκτός τους ανθρώπινου σώματος. Επιπλέον πραγματοποιείται μια συγκριτική μελέτη όλων των τεχνικών σμίκρυνσης και των πλεονεκτημάτων τους που χρησιμοποιούνται κατά την σχεδίαση κεραιών, οι οποίες έχουν ως απώτερο σκοπό την λειτουργία τους σε περιβάλλον όπου ο χώρος είναι περιορισμένος. Η δεύτερη κατηγορία αφορά την ανάπτυξη πρωτότυπων ημι-αναλυτικών και ασυμπτωτικών μεθόδων οι οποίες εφαρμόζονται σε προβλήματα όπου η βασική γεωμετρία είναι κυλινδρική με κυκλική διατομή και άπειρο μήκος. Αφετηρία για όλες τις ανωτέρω μεθόδους που αναπτύχθηκαν αποτέλεσε η ευρέως γνωστή electric field volume integral equation (EFVIE) καθώς και η coupled field volume integral equation (CFVIE). Ο απώτερος σκοπός της ανάπτυξης αυτών των μεθόδων είναι η κατανόηση φυσικών φαινομένων, καθώς και η εφαρμογή τους για την ανάπτυξη νέων καινοτόμων εφαρμογών στον τομέα της φωτονικής, των νανο-κεραιών, της νανο-φυσικής, των οπτικών ινών κ.λπ.

Στο πρώτο κεφάλαιο γίνεται μια σύντομη εισαγωγή στις βασικές έννοιες των κεραιών, καθώς και στις παραμέτρους οι οποίες έχουν σημαίνοντα ρόλο κατά την μελέτη και αξιολόγηση μιας κεραίας. Επιπλέον, γίνεται μια εκτενής αναφορά στις εφαρμογές και στον τρόπο με τον οποίο οι εμφυτεύσιμες διατάξεις έχουν εισχωρήσει στην ανθρώπινη ζωή, με απώτερο σκοπό την βελτίωση της όσον αφορά τις παροχές που παρέχονται στους ασθενείς. Επίσης, γίνεται μια σύντομη αναδρομή στις μπάντες συχνοτήτων που χρησιμοποιούνται για την διάδοση δεδομένων, που σχετίζονται με εμφυτεύσιμες διατάξεις και αναφέρονται περισσότερες λεπτομέρειες για τις κυριότερες εξ 'αυτών, που είναι οι ISM, WMTS και η MedRadio. Ιδιαίτερη έμφαση, στο κεφάλαιο

αυτό δίνεται στις προκλήσεις με τις οποίες ερχόμαστε αντιμέτωποι κατά την σχεδίαση κεραιών, οι οποίες προορίζονται για την λειτουργία τους σε ευαίσθητα περιβάλλοντα, όπως είναι αυτό του ανθρώπινου ιστού. Πιο συγκεκριμένα, οι κυριότερες προκλήσεις αφορούν την επίτευξη βιοσυμβατότητας ούτως ώστε να αποφευχθεί η απόρριψη της συσκευής/κεραίας από τον οργανισμό, η επίτευξη μικρής διάστασης διότι ο χώρος είναι περιορισμένος, η χαμηλή κατανάλωση ισχύος ώστε να παραταθεί η διάρκεια ζωής της κεραίας και να ελαττωθούν οι χειρουργικές επεμβάσεις, με σκοπό την αντικατάσταση της μπαταρίας τροφοδοσίας της συσκευής, το κέρδος (gain) της κεραίας, το εύρος ζώνης λειτουργίας (bandwidth) της κεραίας καθώς και ο ρυθμός ειδικής απορρόφησης (specific absorption rate, SAR). Αξίζει να τονιστεί ότι έχουν θεσπιστεί κατάλληλα πρότυπα για τον ρυθμό ειδικής απορρόφησης από την IEEE, τα οποία πρέπει να πληρούν οι κεραίες προκειμένου να διαφυλάσσεται η ασφάλεια του ασθενούς και να αποτρέπεται οποιαδήποτε επιπλοκή.

Εν συνεχεία παρουσιάζονται λύσεις στα προβλήματα/προκλήσεις που αναφέρθηκαν ανωτέρω. Η χρήση βιοσυμβατών υλικών τόσο για την κατασκευή της κεραίας, όσο και η χρήση βιοσυμβατού κελύφους για την εμφώλευση της κεραίας, στην περίπτωση που δεν είναι κατασκευασμένη με βιοσυμβατά υλικά, είναι οι δύο ευρύτερα διαδεδομένες τεχνικές για την επίτευξη την πολυπόθητης βιοσυμβατότητας. Όσον αφορά την σμίκρυνση των διαστάσεων της κεραίας, αναφέρονται στην βιβλιογραφία πληθώρα τέτοιων τεχνικών, όπως η χρήση διηλεκτρικού υποστρώματος και υπερ-στρώματος με υψηλή διηλεκτρική σταθερά, η χρήση αγωγού βραχυκύκλωσης, η χρήση πολλαπλών ακτινοβολητών και η επέκταση του μήκους ροής του ρεύματος.

Σύντομη αναφορά πραγματοποιείται για τον τρόπο με τον οποίο κατασκευάζονται αυτές οι κεραίες, καθώς και για την διαδικασία με την οποία μετρούνται τα χαρακτηριστικά ακτινοβολίας τους. Επιπλέον, αναφέρονται οι πειραματικές διατάξεις που χρησιμοποιούνται για την μελέτη των χαρακτηριστικών ακτινοβολίας της κεραίας ούτως ώστε να προσομοιάζουν τις πραγματικές συνθήκες κάτω από τις οποίες θα κληθεί να λειτουργήσει η κεραία.

Ιδιαίτερη έμφαση δίνεται στην γεωμετρία των σχεδιαστικών μοντέλων που προσομοιάζουν τον ανθρώπινο ιστό και χρησιμοποιούνται στο στάδιο της σχεδίασης της κεραίας, με την χρήση κατάλληλων λογισμικών πακέτων. Στην παρούσα διδακτορική διατριβή χρησιμοποιήθηκε εξ ολοκλήρου το λογισμικό πακέτο HFSS της ANSYS. Τα μοντέλα αυτά χωρίζονται σε δυο μεγάλες κατηγορίες, στα κανονικά μοντέλα (canonical models) και στα ανατομικά μοντέλα (anatomical models).Τα κανονικά μοντέλα αποτελούνται από απλουστευμένες διατάξεις, όπως για παράδειγμα κύβους ή σφαίρες, οι οποίες προσομοιάζουν το εκάστοτε μέλος του ανθρώπινου ιστού που ενδιαφέρει την εφαρμογή (στήθος, οφθαλμός, κρανίο κ.α.). Στα μοντέλα αυτά μπορούμε να εισάγουμε όση περισσότερη λεπτομέρεια επιθυμούμε, ούτως ώστε να αυξηθεί η ακρίβεια των αποτελεσμάτων μας και να πλησιάσουν εξαιρετικά αυτά των ανατομικών μοντέλων, καθώς και των πραγματικών μετρήσεων που θα λάβουμε στο στάδιο της υλοποίησης και μέτρησης της κεραίας. Τα ανατομικά μοντέλα παρέχουν αυξημένη ακρίβεια υπολογισμού, διότι περιλαμβάνουν μια πολύ αναλυτική περιγραφή της δομής του ανθρώπινου ιστού αλλά απαιτούν ασύγκριτα μεγαλύτερη υπολογιστική ισχύ συγκριτικά με τα κανονικά μοντέλα. Για τον λόγο αυτό στην βιβλιογραφία υπάρχει πληθώρα εργασιών οι οποίες πραγματοποιούν τις προσομοιώσεις τους σε κανονικά μοντέλα, τα οποία έχουν εμπλουτίσει με επιπλέον πληροφορία, σχετικά με τα στρώματα του ανθρώπινου ιστού (μύες, λίπος, οστό, δέρμα κ.α.), έτσι ώστε να μην είναι απαραίτητη εξαιρετικά μεγάλη υπολογιστική ισχύς, καθώς και για να επιταχυνθεί ταχύτητα εκτέλεσης των προσομοιώσεων.

Το κεφάλαιο συνεχίζεται με την απεικόνιση των μοντέλων κάτω από τις οποίες πραγματοποιήθηκε η σχεδίαση της κεραίας. Όπως είναι εμφανές, αρχικά χρησιμοποι-

ήθηκε ένα απλούστερο μοντέλο με σκοπό τον πρόχειρο υπολογισμό των παραμέτρων της κεραίας. Εν συνεχεία, το μοντέλο εμπλουτίστηκε με επιπλέον πληροφορία, ούτως ώστε να αυξηθεί η ακρίβεια των τελικών αποτελεσμάτων. Επίσης, παρουσιάζεται το πρωτότυπο μοντέλο της κεραίας και αναφέρονται οι παράμετροι σχεδίασης της, προκειμένου να επιτευχθούν οι βέλτιστες παράμετροι ακτινοβολίας. Αξίζει να σημειωθεί ότι λόγω του μεγάλου αριθμού βαθμών ελευθερίας που παρουσιάζει η κεραία, πραγματοποιήθηκε τεράστιος αριθμός παραμετρικών προσομοιώσεων, προτού καταλήξουμε στις τελικές τιμές των παραμέτρων. Στην συνέχεια παρουσιάζονται φωτογραφίες που απεικονίζουν το πραγματικό μέγεθος της κεραίας, η οποία αποτελεί μια εκ των μικρότερων στην βιβλιογραφία. Ένα από τα καίρια πλεονεκτήματα της προτεινόμενης κεραίας πέρα από το πολύ μικρό μέγεθος της, το οποίο της επιτρέπει να χρησιμοποιηθεί σε εφαρμογές όπου ο χώρος είναι περιορισμένος (π.χ. οφθαλμός) είναι η δυνατότητα της να λειτουργεί σε δύο μπάντες συχνοτήτων. Το γεγονός αυτό δίνει την δυνατότητα στην κεραία να λειτουργεί με wake up και sleep σήματα. Πιο αναλυτικά, η κεραία μπορεί να θέτει την εμφυτευμένη συσκευή σε κατάσταση ύπνου, άρα και μηδενικής κατανάλωσης ενέργειας, μέσω ενός σήματος στην MedRadio μπάντα και να την ενεργοποιεί μόνο όταν είναι απαραίτητο, για την λήψη κάποιων δεδομένων, με ένα σήμα στην ISM μπάντα. Έτσι, παρατείνεται η διάρκεια ζωής της μπαταρίας, με αποτέλεσμα να μειώνεται η ανάγκη για πραγματοποίηση χειρουργικών επεμβάσεων με σκοπό την αντικατάσταση της μπαταρίας τροφοδοσίας. Η επίτευξη αυτής της λειτουργίας οφείλεται στην εισαγωγή κατάλληλων προεξοχών, οι οποίες μέσω παραμετρικών προσομοιώσεων συντονίζουν στην κατάλληλη συχνοτική περιοχή. Τέλος, απεικονίζονται κατάλληλα διαγράμματα, τα οποία αποδεικνύουν αυτή την λειτουργία της, καθώς και τα χαρακτηριστικά ακτινοβολίας της.

Στο δεύτερο κεφάλαιο μελετάται η σκέδαση ηλεκτρομαγνητικών κυμάτων από έναν απέραντο κύλινδρο κυκλικής διατομής, ο οποίος έχει διαφορετικές συντακτικές παραμέτρους από τον περιβάλλοντα χώρο στον οποίο βρίσκεται. Για την επίλυση του προβλήματος χρησιμοποιείται η electric field volume integral equation (EFVIE) σε πρώτο στάδιο, καθώς και η coupled field volume integral equation (CFVIE). Έχουν ληφθεί υπόψη και οι δύο πολώσεις του προσπίπτοντος ηλεκτρομαγνητικού κύματος, το οποίο προσπίπτει κάθετα στην διάταξη. Οι CFVIEs λύνονται με την χρήση κυλινδρικών αναπτυγμάτων τύπου Dini, όπου τα άγνωστα πεδία αναπτύσσονται σε ορθογώνιες διανυσματικές συναρτήσεις βάσης. Το κύριο πλεονέκτημα της μεθόδου που αναπτύχθηκε είναι ότι επιτρέπει στον σχεδιαστή να έχει γυροτροπικά χαρακτηριστικά συνεχούς μεταβολής, υψηλής ανομοιογένειας, δηλαδή οι συντακτικές παράμετροι του κυλίνδρου μπορούν να είναι υψηλής ανομοιογένειας, τόσο στον γυροηλεκτρικό όσο και στον γυρομαγνητικό τανυστή που τις περιγράφει. Αρχικά η δισδιάστατη συνάρτηση Green αναπτύχθηκε σε τανυστική μορφή, με την χρήση των διανυσματικών κυματικών κυλινδρικών συναρτήσεων. Ύστερα, χρησιμοποιώντας το ανάπτυγμα της σειράς Dini σε κυλινδρικές συντεταγμένες για τα άγνωστα πεδία, μπορούμε να υπολογίσουμε αναλυτικά τα δισδιάστατα ολοκληρώματα υποβαθμίζοντας τις CFVIEs σε ένα σύνολο από αλγεβρικές εξισώσεις. Τα αποτελέσματα της μεθόδου που αναπτύχθηκε εξετάστηκαν ενδελεχώς μέσω συγκρίσεων με την αναλυτική λύση, η οποία βασίζεται στον χωρισμό των μεταβλητών για ομογενείς ισοτροπικούς/γυροηλεκτρικούς/γυρομαγνητικούς κυλίνδρους. Για την περίπτωση πιο πολύπλοκων δομών, διστρωματικό και τριστρωματικό γυροηλεκτρικό/γυρομαγνητικό κύλινδρο, επιστρατεύτηκε το λογισμικό πακέτο HFSS. Επιπλέον, έγινε σύγκριση με την προσφάτως αναπτυγμένη μέθοδο υβριδικής προβολής (Hybrid Projection Method, HPM) για ηλεκτρικά μεγάλους κυλίνδρους.

Η ηλεκτρομαγνητική σκέδαση από διάφορα αντικείμενα αποτελεί τομέα μεγάλου επιστημονικού ενδιαφέροντος, όσον αφορά τον εφαρμοσμένο ηλεκτρομαγνητισμό, εδώ και δεκαετίες. Ο λόγος πίσω από το ενδιαφέρον αυτό είναι η συνεχής ανάπτυξη

νέων καινοτόμων εφαρμογών σε τομείς όπως η νανο-φυσική, η φωτονική αλλά και η σπουδαιότητα άλλων εφαρμογών, όπως για παράδειγμα ο υπολογισμός του ρυθμού απορρόφησης ακτινοβολίας, ο οποίος είναι υψίστης σημασίας για εφαρμογές όπου συμμετέχει ο ανθρώπινος παράγοντας και πρέπει να διαφυλαχθεί η υγεία του. Ως παράδειγμα μπορούμε να αναφέρουμε ότι μια κυλινδρική γεωμετρία μπορεί να χρησιμοποιηθεί για την προσομοίωση νανο-δομών, όπως για παράδειγμα κεραίες ή για την προσομοίωση ενός ανθρώπινου χεριού ή του ανθρώπινου κορμού.

Οι κυλινδρικές διατάξεις αποτελούν τα τελευταία χρόνια το μέσο, μέσω του οποίου έχουν έρθει στο προσκήνιο πληθώρα ενδιαφερόντων φαινομένων, κυρίως στον τομέα της φωτονικής. Κάποιες από αυτές τις εφαρμογές είναι τα μαγνητο-οπτικά υλικά, τα οποία στοχεύουν σε εφαρμογές ενεργού ρύθμισης της διεύθυνσης του σκεδαζόμενου κύματος από κυλίνδρους, cloaking-to-superscattering λειτουργία με την χρήση υλικών αλλαγής φάσης, ανισοτροπικά νανο-καλώδια για λειτουργία υπερ-σκέδασης, κυλινδρικά ραδιοκύματα για πλάσμα tokamak, ρύθμιση πλασμονικού μανδύα μέσω εξωτερικού μαγνητικού πεδίου, διερεύνηση ρυθμών κοιλότητας σε δαχτυλίδια μετα-υλικών, δημιουργία ηλεκτρομαγνητικών μαύρων τρυπών κ.α.

Όπως αναφέρθηκε και ανωτέρω η μελέτη της σκέδασης ηλεκτρομαγνητικών κυμάτων από κυλινδρικές διατάξεις κυκλικής διατομής έχει αποτελέσει αντικείμενο μελέτης για αρκετές δεκαετίες. Ως εκ τούτου υπάρχει μια ευρεία γκάμα προσεγγίσεων για την λύση του προβλήματος αυτού τόσο σε ισοτροπικά, όσο και σε ανισοτροπικά ομογενή ή όχι υλικά. Ενδεικτικά αναφέρουμε τις ακόλουθες: Η ακριβής λύση για την σκέδαση από ομογενή κύλινδρο κατά την κάθετη πρόσπτωση ηλεκτρομαγνητικού κύματος έχει υλοποιηθεί, καθώς και η ακριβής λύση για την σκέδαση από ομογενείς γυροηλεκτρικούς κυλίνδρους. Επιπλέον, έχει μελετηθεί η σκέδαση ύστερα από την πρόσπτωση ηλεκτρομαγνητικού κύματος υπό γωνία, χρησιμοποιώντας χωρικές ολοκληρωτικές εξισώσεις. Επίσης, έχει αναπτυχθεί μια μέθοδος πεπερασμένων στοιχείων για την περίπτωση της πρόσπτωσης κύματος, υπό γωνία, σε κύλινδρο.

Η μέθοδος η οποία αναπτύσσεται στο κεφάλαιο αυτό, βασίζεται στις CFVIEs και επιλύει το πρόβλημα της σκέδασης από κύλινδρο όταν πάνω του προσπίπτει κάθετα ένα ηλεκτρομαγνητικό κύμα. Ο κύλινδρος θεωρείται ότι αποτελείται από γυροηλεκτρικό/γυρομαγνητικό υλικό συνεχούς μεταβολής και υψηλής ανομοιογένειας, έχει άπειρη διάσταση στον άξονα z και είναι ηλεκτρικά μεγάλος. Η ανισοτροπία περιγράφεται μέσω των τανυστών που εκφράζουν την διαπερατότητα και την επιδεκτικότητα του υλικού. Μια καινοτομία που προσφέρει η παρούσα μέθοδος είναι ότι παρέχει μια λύση πλήρους κύματος, βασισμένη σε ορθογώνιες κυλινδρικές συναρτήσεις βάσης. Πιο συγκεκριμένα, οι CFVIEs λύνονται με την χρήση της μεθόδου CDSE, όπου τα άγνωστα πεδία αναπτύσσονται σε τύπου Dini CVWFs $\mathbf{M}$, $\mathbf{N}$ διανύσματα με μηδενική απόκλιση και σε αστρόβιλα $\mathbf{L}$ διανύσματα. Επίσης, εγκαθιδρύονται πλήρως ορθογώνιες ιδιότητες για τις τύπου Dini CVWFs εντός του κυλίνδρου, μέσω της ικανοποίησης κατάλληλων ιδιο-εξισώσεων από τα ορίσματα των διανυσμάτων $\mathbf{M}$, $\mathbf{N}$ και $\mathbf{L}$. Ένα σημείο κλειδί, το οποίο αξίζει να τονιστεί, είναι η υποβάθμιση των αρχικών CFVIEs σε ένα σύνολο από αλγεβρικές εξισώσεις. Αυτό αποτελεί το βασικότερο όλων των πλεονεκτημάτων της μεθόδου που αναπτύχθηκε.

Αξίζει να σημειωθεί ότι η μέθοδος που αναπτύχθηκε μπορεί να χειριστεί διατάξεις που περιλαμβάνουν υλικά με μεγάλη ανομοιογένεια, συνεχούς μεταβολής, όσον αφορά την διαπερατότητα και την επιδεκτικότητα, συμπεριλαμβανομένων και των ανισοτροπικών υλικών. Ένας εξαντλητικός αριθμός ελέγχων των αποτελεσμάτων πραγματοποιείται προκειμένου να επιβεβαιωθεί η ορθότητα της μεθόδου, πράγμα το οποίο επιβεβαιώνεται.

Στο τρίτο κεφάλαιο αναπτύσσεται μια μέθοδος για τον υπολογισμό των κανονικοποιημένων κυματαριθμών αποκοπής για την περίπτωση κυκλικών κυματοδηγών, οι

οποίοι έχουν υλικά μεγάλης ανομοιογένειας στο εσωτερικό τους, τα οποία έχουν γυρο-
τροπικά χαρακτηριστικά. Η μέθοδος αυτή βασίστηκε στην CFVIE, όπως και η αντίσ-
τοιχη που χρησιμοποιήθηκε στο δεύτερο κεφάλαιο. Οι κανονικοποιημένοι κυματαρι-
θμοί προκύπτουν ως ρίζες μιας determinantal εξίσωσης η οποία προκύπτει από την
λύση των CFVIEs με την χρήση των CDSE αναπτυγμάτων, όπου τα άγνωστα πεδία
στο εσωτερικό του κυλίνδρου αναπτύσσονται σε ορθογώνιες συναρτήσεις τύπου Dini.
Προκειμένου να λάβουμε υπόψη μας την οριακή συνθήκη στο σύνορο του μεταλ-
λικού τοιχώματος του κυλίνδρου, κατασκευάστηκαν δύο τροποποιημένες συναρτήσεις
Green, οι οποίες αναπτύχθηκαν σε διανυσματικές κυλινδρικές κυματικές συναρτή-
σεις και οι οποίες εισάγονται στον πυρήνα των CFVIEs. Αυτές οι τροποποιημένες
συναρτήσεις Green κατασκευάζονται μέσω της επιβολής, στην δυαδική μορφή, της
ικανοποίησης των ηλεκτρικών συνοριακών συνθηκών στο σύνορο του μεταλλικού
κυματοδηγού. Οι CDSE σε συνδυασμό με τις τροποποιημένες συναρτήσεις Green
επιτρέπουν τον αναλυτικό υπολογισμό των ολοκληρωμάτων και την υποβάθμιση των
CFVIEs σε ένα σύνολο από αλγεβρικές εξισώσεις. Εν συνεχεία πραγματοποιείται
εξαντλητικός έλεγχος των αποτελεσμάτων, με σκοπό την εξακρίβωση της ορθότη-
τας της μεθόδου που αναπτύχθηκε. Για τον λόγο αυτό, αρχικά, κατασκευάστηκαν οι
λύσεις για την εξαγωγή των κανονικοποιημένων κυματαριθμών στην περίπτωση του
ομογενούς γυροτροπικού κυματοδηγού, μέσω της μεθόδου του χωρισμού των μεταβλ-
ητών. Ύστερα, χρησιμοποιήθηκε το λογισμικό πακέτο HFSS για την περίπτωση του
διστρωματικού ισοτροπικού και του τριστρωματικού γυροηλεκτρικού κυματοδηγού.

Η εξαγωγή των κυματαριθμών αποκοπής ή των συχνοτήτων αποκοπής, έχει
πολύ μεγάλη πρακτική σημασία για τη σχεδίαση πληθώρας μικροκυματικών στοιχείων.
Ενδεικτικά, κάποιες από τις πρακτικές εφαρμογές όπου είναι απαραίτητη η γνώση
τους είναι οι πολύ-συχνοτικοί μορφοτροπείς (mulifrequency transducers), τα φίλτρα
δύο ρυθμών (dual-mode filters), οι πολυπλέκτες που στηρίζονται σε κυκλικούς κυ-
ματοδηγούς, οι διαιρέτες κ.α. Επίσης μπορούν να χρησιμοποιηθούν για την ανάπ-
τυξη στοιχείων οδήγησης από μετα-υλικά, τα οποία έχουν οδηγήσει στην μείωση των
συχνοτήτων αποκοπής και στην διάδοση κυμάτων κάτω από την συχνότητα αποκοπής
(below cutoff), σε κυκλικούς κυματοδηγούς που αποτελούνται από μετα-υλικά.

Αυτή η τεράστια ποικιλία εφαρμογών, που απαιτούν την γνώση των κυματαρ-
ιθμών αποκοπής, έχει ως αποτέλεσμα την ύπαρξη μιας εκτενούς βιβλιογραφίας, η
οποία μελετάει το αντικείμενο αυτό και επομένως την ύπαρξη πληθώρας μεθόδων
που αντιμετωπίζουν αυτό το πρόβλημα. Οι μέθοδοι αυτές αφορούν ισοτροπικά και
ανισοτροπικά, ομογενή και ανομοιογενή υλικά.

Όπως αναφέρθηκε και ανωτέρω, στο κεφάλαιο αυτό αναπτύσσεται μια μέθοδος
για τον υπολογισμό των κανονικοποιημένων κυματαριθμών αποκοπής, η οποία στηρίζε-
ται στις CFVIEs. Πέραν της κατασκευής των τροποποιημένων συναρτήσεων Green,
για την ικανοποίηση των οριακών συνθηκών που επιβάλλει ο μεταλλικός κυματοδηγός,
αξίζει να σημειωθεί ότι επιτυγχάνεται υποβάθμιση των CFVIEs σε σύνολα από αλγε-
βρικές εξισώσεις, τα οποία διαφέρουν από αυτά που προέκυψαν στο δεύτερο κεφάλαιο,
λόγω της ύπαρξης των τροποποιημένων συναρτήσεων Green. Επίσης, η μέθοδος
που αναπτύχθηκε επιτρέπει τον υπολογισμό των κανονικοποιημένων κυματαριθμών
αποκοπής, τόσο για γυρομαγνητικά/γυροηλεκτρικά υλικά με υψηλή ανομοιογένεια,
όσο και για υλικά που περιέχουν διασπορά.

Στο τέταρτο κεφάλαιο της παρούσας διδακτορικής διατριβής αναπτύσσονται
ασυμπτωτικές εκφράσεις κλειστής μορφής για τον υπολογισμό των μιγαδικών συντον-
ισμών των whispering gallery ρυθμών (WGM), για την περίπτωση του ομογενούς
γυροηλεκτρικού κυκλικού συντονιστή απείρου μήκους. Επιπλέον, γίνεται επέκταση
της μεθόδου VIE-CDSE, που περιγράφηκε στα προηγούμενα κεφάλαια, ούτως ώστε
να υποστηρίζει την πρόβλεψη των μιγαδικών WGMs για συντονιστές που αποτελούν-

ται από γυροηλεκτρικά υλικά υψηλής ανομοιογένειας και συνεχούς μεταβολής. Επιπλέον, οι διανυσματικές ορθογώνιες κυματοσυναρτήσεις της VIE επεκτείνονται, μέσω ασυμπτωτικών εκφράσεων κλειστής μορφής, ώστε να υποστηρίζουν τους μεγάλους δείκτες των εμπλεκόμενων CVWFs. Με αυτό τον τρόπο οι ιδιο-βάσεις που χρειάζονται για την επίλυση της VIE δεν έχουν αριθμητικές αστάθειες όταν εμπλέκονται πολύ μεγάλοι δείκτες στις συναρτήσεις Bessel. Οι μιγαδικοί συντονισμοί που προκύπτουν από τις ασυμπτωτικές εκφράσεις κλειστής μορφής, για την περίπτωση του ομογενούς γυροηλεκτρικού συντονιστή, καθώς και αυτές που προκύπτουν από τις VIE για ένα στρώμα υλικού, συγκρίνονται με τις μιγαδικές ρίζες που εξάγονται από την αριθμητική επίλυση των χαρακτηριστικών εξισώσεων των TE/TM ρυθμών, που προκύπτουν από την μέθοδο χωρισμού των μεταβλητών, χρησιμοποιώντας τεχνικές εύρεσης μιγαδικών ριζών. Εν συνεχεία παρατίθενται οι υπολογισμοί για την περίπτωση πολύ μεγάλης τάξεως συντονισμών WGM ,για κυλινδρικούς συντονιστές που συντίθενται από ομογενή και ανομοιογενή υλικά.

Ευχαριστίες

Η περάτωση αυτής της διδακτορικής διατριβής σηματοδοτεί το τέλος της μακράς περιόδου μου ως υποψήφιο διδάκτορα. Η διαδρομή αυτή δεν ήταν στρωμένη με ροδοπέταλα και σε καμία περίπτωση δεν θα μπορούσα να έχω φανταστεί, ούτε στο ελάχιστο, τι θα μου επιφύλασσε το ταξίδι αυτό. Κοιτώντας πίσω, θα το χαρακτήριζα ως ένα τρενάκι το οποίο σε περνάει από διάφορα μέρη, όμορφα και μη, με διάφορες ταχύτητες, από του φωτός έως του σαλιγκαριού, με διάφορες θερμοκρασίες, από του ήλιου έως του αχανούς διαστήματος. Τώρα που το ταξίδι έφτασε στο τέλος του, μπορώ να πω μετά βεβαιότητας, ενώνοντας τις κουκκίδες προς τα πίσω, ότι όλες αυτές οι δοκιμασίες είχαν ως απώτερο σκοπό κάτι πολύ μεγαλύτερο από την απόκτηση ενός ακόμα πτυχίου. Το διακύβευμα δεν ήταν άλλο από το να γνωρίσω καλύτερα τον εαυτό μου! Όλες αυτές οι δοκιμασίες με ανάγκασαν να σκάψω βαθύτερα μέσα μου και να ανακαλύψω κρυφές πτυχές μου, των οποίων αγνοούσα πλήρως ακόμα και την ύπαρξη. Παρότι πολλές από αυτές τις δοκιμασίες θα ήθελα να τις έχω αποφύγει, πλέον γνωρίζω το θετικό αντίκτυπο που άφησαν επάνω μου 'χαράζοντας' με ανεξίτηλα. Πέρα όμως από τις πρακτικές ικανότητες, τις θεωρητικές γνώσεις και τα πνευματικά δώρα που μου δόθηκαν, το ταξίδι αυτό μου επιφύλασσε την γνωριμία με ανθρώπους οι οποίοι επέδρασαν πάνω μου με τρόπο καθοριστικό και μοναδικό. Σε αυτούς, καθώς και σε όλους τους άλλους που με στήριξαν σε αυτό το ταξίδι, και στην ζωή μου, θα ήθελα να αφιερώσω την παρούσα διατριβή.

Αδιαπραγμάτευτα την πρώτη θέση, όσον αφορά τους ανθρώπους που θέλω να ευχαριστήσω από τα βάθη της καρδιάς μου, κατέχει ο επιβλέποντας καθηγητής μου κ. Ιωάννης Ρουμελιώτης, ο οποίος με πίστεψε δίχως να έχει κάποιο συγκεκριμένο λόγο να το κάνει. Εμφανίστηκε ως 'μάννα εξ ουρανού' και με έβγαλε από μια πάρα πολύ δύσκολη θέση στην οποία βρισκόμουν εκείνη την δεδομένη χρονική στιγμή. Χωρίς περίσσεια υπερβολή, μπορώ να πω ότι, η παρούσα διδακτορική διατριβή αποτελεί ένα απόσταγμα της καλοσύνης του, της καλοσύνης που αποπνέει ένας ΔΑΣΚΑΛΟΣ, με όλη την σημασία της λέξης αυτής. Η πράξη του αυτή αναπτέρωσε την πίστη στον εαυτό μου αλλά και στο ανθρώπινο είδος γενικότερα. Ελπίζω η πορεία μου να σας κάνει να νιώθετε, έστω και ελάχιστα, δικαιωμένος. Σας είμαι αιώνια υπόχρεος!

Στην συνέχεια θα ήθελα να αναφερθώ στον στενότατο συνεργάτη μου, και κατ' εμέ φίλο, Δρ. Γρηγόριο Ζούρο, ο οποίος αποτέλεσε μέντορα μου καθόλη τη διάρκεια της εκπόνησης της διδακτορικής μου διατριβής. Ο τρόπος που με πίεσε να δουλεύω όλο και περισσότερο, η αμετακίνητη επιθυμία του για το τέλειο, η συνεχόμενη στήριξη σε όλα τα προβλήματα που προέκυπταν, οι λύσεις του σε προβλήματα που μου φαινόντουσαν απροσπέλαστα, καθώς και πολλά άλλα, με καθόρισαν τόσο ως προς την προσέγγιση μου στον επαγγελματικό τομέα αλλά και γενικότερα σαν άνθρωπο. Σου είμαι για πάντα ευγνώμων!

Στο σημείο αυτό θα ήθελα να ευχαριστήσω ιδιατέρως τους φίλους μου Νίκο Αναγνώστου, Δημήτριο Κούσουλα και Γεώργιο Σαμαρέντζη, διότι διαδραμάτισαν καθοριστικό ρόλο στην αποφόρτιση και την υποστήριξη μου στις στιγμές που τα πράγματα φαινόντουσαν 'σκοτεινά'. Ήσασταν εκεί σε όλες τις στιγμές και ποτέ δεν αλλάξατε την συμπεριφορά σας απέναντι μου. Για πάντα δίπλα σας!

Επιπλέον θα ήθελα να εκφράσω ένα τεράστιο ΕΥΧΑΡΙΣΤΩ στους φίλους μου Χρήστο Παπασωτηρίου, Μάριο Λουκά, Άννα Ρούμκου, Γιάννη Αλεξόπουλο και Ελένη Γεωργιοπούλου για τις ευχάριστες και ενδιαφέρουσες συζητήσεις μας, μα πάνω απ'όλα για την άνευ όρων κατανόηση και την στήριξη που μου προσφέρατε. Ελπίζω να είμαστε φίλοι έως τα βαθιά γεράματα. Πάντα στην διάθεση σας!

Δεν θα μπορούσα να μην αναφέρω τις απέραντες ευχαριστίες μου στον καθηγητή

των μαθηματικών μου κ. Ανδρέα Καψάλη, τον οποίο θεωρώ μέλος της οικογένειας μου. Με τον τρόπο σου καθοδήγησες, εμένα και τον αδερφό μου, σε μονοπάτια που δεν ήταν, φαινομενικά, πλασμένα για εμάς. Δάσκαλε, σου είμαι απόλυτα ευγνώμων για την γενναιοδωρία σου απέναντι μας, καθώς και για τον τρόπο που μας έκανες να βλέπουμε τον κόσμο και τους εαυτούς μας. Επίσης θα ήθελα να ευχαριστήσω την καθηγήτρια των μαθηματικών μου, στο Δημοκρίτειο Πανεπιστήμιο Θράκης, κα. Αμαλία Μεϊμαρίδου διότι ο τρόπος που με έμαθε να αντιμετωπίζω την επιστήμη, τους ανθρώπους και τον εαυτό μου με συντροφεύει έως σήμερα και έπαιξε καθοριστικό ρόλο στην εξέλιξη μου. Σας ευχαριστώ αμφότερους για όλα!

Εν συνεχεία, θα ήθελα να εκφράσω την απεριόριστη ευγνωμοσύνη μου στον π. Γερβάσιο τον Σιμωνοπετρίτη και τον π. Τιμόθεο Αγγελή. Τις σχέσεις αυτές δεν μπορώ να τις χαρακτηρίσω ΄τυχαίες΄ αλλά, στον αντίποδα, θα τις χαρακτήριζα Θεόσταλτες. Ο Θεός σας φανέρωσε στο διάβα μου την κατάλληλη στιγμή και βοηθήσατε τα μέγιστα προκειμένου να συνεχίσω ως το τέλος της διαδρομής, με πίστη και υπομονή. Εύχομαι ο Θεός να σας σκεπάζει και ελπίζω η σχέση αυτή να διατηρηθεί αναλλοίωτη στον χρόνο. Αιώνια ευγνώμων!

Για το τέλος άφησα τους τρείς πυλώνες της ζωής μου, γύρω από τους οποίους έχω χτίσει, και θα συνεχίσω να χτίζω, ανεξαρτήτως των περιστάσεων. Τον πρώτο πυλώνα αποτελεί η μητέρα μου, Μαρία Φλώρου, η οποία κυριολεκτικά αφιέρωσε όλη της την ζωή στην ανατροφή και την στήριξη των παιδιών της. Μαμά, η αγάπη σου και ο άνευ ορίων μόχθος που κατέβαλλες καθημερινά για να μην μας λείψει τίποτα μας έχει καθορίσει ολοκληρωτικά. Επειδή δεν υπάρχει τρόπος να στο ανταποδώσουμε, πασχίζουμε απλώς να σου δείξουμε ότι το καταλάβαμε. Ο δεύτερος πυλώνας αφορά τον αδερφό μου, Αλέξανδρο Κάτσινο, ο οποίος αποτελεί τον καλύτερο μου φίλο, το ίνδαλμα και τον προστάτη μου, από τα παιδικά μου χρόνια! Αλέξανδρε, όπως έχω ξαναπεί, αποτέλεσες το παγοθραυστικό για τον δρόμο αυτό που έχουμε χαράξει και είσαι αυτός που με παρέσυρε σε αυτή την ΄τρελή΄ διαδρομή. Τον τρίτο πυλώνα της ζωής μου αποτελεί η σύντροφος μου Μαρία Ραμαντάνη. Μαράκι μου, η υπομονή σου, ο χαρακτήρας σου, η σιωπηλή υποστήριξη σου και η επιμονή σου στο βάθος του χρόνου δεν μπορούν να περιγραφούν από λόγια. Η οποιαδήποτε προσπάθεια να τα εκφράσω απλώς θα τα έκανε να χάσουν κάτι από την αξία τους. Αιώνια δικός σας!

*The basic difference between an ordinary man and
a warrior is that a warrior takes everything as
a challenge while an ordinary man takes
everything as a blessing or a curse.*
– Carlos Castaneda

Contents

Implantable Antenna for Biomedical Telemetry Applications

The rapid evolution in the field of electronics enables the development of small electronic medical devices, suitable for implantation inside the human body. The size of Implantable Medical Devices (IMDs) is critically dependent on the size of the antennas integrated into the device and enables wireless communication with external monitoring/control equipment [1]. Moreover, the design and fabrication of miniature implantable antennas is a challenging task due to the rather low-frequency range that has been dedicated worldwide for this kind of application (MedRadio, $401 - 406$ MHz). Nevertheless, MedRadio provides several advantages, including: (i) low noise, (ii) low attenuation, (iii) sufficient penetration inside human tissue, (iv) low power electronics, (v) cheap electronics and (vi) worldwide availability. Apart from MedRadio, the ISM band $(2.4 - 2.5$ GHz) can be used for biotelemetry purposes providing higher data transmission rates with shorter distance range than MedRadio by virtue of higher attenuation [2]. In most cases, IMD devices are powered by an integrated battery, which presents several disadvantages, such as limited lifetime and the need for replacement usually through a new surgical procedure. In order to extend battery's lifetime, several approaches have been proposed, including energy harvesting from air flow, glucose oxidation, muscle movement, etc. [1]. An alternative way to reduce energy consumption and prolong battery life is the use of wake up/sleep signals every time data transmission is necessary. A signal in the ISM band is sent to the device as a wake-up signal and the data is transferred using the MedRadio band. Moreover, great attention must be taken to the design procedure in order to satisfy the SAR limits and preserve patient's safety.

1.1   Introduction

In body medical devices have been attracting high scientific interest for the last 20 years in a variety of medical applications for prevention, diagnosis and treatment as they are superior to wearable medical devices. The reason behind this fact is that the wearable medical devices receive signals that come from outside the body while the implanted ones can be placed inside the human body and by that broaden the number of the existent applications and moreover the development of novel ones. In body medical devices have two main uses [3]: (1)As sensors to monitor the function of organs or parameters of the body. (2)As stimuli or, equivalently, Functional Electrical Stimulation (FES) systems.

We can divide the in body medical devices into three major subcategories based on how they are introduced into the human body, those categories are:

(1) Implantable devices, which are inserted into the body by performing surgery [4]. Typical examples of implantable devices are the sensors that are monitoring physiological signals such as intracranial pressure [5], body temperature [5], blood pressure [5], blood glucose levels [6], etc. Also, implantable devices can be used as stimuli and typical examples of this category are the pacemakers [7], the restoration of limb movement [8], the control of bladder function [9], the restoration of vision [10], etc.

(2) Swallowable medical devices, which are in the form of a capsule and can be easily consumed by the patient as a pill [11]. One of the most common ingestible device is that of wireless endoscopy that is used by doctors when is needed to examine the human intestines. Nowadays wireless ingestible devices can perform more complicated functions leading to new applications such as the monitoring of the body's response to drug therapies and at the same time may inject drugs targeted along the gastroesophageal tract.

(3) Injectable devices, which are inserted into the human body through needles by a minimally invasive procedure and perform sensory and neurostimulatory functions. A wide variety of applications will use injectable medical devices and many inventions will come in the future because those devices are very recent [12].
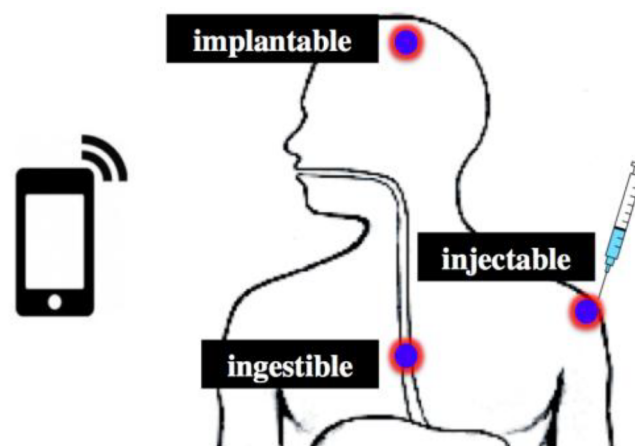

Figure 1.1   Implantable, injectable and ingestible medical devices for wireless biotelemetry purposes [3].

When we use the term telemetry we mean the remote measurement and reception of data of any kind. The data is measured at the point of interest and are transmitted through the telemetry system, in most cases an antenna, to a remote receiving station consisting of an external monitoring and control device. That kind of systems are used in a wide variety of applications starting from tracking a car to tracking rockets and aircrafts. But, in the case of medical telemetry we refer to the remote transmission of signals/data that are extracted for medical purposes. So, a key element of the operation of in body medical devices, that makes them very helpful, is their ability to communicate with external base stations. These base stations may be external monitoring or control devices and the extracted data can be used by the doctor for diagnosis and treatment. In the case of in body devices, the base station may be located on or within walking distance of the patient.

Medical telemetry can be a two-way system, i.e. the device in the body can send data to the external base station but also receive data from it. So, the communication between the external base station and the in body device can be categorized as:

(1) Upper link, the transmission of data (measured physiological signals) from the body to the external device.

(2) Down link, the transmission of data from the external to the internal device in order to modify some of the parameters of the implantable device. Such actions are very useful because can help the medical device to have the best possible effect in the case of stimuli use.

Before the arrival of the miniaturized antennas, inductive couplings were the most common way of achieving medical telemetry for in body medical devices. These are wireless connections formed between two mutually coupled coils, one inside the body and one outside the body [13]. Nevertheless, inductive couplings have significant weaknesses, as listed below:

(1) Low data rate ($1 - 30$ kbps).

(2) Very limited communication range between in-body and external devices (less than 10 cm).

(3) Low tolerance to relative position and alignment of coils (high sensitivity).

Because of these significant drawbacks, research interest today is focused on wireless body telemetry of medical devices through antennas. The patient's in-body devices communicate bi-directionally with an external base station. Some of the functions that the base station can perform are:

(1) Post-processing of received data and decision making.

(2) Warning the patient of a significant medical event.

(3) Notification of other implantable devices for injecting a drug.

(4) Save locally received data for future post-processing.

In body devices are a very important innovation in the field of medicine capable of improving the quality of patients life, as it allows the immediate and continuous reception of data through sensors and therefore the immediate recognition of deviations of this data from normal values, or introduction of innovative therapies through targeted, intrinsic stimulation or infusion of drugs.

A wide variety of frequency bands for in-body medical devices have been used from time to time, with the most common being the Medical Device Radio Communication Service (MedRadio) at 403.5 MHz ($401 - 406$ MHz) and the Industrial, Scientific and Medical (ISM) band at 2.4 GHz. Choosing the right operating frequency band is not an easy task because it involves many restrictions in the design process of the antenna and also to the data rate of the communication. A key advantage of the low frequency bands that makes them more suitable for these ap-

plications is the lower losses in biological tissues. For example, frequencies in the order of $3-5$ GHz impose an attenuation of $20-30$ dB for every 2 cm of biological tissue. In practice, swallowing antennas mainly use high frequencies to achieve better transmission, better image resolution and smaller layout.

Wireless data transmissions, including wireless telemetry for in-body medical devices, can also be performed in unlicensed bands of the electromagnetic (EM) frequency spectrum. However, unlicensed frequency bands are not common in all countries.

1.1.1　Medical Device Radio Communication Service (MEDRADIO)

A huge problem that biomedical telemetry applications were facing until the beginning of the century was that no frequency band was exclusively dedicated worldwide for wireless biotelemetry. This problem solved in 1997 with the recommendation SA.1346 of the International Telecommunications Union-Radiocommunications (ITU-R), which defined the frequency band $402.0-405.0$ MHz exclusively for Medical Implant Communications Services (MICS) [14], [15]. The MICS zone was defined for two types of applications:
(a) Communication between an implantable medical device and an external base station.
(b) Communication between medical devices implanted within the same human subject.

The MICS band supported simultaneous transmission of ten (10) channels with a maximum bandwidth of 300 kHz per channel. In case the wireless medical telemetry system uses different operating frequencies for the upper and lower coupling, then the cumulative bandwidth of the two transmissions should not exceed the value of 300 kHz. This means that in order to achieve high transmission rates only one device transmits at a time. Due to the growing needs of new applications in biomedical technology ETSI (European Telecommunications Standards Institute) increased the MICS band by one MHz on each side and designated the MICS/MEDS band, where MICS maintained the central frequencies $402-405$ MHz and the regional extensions of the zone are referred to as MEDS. Also, in May 2009, the FCC (Federal Communications Commission) similarly increased the MICS bandwidth and renamed it the Medical Device Radio Communication Service (MedRadio).

Another key parameter that we have to keep in mind all the time is electromagnetic interference. In order to avoid that problem a maximum permissible equivalent radiated power (ERP) was set. More specifically ERP should not exceed $25\mu W$. Equivalently, the maximum field strength in any direction shall be equal to, or less than, the maximum intensity, in the same direction, of a tuned dipole supplied with a power of $25\mu W$. The ultimate goal is the simultaneous telemetry of multiple implantable medical devices in the same space avoiding any effect of electromagnetic interference in the transmissions of the Meteorological Service Aids (MetAids) zone that takes place in the same frequency band. The standard coverage radius of MedRadio-MICS/MEDS band medical telemetry systems is 2 m.

1.1.2　Industrial Scientific and Medical (ISM)

ISM bands were originally reserved internationally for non-commercial uses of the EM spectrum related to Industrial Scientific and Medical (ISM) applications. However, several of the ISM bands are currently used for commercial applications, as no government approval is required. The most commonly used ISM band for wireless telemetry of implantable medical devices is the $2400.0-2483.5$ MHz band. According to ETSI EN 300 328, the maximum active radiated power in this zone should

not exceed -10 dBW (100 mW). At least fifteen different, non-overlapping channels may be used in the available frequency range.

The fact that ISM bands concentrate a large amount of interest is because of a key advantage that are providing. That key advantage of ISM bands is the increased bandwidth, which allows high-speed data transmission, so video transmission can be supported in this band. The cause behind this fact is the high frequency that the communication takes place. In addition, the penetration of EM radiation into the human body in the ISM bands is much lower than that in the MICS band, due to a higher operating frequency and therefore higher attenuation that leads to much lower penetration depth. For example, at a frequency of 2450.0 MHz it is stated that the depth of skin within muscle tissue is equal to 22 mm. On the contrary, at a frequency of 403.5 MHz the penetration depth is equal to 52 mm. Those benefits does not come without a cost. The most important disadvantage of ISM bands is the realization of various simultaneous transmissions in these bands leading to serious issues of EM interference.

1.1.3 Wireless Medical Telemetry Services (WMTS)

In the USA Wireless Medical Telemetry Services (WMTS) zones have been assigned for remote patient monitoring. The main advantage of the WMTS frequency band is the large bandwidth that offers for wireless telemetry applications of implantable medical devices. Indicatively, it is stated that in the WMTS $608.0 - 614.0$MHz band, four channels with a bandwidth of 1.5 MHz each are allowed. Another key advantage of the WMTS bands is the lack of interference due to the fact that this band is completely dedicated to medical telemetry applications, so these devices are protected from other sources of EM radiation. On the other hand, the main disadvantage of these bands is that there are not available in countries outside the US, so any device that is designed to operate in this band cannot operate outside of the USA.

1.2 Challenges of Implantable Antennas and Miniaturization Techniques

The design of an antenna that is meant to be implanted inside the human body has a plethora of challenges. The most important challenges associated with in body medical devices arise from the fact that they must be small in size and do not occupy a large volume in the body as well as that they are in contact with the human tissue, so they must be strictly biocompatible in order to prevent rejection of the implant and short circuit of the device. Some of the most important challenges that we have to overcome in order to successfully design an antenna are listed below:

(1) Biocompatibility in order to preserve patient safety from rejection of the implant.

(2) Miniaturization of the implantable antenna in order to be feasible to be implanted inside the human body.

(3) Low power consumption in order to extend the battery's lifetime and prevent any unnecessary surgical operation for the replacement of the battery.

(4) Far-field gain which indicates the radiation characteristics that the receiver should have in order to achieve a reliable biotelemetry communication.

(5) Specific absorption rate (SAR) values that comply with the IEEE standards in order to ensure patients safety.

(6) Adequate bandwidth in order to ensure the stability of the performance of the

implantable antenna.

On this, it is noted that the most widely used antennas in the body are microstrip antennas due to their high flexibility in format, their design and the results achieved.

1.2.1   Challenges and Solutions

Implantable antennas must be biocompatible in order to ensure patient safety and prevent possible rejection of implantable medical devices from biological tissues. Another key problem that the antenna's biocompatibility solve is the avoidance of short-circuits. The implantable antenna includes metallic parts that are responsible for the radiation, so the designer has to ensure that those parts will not come in direct contact with the conduxtive biological tissue of the human body. Moreover, the biocompatibility and prevention of unwanted short circuits are particularly critical in the case of antennas intended for long-term implantation. There are two methods by which we can ensure the biocompatibility of the implantable antenna: (1) Use of biocompatible substrate-superstrate: The most common method of ensuring antenna's biocompatibility and avoid any short-circuit is the use of biocompatible materials as substrate and superstrate [16]. Common biocompatible materials are Teflon, the macor and ceramic alumina ($\epsilon_r = 9.4$, $tan\delta = 0.006$) which is used in the proposed antenna design [17]. It is important to emphasize that ceramic dielectric layers material is not easy to engrave and cut.
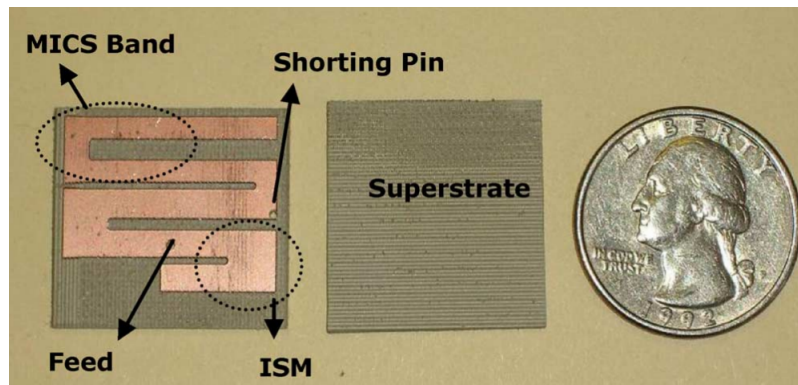
Figure 1.2   Dual band implanable antenna fabricated with biocompatible materials [16].

(2) Another possible way to achieve the desired biocompatibility of the antenna is encapsulation with biocompatible material. More specifically, we use a thin coating of low loss biocompatible material in order to physically separate the implantable antenna for the biological tissue [18]. The most used materials for the use as biocompatible coatings are zirconia, PEEK and elastometric Silastic MDX4-4210 [18],[19]. In the literature zirconia is considered as the most appropriate candidate due to its electrical properties. From an EM point of view zirconia is the optimal biocompatible coating material because of the high value of relative dielectric constant (ϵ_r) and the low value of tangent losses ($tan\delta$) limit the near field of the antenna within the biocompatible coating layer, and significantly reduce power losses. On the other hand, PEEK and Silastic MDX4-4210 elastomeric are significantly easier to prepare and handle but does not have great performance, from electromagnetic point of view. An important design factor of the antenna is the thickness of the biocompatible coating, because changes the environment that the antenna is operating

and of course its performance characteristics. The search for the optimal value of the thickness of the biocompatible coating is crucial in order to reduce power losses but we have to bear in mind that there should be no unnecessary increase in the antenna's dimensions.

Figure 1.3   Silicone and the antenna encased in the silicone [18].

1.2.2 Miniaturization Techniques

Another key challenge that we must overcome during the designing process of an implantable antenna is the large volume of the antenna. Recent developments in the field of electronics science have led to a significant reduction in the dimensions of implantable medical devices. A typical example that shows that need is an implantable artificial retina device. This device must be small enough to fit inside the human eyeball (12.5 mm radius). However, the dimensions of traditional half-wavelength ($\lambda/2$) or one-quarter wavelength ($\lambda/4$) antennas in the frequency bands designed for implantable medical device telemetry, and in particular in the low frequency MICS band, make it impossible to use for implant applications. Therefore, reducing the dimensions of implantable antennas is one of the most important design challenges.

The biological tissues in which the implantable antennas operate have a high value of relative dielectric constant (e.g., the relative dielectric constant, ϵ_r, of skin tissue at 402 MHz equals 46.7). As it is known, as much higher is the relative dielectric constant of the environment that the antenna operates, such smaller would be the physical dimensions of the implantable antenna. But, it should be highlighted that when the antenna is surrounded by a biocompatible coating, in order to ensure the biocompatibility, there is a degradation of the miniaturization that the environment offers. The reason behind this fact is the use of low relative dielectric constant materials as encapsulation layers. So, implantable antenna designers tend to use of microstrip patch antennas for medical applications because they allow for some additional miniaturization techniques. The ultimate goal is to reduce the size of the antenna at a given operating frequency, while maintaining the required EM performance in order to ensure a dignified communication with the external base station. The miniaturization techniques proposed in the literature for implantable microstrip antennas are as follows:

(1) Use of High Dielectric Constant Materials: The use of substrate and superstrate materials with a high relative dielectric constant (eg. ceramic alumina ($\epsilon_r = 9.4$)) reduces the active wavelength of the radiation, and leads at lower tuning frequen-

cies, contributing to the reduction of dimensions of the antenna. However, even if the dielectric material has high relative dielectric constant, the superstrate acts as an isolator between the antenna and the higher relative dielectric constant biological tissue. So, it is very important to take into account the thickness of the superstrate that we are going to use during the design process. The best solution, therefore, is the choice of biocompatible dielectric materials with the highest relative dielectric constant, and thin films.

(2) Elongation of the Current's Stream Flow Path to the Surface of the Microstrip:
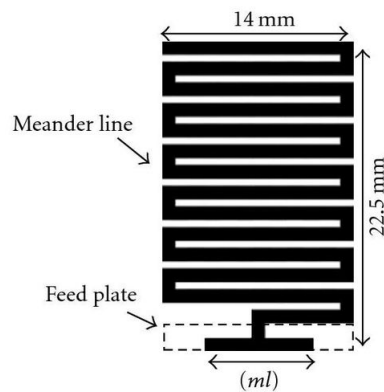
Figure 1.4   Meandered line antenna [20].

Similarly lower tuning frequency values and therefore reduction of the implantable antenna can be achieved with the designation of longer paths for the flow of current on the microstrip patch antenna. For that reason microstrip antennas in meander-like [16], spiral [21], waffle type [17], hook [22] shapes have been proposed.
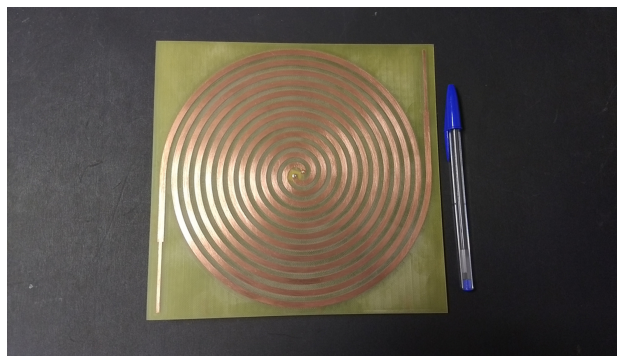
Figure 1.5   Spiral antenna [23].

(3) Use of shorting pins: The addition of a short-circuit conductor between the ground and the radiating patch of the microstrip antenna increases the effective size of the antenna and therefore it is possible to reduce its required physical dimensions, at a given operating frequency of the antenna. This technique works in much the same way that a grounding plate doubles the height of a monopolar antenna.

(4) Stucked patches: Vertical stacking of two or more strips is an alternative technique to increase the length of the current path on the strips, thereby reducing the
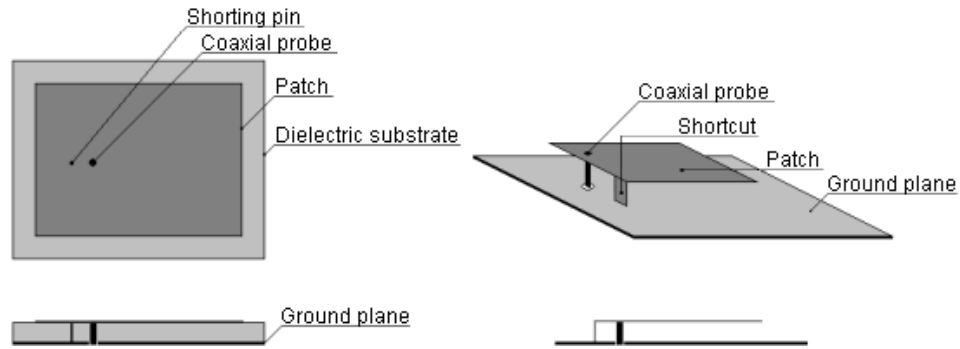
Figure 1.6   Shorting pin.

overall physical size of the antenna at a specific operation frequency.
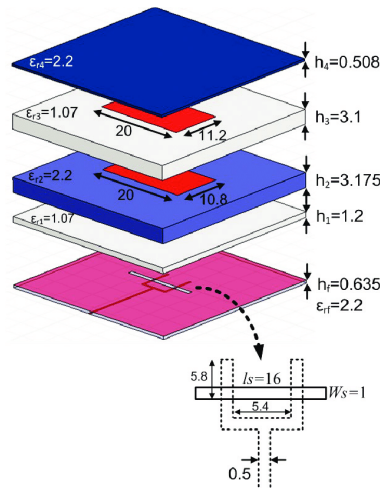
Figure 1.7   Patch stacking [24].

In general, circular antennas are preferred, with no sharp edges that could cause injury.

1.2.3   Bandwidth

As it is easily undestood, the environment that the implantable antenna operates affect its performance. So, biological tissues act as a dielectric load on the implantable antenna, and significantly affect its EM performance. Differences in the anatomical structure and electrical properties of biological tissues potentially alter the implantation antenna tuning performance. These changes must be taken into account when designing implantable antennas for realistic applications, in order to avoid any detuning effect. Therefore, increasing the antenna bandwidth becomes necessary in order to improve its tolerance to tuning effects.

1.2.4   Specific Absorption Rate (SAR)

As we mentioned earlier, because the implantable antennas operate inside the human body issues related to patient safety arise. In order to avoid those problems, we have to limit the maximum allowable power that can be applied to the implantable antenna and therefore the radiating power. Key quantities for the study of biological effects are the frequency of radiation, its power density (in mW/cm^2), and the rate of specific absorption of radiation (Special Absorption Rate-SAR). Frequency and power density are easily and accurately determined. On the contrary, the SAR index is more difficult to estimate, but is also considered the most appropriate for the evaluation of patient safety. The SAR (W/kg) expresses the amount of electromagnetic energy absorbed per unit mass of tissue per unit time and is determined by the ratio:

$$SAR = \frac{\sigma}{p}E^2 \qquad (1.1)$$

where σ is the special electric conductivity of the biological (S/m) at a given frequency, p is the density of biological tissue (kg/m^3) and E is the intensity of the electric field within the tissue (V/m). The value of SAR depends on:
(1) The characteristics of the radiation.
(2) The characteristics of the biological tissue.
(3) The distance of the emission source of the radiation.
(4) The biological tissue.
More specifically, the characteristics of radiation include the frequency, intensity, continuity or not of the wave propagation and the polarization of the radiation. In terms of frequency, as we mentioned earlier, high frequency waves are absorbed superficially, while radio waves penetrate deeper to the inside of the tissue due to the change of the electric properties of the human tissue with respect to frequency. More specifically, the human tissue exhibits higher losses when the frequency is higher. The radiation's polarization is defined as the different orientation of the body in relation to the wave's electric and magnetic field directions. Regarding the characteristics of biological tissue, its dimensions, curvature of the surface, density, specific conductivity and dielectric constant are examined. The dependence of the SAR value on such a large number of parameters implies the highly selective absorption of radiation by the human body.

As it is widely known, the biological tissues in their composition consist of about 70% water. Moreover, the water molecules are electric dipoles. That means that an electromagnetic wave can interact with those molecules by rotating elongation and oscillation. Moreover, the interaction of those molecules with an electromagnetic wave lead to an interaction of the electric currents of the organism with it. Taking all the above into account it is possible in the long term to cause complications that are classified as thermal and non-thermal [25].

When an increase in temperature of the body is more than $0.1°C$ he effect is characterized as thermal. A noticeable increase in temperature is caused by power densities above $1mW/cm^2$. When the human body is exposed to an electromagnetic field, the water dipoles and other charged particles of the organism are forced to orient in the direction of that field, and as a result, oscillate at a frequency similar to that of the field. The kinetic energy obtained by dipoles due to forced oscillations, frictions and collisions of charged particles with each other and with their neighbors, is translated into heat, which tends to increase body temperature. The body's homeostatic, thermoregulatory mechanisms can generally immediately return its temperature to normal levels for small changes in temperature. However, if the

amount of heat generated exceeds a maximum permissible value, these mechanisms may lose their ability to dissipate excess heat, resulting in an increase in temperature in the whole or in individual tissues and organs. An interesting fact is that if the increase in body temperature does not exceed one degree Celsius, then there is no risk to the body, even in long-term exposure. In these effects, however, the temperature of the tissue does not eventually rise, as the extra amount of heat is directly absorbed by local homeostatic mechanisms, making the tissue exposure to radiation of minor importance.
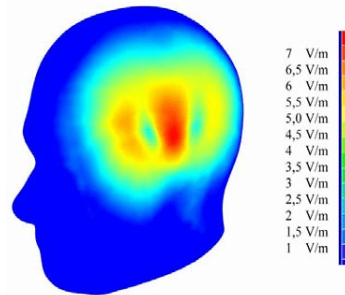
Figure 1.8   Specific absorption rate (SAR) of wearable device [26].

In contrast to thermal, non-thermal effects are those that cause some biological effect on the function of cell components, without a measurable increase in temperature (less than $0.1°C$). Such effects occur at very low power densities ($\mu W/cm^2$). Non-thermal effects are considered the most important, as they are not directly measurable with an instrument. But it is reasonable that any effects on the body depend on whether the radiation is strong or not, on the duration of exposure of the body to it, and on its distance from the source of radiation. The exact mechanisms of action in this case are not yet completely clear, and according to various studies, their etiology may lie in the relationship between the frequency of radiation and the frequency emitted by a biological tissue. The main non-thermal phenomena are considered to be the phenomenon of change in the flow of calcium in the brain cells and the microwave-acoustic phenomenon. More specifically, the outflow of calcium ions to brain cells increase when they are exposed to radio frequencies. This increased rate of outflow of calcium ions has been linked to the creation of resonance phenomena, where the frequency of radiation follows the natural frequencies of the brain, which could potentially facilitate the development of an existing cancer or suppress the body's ability to fight type of cancer cells.

Thus we understand that in terms of SAR it is important to comply with international regulations that aim to preserve patient's safety. For example, according to the IEEE in 1999 the average SAR was limited to one gram of cube-shaped tissue at less than 1.6W/kg, while the ICNIRP (International Commission on Non-Ionizing Radiation Protection) limits the average SAR to 10 grams DC power is 2 W/kg. In 2005 the IEEE then adopted the ICNIRP limits for the average SAR at 10 grams of continuous web at 2 W/kg.

The mean power absorbed by the biological tissues of the human body at the incidence of an EM wave is given by the relation:

$$P = \sigma \frac{1}{2} |E|^2 \int dV \tag{1.2}$$

where σ is the tissue conductivity (in $[S/m]$), and $|E|$ is the intensity of the electric field within the biological tissues (in $[V/m]$).

Based on the fact that the highest average SAR values are produced by the high field strength values, we can design advanced implantable microstrip antennas, aiming at lower field electric intensities. Efforts have been made in the literature to understand the radiation mechanism of implantable antennas in order to modify its design accordingly to reduce the average SAR in human tissue.

1.2.5 Gain

One of the most important radiation characteristics of an implantable antenna is the gain. The purpose of biomedical telemetry is to transmit signals (biological signals such as the intracranial pressure) from a device that is inside the human body to an external monitoring equipment. In order to achieve that, implantable antennas must emit an adequate signal, capable of being detected by the respective external monitoring/control device, regardless of any power restrictions. Besides the limitations that we have to obey as far as the SAR values, in order to ensure patients safety, additional limits has to be fulfilled in order to avoid electromagnetic interference. Those limits refer to the maximum allowable input power of the implantable antenna. For example, the maximum radiated power to avoid EM interference is set to $25\mu W$ in the MedRadio band.

Considering the power limitations that have to be fulfilled in order to avoid EM interference, the gain of the antenna is what determines the required sensitivity of the external receiver, in order to achieve reliable telemetry of medical data. However, the design process of an implantable antenna is a trade-off between the size of the antenna and its radiation characteristics because the smaller the physical size of the implantable antenna, the greater degradation of the radiation characteristics, and vice versa. Although low gain values equate to low radiation efficiency, compromises in system EM performance are inevitable given the requirement for microscopic implant dimensions.
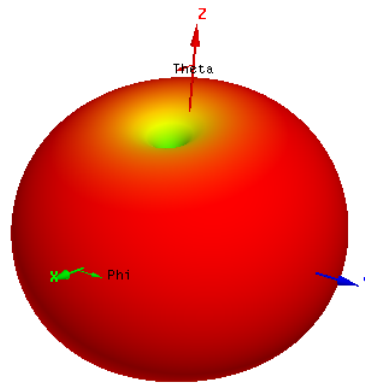

Figure 1.9   Antenna gain.

1.2.6 Power Consumption

If the transceiver of the implantable medical device operates continuously, it will consume a significant amount of energy, reducing the life of the device. Various methods are available for recharging the battery with the implantable medical de-

vice, such as the reciprocating coil method as mentioned above [27], [13]. Nevertheless, it is necessary to apply additional power conservation techniques, such as the ability to use the telemetry link only when needed. For this purpose, a dual frequency transceiver can be used, such as the commercially available Zarlink ZL 70101 transceiver. The system uses two frequency bands, one for alarm and one for transmission. The transceiver remains in standby mode with low power consumption ($1\mu W$), until it detects an alarm signal in the ISM band (2450 MHz). In normal operation, the implantable medical device is powered at full power and exchanges data. After data transfer, the device returns to standby mode.

1.2.7   Antenna Realization

Even if the antenna is properly designed in a simulation environment, the constructed one may exhibit different radiation properties from the designed on. This fact may happen due to a plethora of problems that the construction of implantable antennas are facing. One of the practical problems that may appear is in the addition of adhesive layers to connect the individual dielectric layers. Those layers significantly affect the antenna's tuning performance, by altering the tuning frequency and degrading the achieved return loss values [19]. Additional factors that may lead to a deviation of the simulated characteristics with the measured ones can originate from the measuring equipment. Radiative currents may develop on the external conductor of the coaxial power cord used to connect the antenna to the Vector Network Analyzer (VNA), which in turn degrades the quality. of measurements. Finally, an important challenge in the experimental measurement of implantable antennas is the preparation of simulations that simulate the electrical properties of biological tissues at the operating frequencies of interest, as well as the experimental measurement of their electrical properties (relative dielectric constant, ϵ_r, and conductivity, σ).

Three important aspects of construction are considered to mainly affect the final behavior of the antenna.
(1) The cutting of the substrate.
(2) The gluing of the substates.
(3) The alignment of the layers.
One of the problems that arise is that these three steps are not necessarily independent of each other. In fact, because the substrate material is quite hard and rigid, it cannot or is extremely difficult to cut once the antenna has been assembled. Also, it seems that some external alignment points are necessary for the assembly of the antenna, which are to be removed after the completion of the construction. Therefore, it is proposed to build a base that will help in the assembly of the antenna. This base ensures the correct alignment between the three layers, while at the same time it serves as a support for the antenna during the various gluing processes. Based on the above, a proposed construction methodology would include the following steps:
(1) Photolithographic masks: photolithographic masks are prepared and printed. The masks include a circular outline, which is used as a guide for cutting the antenna, four circular marks indicating the positions of the holes that match the four pins of the base during the assembly process, a square frame that matches its dimensions base and complementary alignment marks on both sides of the lower substrate.
(2) Photolithography: the substrates required for the construction of the antenna are etched through a photolithographic process, using the photolithographic masks described above.
(3) Cutting the layers: a circular cutting tool is used to cut the antenna layers. The cutting tool must have a diameter corresponding to the radius of the desired orig-

inal antenna model. The strategy adopted is to first cut the substrate to a critical depth, exactly as needed to hold the alignment points with the microfilm, but thin enough to allow easy detachment without imposing too much mechanical stress on the antenna.

(4) Antenna Assembly: the antenna is then assembled with the help of the base. The layers are aligned and welded, while the short-circuiting pin is positioned to connect the ground plate to the lower microfilm. The external conductor of the coaxial cable is connected to the ground plane of the antenna, while its internal conductor is supported at the same time on the highest and the lowest microstrip layer.

1.2.8   Experimental Evaluation

In order to evaluate the performance of the designed antenna an adequate amount of test have to take place. Those tests are classified in two categories, the in vitro and in vivo tests. For the in vitro tests a phantom is necessary. As a phantom we characterize a liquid or gel material that mimics the electrical properties of a biological tissue. It is contained in a container, where the implantable antenna is immersed and serves as an electrical substitute for the studies. For this type of tests, extreme attention has to be given in the creation of the mimicking gel in order to ensure that the antenna operates in an environment that corresponds to the oe that used during the design process [28].

Assuming that the development of the phantom is done with success, we can proceed to the appropriate measurements. Reflection coefficient measurements are made by immersing the original antenna inside an in vitro model-simulation and connecting it to a network analyzer via a coaxial signal. The fabricated prototype is immersed inside a model and measurements are taken (Figure 1.10).
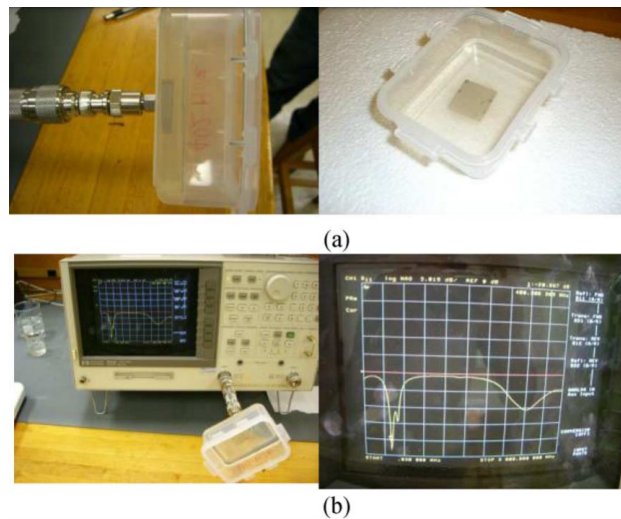
Figure 1.10   (a) Antenna embedded in skin-mimicking gel and (b) Measurement setup [16].

On the other hand, in vivo testing is using real animal tissue as an implantation cite. The main advantage of this kind of tests is the certainty that the electrical properties are the correct ones. Moreover the use of animal tissue samples offers an

easy approach to the study of frequency dependence on the electrical properties of tissues. This can be especially useful when performing measurements on implantable antennas operating in many frequency ranges.

Despite the obvious advantages of in vivo testing the use of live animals also presents particular challenges. The first step before the beginning of an in vivo test is the development of a protocol. Inside the protocol, the selection of the animal, the amount of them, the preparation, the anesthesia, the surgical procedure and other parameters have to be determined. For this reason the in vivo tests reported in the literature are very limited. A interesting study for the drop in the resonant frequency of an implantable skin antenna, using mice as models, has been studied. The antenna was surgically implanted inside the spine of three mice, followed by euthanasia after the measurements.
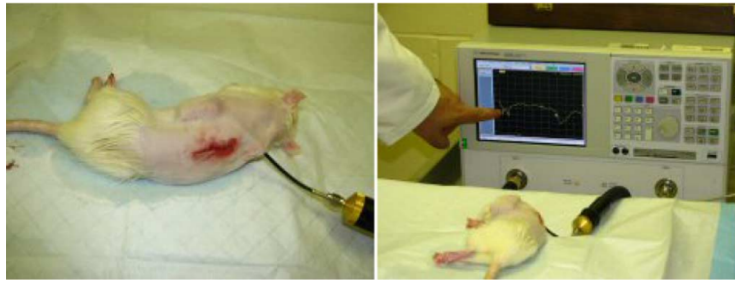
Figure 1.11   Miniaturized antenna implanted in rat [18].
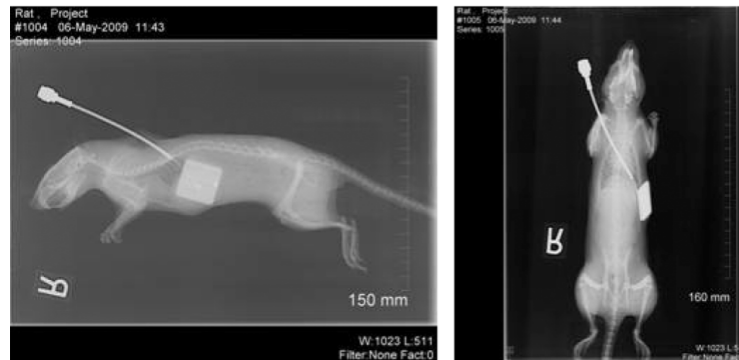
Figure 1.12   X-ray images of implantable antenna in rat [18].

1.3   *Biological Tissue*

The human body is an heterogeneous medium which consists of a variety of biological tissues (e.g. skin, muscles, blood, organs, etc.). Biological tissues contain both insulating materials (eg lipids) and electrical charges (e.g. ions) and can be considered dielectric materials, i.e. weakly conductive media.

1.3.1   Electrical Properties

The behavior of the constituent elements of matter, when is illuminated by an electromagnetic field, leads to the characterization of matter by appropriate electrical properties. Those electrical properties affect the propagation, attenuation and the reflection of an electromagnetic wave inside and outside of matter. Therefore, knowledge of the electrical properties of biological tissues is considered necessary in order to understand their interaction with the incident EM waves, and to be able to analyze the transmission and absorption of EM radiation. The exchange of energy in biological tissues takes place either through free charges or through bipolar molecules. In the presence of a time-varying EM field, the free charges are accelerated leading to the development of current and resistance losses, while the bipolar molecules are reoriented. The effects of these phenomena on the total field strength are defined with the help of the complex dielectric constant:

$$\epsilon = \epsilon_0 \epsilon_r \tag{1.3}$$

where ϵ_0 is the dielectric constant of the vacuum, and ϵ_r is the complex relative dielectric constant, defined as:

$$\epsilon_r = \epsilon_r^{'} - j\epsilon_r^{''} \tag{1.4}$$

In general, the relative dielectric constant describes the effect of each material on the electric field, while the conductivity describes the attenuation of the EM wave during its passage through the material medium. The tangent of losses is defined as:

$$tan\delta = \frac{\epsilon_r^{''}}{\epsilon_r^{'}} \tag{1.5}$$

and shows the component of electrical properties that mainly affects the electric field. The relative dielectric constant ($\epsilon_r^{'}$) and the conductivity (σ) dominate the high and low frequencies, respectively. Based on the above formulas, the complex dielectric constant of biological tissues is calculated as:

$$\epsilon = \epsilon_0 \epsilon_r^{'} - j\frac{\sigma}{\omega} \tag{1.6}$$

Therefore, the electrical properties of materials are expressed by means of the parameters $\epsilon_r^{'}$ and $\epsilon_r^{''}$, or ϵ_r and σ, as a function of frequency. Biological tissues, in particular, are heterogeneous dielectric materials and, as a result, are characterized by different relaxation times. The relative dielectric constant ($\epsilon_r^{'}$) and conductivity (σ) depend to a large extent on the type of biological tissue and the frequency of EM radiation, as follows:

(1) Tissues with high water content show higher values of relative dielectric constant and conductivity than tissues with low water content, and consequently higher losses . This behavior is due to the polar coordination of water molecules.

(2) The value of the relative dielectric constant decreases with increasing frequency, from values of 105 at a frequency of a few hundred Hz, to values less than 1 at frequencies of the order of GHz. On the contrary, conductivity increases with frequency, from values of 10^{-4} to values greater than 1, within the above frequency range.

Moreover, an important parameter for understanding the propagation of EM waves within biological tissues is skin depth, δ. Skin depth is a measure of the

distance within which the electric field is attenuated by $\frac{1}{e}$ from its original value, and is defined as:

$$\delta = \frac{1}{a} \tag{1.7}$$

At low frequencies, where the values of the relative dielectric constant are high and the conductivity values are low, the skin depth is significant and the EM wave penetrates deep into the human body. The penetration of the incident EM wave into the biological tissues decreases with frequency. At high frequencies, conductivity values are high, skin depth is reduced, and propagation is limited to the surface of the human body.

In addition, various studies have been performed on changes in the values of the electrical properties of biological tissues. Two empirical models are proposed to describe the experimental data: the first model contains two Cole-Cole functions, while the second uses a Havriliak-Negami function and a Cole-Cole function. The standard deviations recorded are in the range of 4% to 16%.

In addition, the values of the electrical properties of most types of tissues decrease with age, due to changes in their water content and organic composition. More recently, a systematic study has been published on the dependence of the electrical properties of biological tissues on age, for a large number of tissues [29]. The study presents measurements of the electrical properties of pig tissues of different ages in the frequency range from 50 MHz to 20.000 MHz, recording a significant reduction in the relative dielectric constant and conductivity with age, by a factor of 10 and 15, respectively.

1.4   Numerical Models of Biological Tissues

Computational models are extremely helpful tools in the hands of antenna designers because they provide an effective way to predict the behavior of implantable antennas EM performance in terms of radiation performance, propagation, and interaction with biological tissues. Moreover, with those tools we can calculate the SAR values in order to ensure patient's safety. Furthermore, they give us the capability to calculate the EM fields inside the biological tissues as well as the evaluation of the implantable medical devices for which it is considered difficult to carry out in vitro and in vivo experimental devices. Therefore their use is very important both in the design and in the evaluation of implantable medical devices.

1.4.1   Canonical Models

Numerical models of biological tissues of simplified geometry (e.g. spherical or cubic) are known as canonical models. Due to the simplicity that those models exhibit, they can be solved both numerically and analytically with ease. The key advantage that canonical models offer is that the are computationally efficient and sufficient to evaluate EM performance of the systems being simulated. Any resulting inaccuracies come from inaccuracy in modeling, and not from inaccuracy in arithmetic calculations but those inaccuracies can be degraded with the addition of further information in our canonical models. Furthermore, those models are extremely valuable because the phantoms that are used in in vitro test have simple geometries.

The literature gives a plethora of examples of regular models that have been used in research which models the human body. An example is the rectangular parallelepiped three-layer model that is depicted in Fig. 1.13 [30]. The model

consists of a layer simulating fat tissue placed between two layers that simulating skin and muscle.
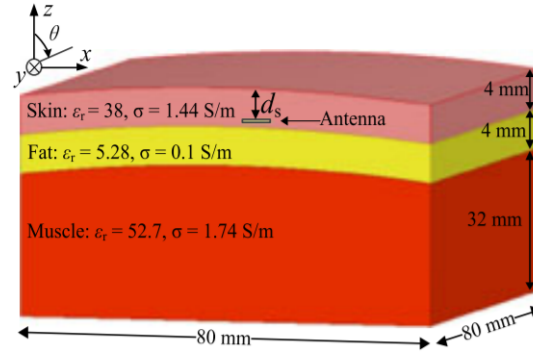
Figure 1.13   Three-layer canonical human tissue model [30].

Canonical models have also been proposed in the literature, for the simulation of the dielectric properties of a part of the human body. Homogeneous canonical models are also mentioned in the literature, but they are used for preliminary simulations. Canonical models can be more accurate and closer to reality, if layers of different tissues are present in the part of the body we want to model. The literature gives us such examples that have been used in wireless telemetry applications of implantable medical devices. Another key advantage of the canonical tissue models is the low demand on computing power and of course the smaller amount of time which is necessary for the simulations to complete.

1.4.2   Anatomical Models

Numerical models of biological tissues of realistic shape, volume and composition are called anatomical models. In order to verify the results of the performance of an implantable medical device, it is advised to use anatomical models. Those models consists of a huge amount of cubic elements, known as voxels, in order to simulate human parts with great accuracy. Every voxel is assigned with appropriate electrical properties of a specific biological tissue. The largest the amount of voxels that the mesh has, the greater the illusion of a continuous change in the biological tissue (for example from skin to muscle). Selecting the appropriate values of electrical properties in each cubic element, makes it possible to accurately model specific biological tissues and organs.

The development of anatomical numerical models is one of the greatest challenges in the field of numerical bioelectromagnetism, and today it is facilitated by the rapid scientific developments in the field of medical imaging. Thanks to the increase in computing power and the reduction in the cost of computing resources, there is a tendency to develop more and more detailed anatomical structures. It is noted that the highest complexity of anatomical models, today, reaches 50 types of tissues, while the optimal resolution is of the order of 1 mm.

In most studies data for the design of anatomical models are obtained by Magnetic Resonance Imaging (MRI), or Computed Tomography (CT). MRI and CT provide images of the human body in cross sections at a distance from each other. The analysis in each section is of the order of a few millimeters. Despite the fact that several of the tissues are visible on MRI and CT images, the application of segmentation techniques is considered necessary for their accurate conversion into
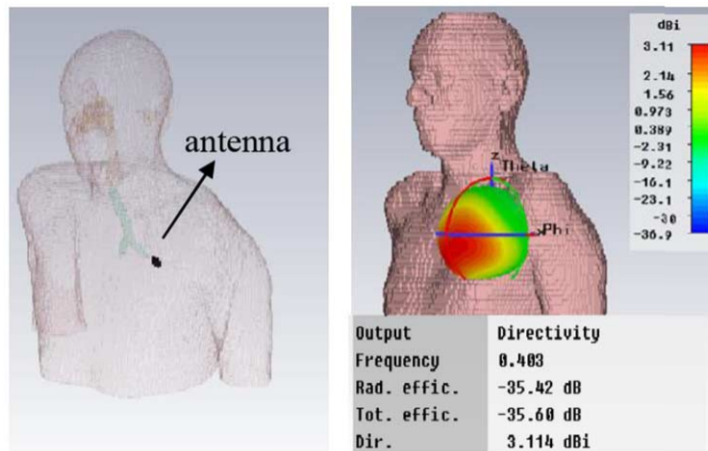
Figure 1.14 Implantation site (left figure) and antenna radiation (right figure) [31].

"tissue maps". This process is generally complex and time consuming and takes place semi-automatically, although automatic methods have been also reported. It is noted that even if the software is implemented for automated image segmentation, further manual verification and correction of the results are also considered important and necessary.

1.5 Antenna Design

1.5.1 Tissue Models

The main goal of our research is to design an antenna able to operate correctly inside the human chest, in order to be implemented in applications such as the pacemaker. Moreover, one of our ultimate tasks was to design this antenna in such a way, in order to operate in both MedRadio and ISM frequency bands. This task was very demanding if we consider the very small size of the implantable antenna, ($29mm^3$). So in order to achieve it, a very large amount of simulations was carried out, leading to a new, novel, antenna design. The motivation behind this demand was the ability of the antenna to use wake up and sleep signals. This operation gives the antenna the capability to consume power only when it is necessary, for example when the doctor wants to extract some data from the pacemaker. Taking into account this fact, it is easily understood that the lifetime of the battery is expanding, leading to fewer surgical operations as far as the replacement of the device's battery. Furthermore, it should be highlighted that the final size of the antenna makes it one of the smallest in the literature.

As a first step of the antenna design procedure, we considered a canonical cubic human chest model filled with material mimicking the skin tissue electrical properties, at the appropriate simulation frequency. Then we conduct simulations in order to make the antenna radiate based on our demands. The implantation cite scenario is depicted in the Figure 1.16.

The next step in the design process is to use a more detailed model of the human chest, leading to more accurate results as far as it concerns the antenna's
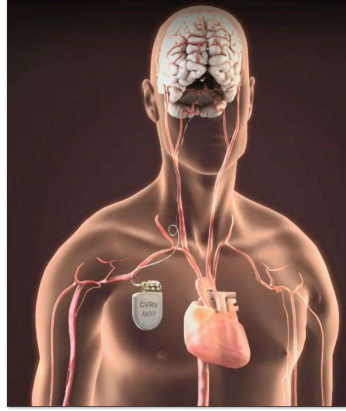
Figure 1.15   Implantable antenna for the case of a pacemaker application.
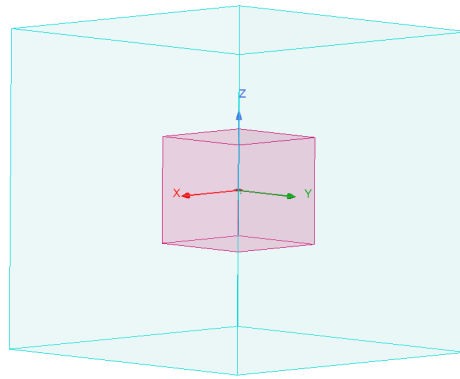
Figure 1.16   Canonical cubic model mimicking skin tissue properties.

performance. In order to achieve that, we implement it to the previous implantation Figure 1.16 using more layers, such as fat and muscle. It should be noted that the size and the values of the electrical properties of each human tissue layer are in very close proximity to the real ones [3]. So, the model that was used is depicted in Figure 1.17.

Now that the implantation cite has changed, we conducted a large number of simulations, in order to optimize the antenna's performance characteristics. The reason behind this is that the antenna is very sensitive to the environment in which it is working. So, detuning effects are very possible to take place, leading to huge changes in the antenna design. In Figure 1.17 the three-layer canonical human chest model is depicted, containing the dimensions and the values of the electrical properties of the implantation cite, in the appropriate frequency [31].

1.5.2   Simulation Software

The antennas are designed with the help of Ansoft HFSS software, which uses the Finite Element method (FEM) and it is highly used for a wide variety of simulations in the context of electromagnetic applications. An iterative tetrahedron meshing is employed using automated refinement, with mesh perturbation by 30% between
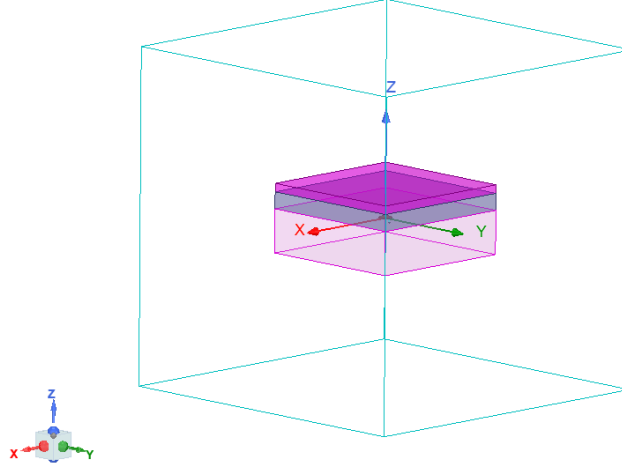
Figure 1.17   Canonical three-layer cubic model mimicking human chest.
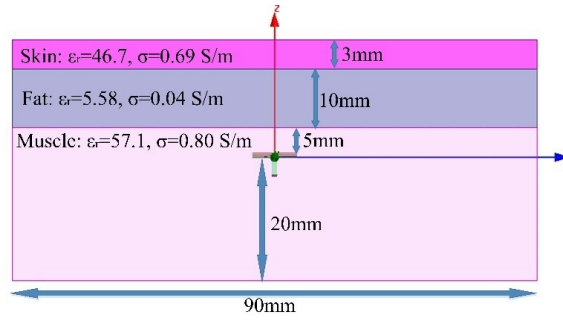
Figure 1.18   Canonical three-layer cubic model mimicking human chest.

each pass [32]. The mesh refinement procedure stops when the maximum change in the reflection coefficient magnitude (|S11|) between two consecutive passes is less than 0.02. In case that the previous condition is not accomplished a maximum number of 20 passes is set. Also, an air box, with quarter wavelength distance from all the radiating surfaces, is set for numerical stability of the simulations. The central frequency of the FEM solver is 402 MHz and 2.45 GHz for the MedRadio and ISM bands, respectively. A frequency sweep of $\pm100MHz$ around those frequencies are computed, with 25000 frequency points.

1.5.3   Proposed Antenna Model

The layout of the proposed antenna is shown in Fig. 1.19 The antenna size is $\pi \times 3.8^2 \times 0.65mm^3$ In order to satisfy the requirement for biocompatibility the ceramic alumina 99.5% ($\epsilon_r = 9.8$, $\sigma = 1.904 \times 10^{-7}S/m$) is used as a lower (LS) and upper (US) substrate and also as superstrate material [2], as shown in Fig. 1.19(a-d).

The antenna model consists of a circular ground plane (GP) (Fig. 1.19(a)) with radius $R_g = 3.8mm$ and two circular vertically stacked metallic radiating patches (Fig. 1.19(b,c)), with radius $R_p = 3.6mm$. The radiating patches include
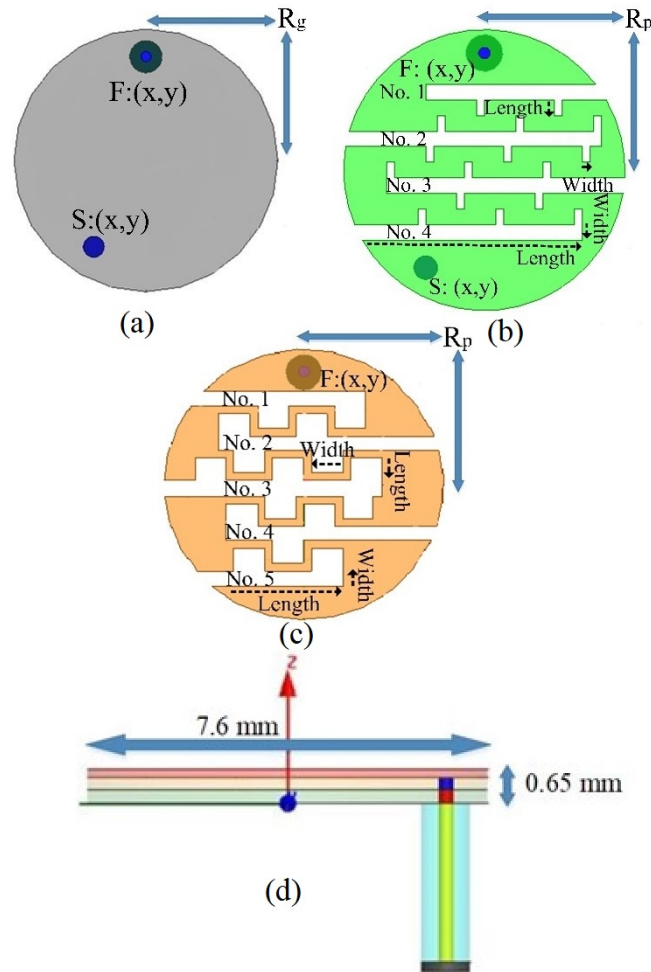
Figure 1.19 Implantable antenna design: (a) ground plane, (b) lower patch, (c) upper patch and (d) XZ side view.

meanders and vertical protrusions to them in order to increase the effective length of the current flow and reduce the antenna size [1],[2]. Both lower (LP) and upper (UP) patches are printed on ceramic alumina, with radius 3.8 mm and thickness 0.25 mm. Additionally, a 0.15 mm thick ceramic alumina superstrate layer covers the antenna structure, in order to ensure biocompatibility. The distance between two adjacent meanders is 0.8 mm, with constant width of 0.4 mm throughout the design process, and the length of each one of them is shown in Table 1.1. The number of vertical protrusions on each meander differs, as shown in Fig. 1.19, and the distance between two adjacent protrusions is 0.8 mm for the LP and 0.4 mm for the UP. Moreover, the width and the length of its protrusion are depicted in Table 1.2.

It should be noted that the idea behind the vertical protrusions is the ability of the antenna to radiate in two different frequency bands. Moreover, the design

Table 1.1   Meander lengths of the proposed dual-band antenna.

Meander No.	1	2	3	4	5
LP[mm]	4.7	6.7	6.2	6	—
UP[mm]	4.4	5.8	5.8	5.5	3.8

Table 1.2   Protrusion dimensions of the proposed antenna.

LP Protrusions [mm]		UP Protrusions [mm]	
Length	Width	Length	Width
0.4	0.2	0.7	0.6

of the proposed antenna offers a wide variety of degrees of freedom, something which is crucial in demanding applications such as the pacemaker or the human eye implant. So, this design is very flexible and can be used in different applications, which include different implantation cites. Optimization simulations are necessary in order to find the correct dimensions of the meanders and the vertical protrusions.

Both radiating patches are excited through a 50-ohm coaxial cable ($F : x = -3$ mm, $y = 0$ mm) EZ-47. A shorting pin placed at ($S : x = 2.5$ mm, $y = -1.5$ mm), with radius $R_s = 0.3mm$, connects the GP with the LP aiding to antenna size reduction.

As a final step we used the LPKF machine to realize the antenna that was designed in the HFSS commercial software. In the figures below (Figures 1.20 to 1.22) the patches/layers of the antenna are depicted.

Figure 1.20   Ground plane of the proposed implantable antenna.
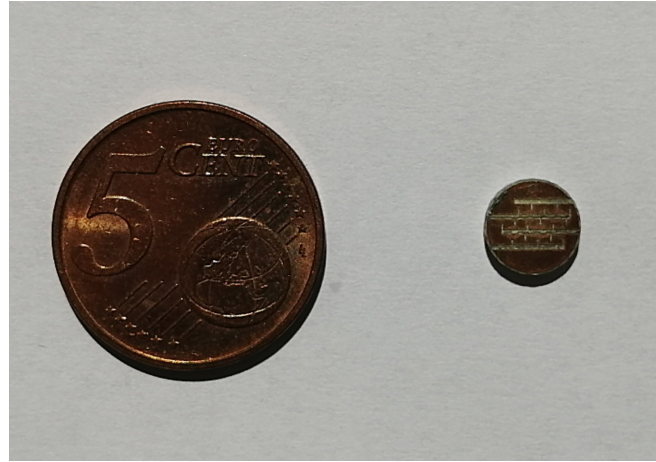
Figure 1.21   Lower patch of the proposed implantable antenna.

Figure 1.22   Upper patch of the proposed implantable antenna.

1.5.4   Proposed Antenna Performance

The values of the reflection coefficients ($|S_{11}|$), of the antenna in the resonant frequencies, inside a three-layer human chest model are illustrated in Fig. 1.23. A broad BW of $38.7 MHz$ ($377 - 415.7$ MHz) in the MedRadio band and 69.2 MHz ($2.389 - 2.459$ GHz) in ISM band is attained. It should be highlighted that the antennas BW includes all the MedRadio band, exhibiting very low values of $|S_{11}|$, as depicted in Fig. 1.25.

Also, the antenna achieves a -55 dB and -52 dB gain in MedRadio and ISM bands, respectively. The radiation patterns in MedRadio and ISM bands are shown in Fig. 1.23 and Fig. 1.24 respectively. The antennas' impedance at resonance in MedRadio and ISM bands is respectively $Z_{MedRadio} = 46.98 + 0.064j$ and $Z_{ISM} = 50.22 - 0.60j$, which are very close to the coaxial cable's impedance, $Z_{cable} = 50\Omega$, leading to mismatching avoidance and can be seen in Fig. 1.27 and Fig. 1.28 respectively.

In order to ensure patients safety, radiation of implantable antennas should
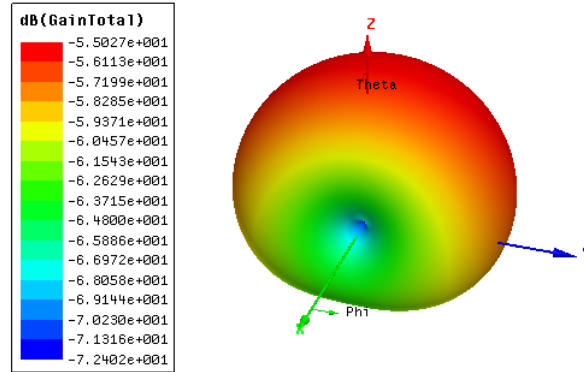
Figure 1.23   Radiation pattern of the proposed antenna in the MedRadio band.
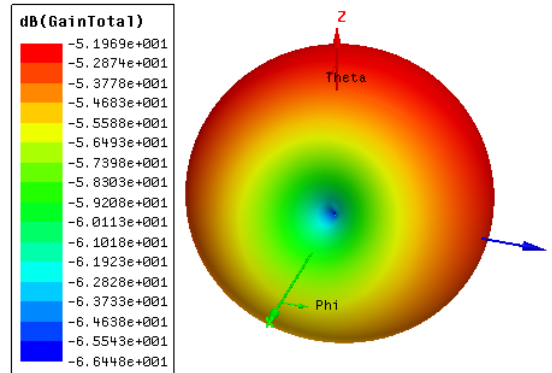
Figure 1.24   Radiation pattern of the proposed antenna in the ISM band.

Table 1.3   Safety performance of the proposed implantable antenna.

	Maximum Allowed Net Input Power	
Model	$P_{1999}[mW]$	$P_{2005}[mW]$
Chest	0.2	0.7

produce maximum SAR values, that conform to the IEEE C95.1-1999 (P_{1999}) [33] and IEEE C95.1-2005 (P_{2005}) [34] safety guidelines. The maximum allowed input power is calculated based on the worst-case scenario of the SAR distribution, which corresponds to the MedRadio band and is depicted in Table 1.3.

In addition, a comparison between dual band implantable antennas is carried out in Table 1.4. It should be highlighted that the majority of the dual band antennas found in the literature have dimensions that may exclude them from use in some applications where the available space is very limited, such as human eye implantation. However, the antenna proposed in this work does not face such a problem because has suitable dimensions for implantation in the human eye. Also, it is known that the larger the antenna dimensions the better the radiation characteristics. So, some antenna designs may have better characteristics than the proposed one.
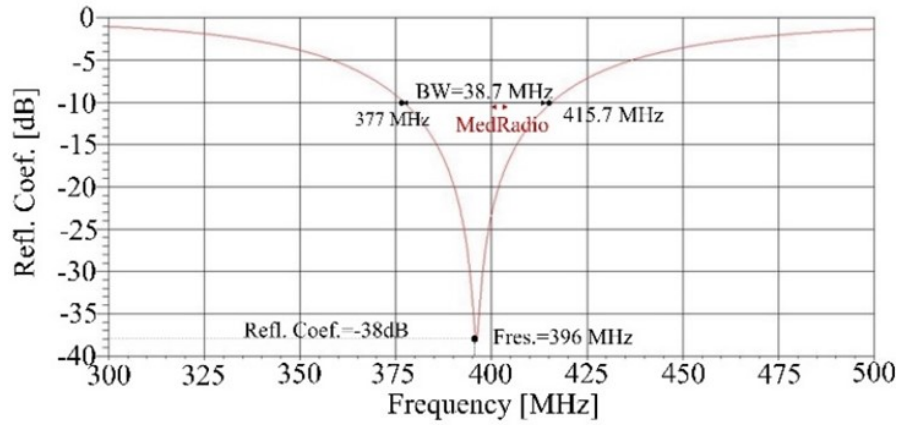
Figure 1.25   Reflection Coefficient vs Frequency inside a three-layer human chest model in the MedRadio band.
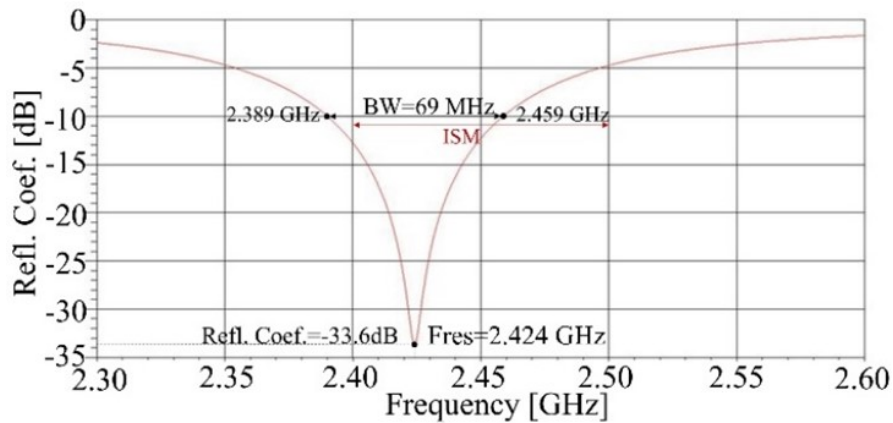
Figure 1.26   Reflection Coefficient vs Frequency inside a three-layer human chest model in the ISM band.

1.6   *Comparative Study of Antenna's Miniaturization Techniques*

In this section we are going to demonstrate a comparative study of the miniaturization techniques which is used in order to reduce the antenna's size. As we mentioned earlier, the miniaturization techniques that are proposed in the literature for implantable microstrip antennas are as follows:
(1) Use of high dielectric constant materials.
(2) Elongation of the current's stream flow path at the radiating patch.
(3) Use of shorting pin.
(4) Stucked patches.
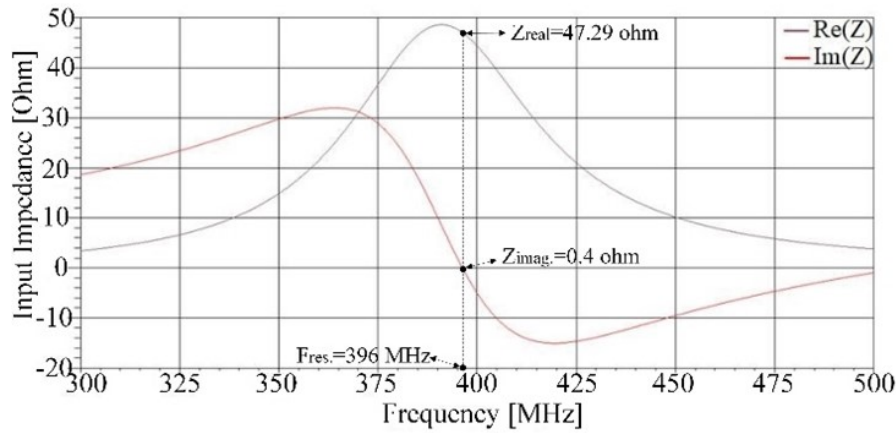
Figure 1.27   Input Impedance vs Frequency inside a three-layer human chest model in the MedRadio band.
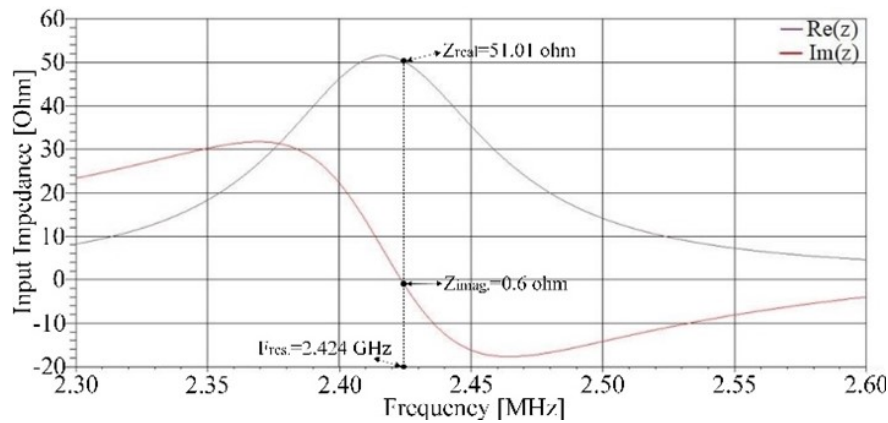
Figure 1.28   Input Impedance vs Frequency inside a three-layer human chest model in the ISM band.

Table 1.4   Comparison between the proposed antenna and antennas in the literature.

Antenna	Volume	Maximum Dimension	BW MedRadio	BW ISM	Gain MedRadio	Gain ISM
[Ref]	$[mm^3]$	$[mm^3]$	$[MHz]$	$[MHz]$	$[dB]$	$[dB]$
[35]	31.5	8.75	28	88	−39	−22
[36]	49	17	74	1000	−33	−16
[37]	152.4	12	172	350	−	−
[38]	642.62	23	30	168	−36.7	−27.1
This Work	29	7.6	38.7	69.2	−50	−52

The combination the aforementioned miniaturization techniques during the antenna design is a must when the goal is to reduce the antenna's dimensions as much as possible. But we have to keep in mind that as smaller as the antenna gets,

a lot of parameters have to be considered. First of all, we should bear in mind that when the antenna gets smaller and smaller it is more sensitive to detuning effects. Moreover, the performance of the antenna is degrading, because the size of the radiating patches is getting smaller.

In order to make the design process of antennas that intend to have the smallest possible size easier, a comparison study was conducted. In this study we present all the possible combinations of the miniaturization techniques, starting from a simple circular patch antenna. It should be noted that the antenna is operating in free space, in order to verify the real reduction that every combination provides. If the above simulations were carried out inside a human tissue model, the dielectric properties of the environment would lead to a reduction of the antenna, due to the higher dielectric constant of the surrounding environment. Another detail, that should be highlighted, is the use of Rogers3210 ($\epsilon_r = 10.2$) for the high dielectric constant material and the Rogers5880 ($\epsilon_r = 2.2$) for the low dielectric constant material. The dimension of the height in every Roger3210 dielectric layer is $h = 0.635$ mm and for the Roger5880 the height is $h = 1.588$ mm. The reason behind this decision is that the company provides those specific materials in these dimensions as it can be seen from their data-sheet. Last but no least, it should be noted that the designing of an antenna for every possible combination of the miniaturization techniques, needed a significant amount of time, because every case demanded an antenna design from scratch, leading to exhaustive simulations and optimizations in order to find the smallest size antenna for every case. In Table 1.5, the antennas with the smallest size for every case are depicted. Moreover, a percentage of the reduction of the antenna's radius and volume is shown, respectively.

As it can be seen from Table 1.5, every miniaturization technique leads to different size/volume reduction of the microstrip patch antenna. Moreover, an interesting outcome of this comparative study is that the use of more miniaturization techniques does not lead to a greater reduction in the size/volume of the antenna. More specifically, in the case no.14 the antenna is designed with Rogers3210 and a shorting pin along with meanders is used. On the other hand, in case no.15 the antenna is designed with Rogers5880 and all the miniaturization techniques are taking place, but the no.14 case antenna exhibits lower values of both radius and volume. An interesting extension of this study would be a comparison of the radiation characteristics of all the aforementioned antennas, such as gain, SAR, efficiency etc.

Table 1.5 Miniaturization Techniques Comparative Study for the Case of Circular Microstrip Patch Antenna.

	Simulation Setup	Rogers 5880	Rogers 3210	Double Stacked	Shorting Pin	Meandered	% Radius Reduction	% Volume Reduction
1	$R = 149$ mm, $V = 110757.44$ mm^3	x	-	-	-	-	0	0
2	$R = 69.5$ mm, $V = 9635.92$ mm^3	-	x	-	-	-	−53.36	−91.3
3	$R = 42$ mm, $V = 8800.33$ mm^3	x	-	-	x	-	−71.81	−92.05
4	$R = 22$ mm, $V = 965.54$ mm^3	-	x	-	x	-	−85.23	−99.13
5	$R = 149$ mm, $V = 221514.88$ mm^3	x	-	x	x	-	0	+100
6	$R = 69.5$ mm, $V = 19271.84$ mm^3	-	x	x	-	-	−53.36	−82.59
7	$R = 110$ mm, $V = 60365.07$ mm^3	x	-	-	-	x	−26.17	−45.50
8	$R = 40$ mm, $V = 3191.86$ mm^3	-	x	x	-	x	−73.15	−97.12
9	$R = 88$ mm, $V = 77267.30$ mm^3	x	-	x	-	x	−40.94	−30.24
10	$R = 35$ mm, $V = 4887.53$ mm^3	-	x	x	-	x	−76.51	−95.59
11	$R = 42$ mm, $V = 8800.39$ mm^3	x	-	x	x	-	−71.81	−92.05
12	$R = 20$ mm, $V = 1595.93$ mm^3	-	x	x	x	-	−86.58	−98.56
13	$R = 30$ mm, $V = 4489.96$ mm^3	x	-	-	x	x	−79.87	−95.95
14	$R = 16$ mm, $V = 510.70$ mm^3	-	x	-	x	x	−89.26	−99.54
15	$R = 30$ mm, $V = 897.99$ mm^3	x	-	x	x	x	−79.87	−99.19
16	$R = 10$ mm, $V = 398.98$ mm^3	-	x	x	x	x	−93.28	−99.64

1.7   Conclusion

The main design advantage of this antenna is that it offers many degrees of freedom, such as the number and size of meanders and protrusions, that can be optimized in order to achieve the desired results. So, this flexibility in the design made possible, for such a small antenna, to resonate in both MedRadio and ISM bands. Furthermore, during the optimization process, the antenna was resonating in both bands and in many other optimized parameter values (lengths, widths etc.) but here the biggest BW case is presented. Certainly the proposed antenna covers the MedRadio and ISM bands. More specifically, in Fig. 1.25 and Fig. 1.26 we can see that the proposed antenna's bandwidth is including the MedRadio band and a large part of the ISM band. Finally, the antennas gain is relatively small, but it can be improved using various techniques such as parasitic patch [39], dual feed [39] and reflecting layer [35], [40]. As a next step the antenna will be implanted inside an anatomical human chest model, to verify the antenna's characteristics and performance inside a more realistic tissue model.

In this study, a novel dual-band miniature PIFA was presented for human chest implantation applications, such as pacemakers. The dual band design allows the IMD to switch between sleep and wake-up modes. The proposed antenna volume is 29 mm^3 and a broad BW of 38.7 MHz and 69.2 MHz in MedRadio and ISM frequency bands, respectively is achieved. The radiation pattern of the antenna is omnidirectional, with maximum gain of -55 dB and -52 dB in the MedRadio and ISM bands, respectively. Also, the antenna achieves great impedances at the resonance frequencies, in both MedRadio and ISM bands ($Z_{MedRadio} = 46.98 + 0.064j$ and $Z_{ISM} = 50.22 - 0.60j$).

Electromagnetic Scattering by Highly Inhomogeneous Gyrotropic Cylinders using CFVIEs

A coupled-field volume integral equation (CFVIE) method for electromagnetic (EM) scattering on electrically large, highly inhomogeneous gyrotropic circular cylinders, under normal incidence, is developed in this work. The CFVIEs are solved by cylindrical Dini series expansion (CDSE) method, where the unknown fields are expanded by entire domain orthogonal vectorial basis functions. The main advantage of the present method is that it permits the scatterer to have continuously varying highly inhomogeneous gyrotropic characteristics, i.e., the constitutive parameters of the cylinder can be highly inhomogeneous in both gyroelectric and gyromagnetic tensors. Initially, the two-dimensional (2-D) Green's function (GF) is expanded in a tensorial form using the cylindrical vector wave functions (CVWFs). Then, by employing the CDSE for the unknown fields, the 2-D volumetric integrals are carried out analytically, reducing the CFVIEs to a set of algebraic equations. The method is validated by comparisons with the exact solution based on the separation of variables method (SVM) for homogeneous isotropic/gyroelectric/gyromagnetic cylinders, with HFSS commercial software for two- and three-layered gyroelectric/gyromagnetic cylinders, as well as with the recently developed hybrid projection method (HPM) for electrically large continuously varying highly inhomogeneous isotropic cylinders. Results for combined gyroelectric-continuously varying highly inhomogeneous isotropic cylinders are presented and discussed.

2.1 Introduction

In the recent years, cylindrical structures have constituted the platform for highlighting and bringing to the foreground various interesting phenomena, mainly in the area of photonics. These include the design of gradient-index lens for invisibility

applications [41, 42], magneto-optical materials-aided applications for active tuning of directional scattering in single or in a collection of cylinders [43-45], cloaking-to-superscattering operation using phase-change materials [46], radially anisotropic nanowires for superscattering operation [47], cylindrical radio frequency waves in tokamak plasmas [48, 49], tuning of plasmonic cloaks with external magnetic fields [50], the investigation of cavity modes in metamaterial rings [51], engineering of rod-type metamaterials at optical frequencies [52], or the development of electromagnetic black holes [53-57].

EM scattering by cylinders, either isotropic/anisotropic or homogeneous and inhomogeneous, was the subject of research for many researchers. The exact solution for the scattering by homogeneous and stratified plasma cylinders, under normal incidence, has been documented in [58]. Then, the exact solution for the scattering from a homogeneous gyrotropic cylinder, also under normal incidence, and its TM/TE separation, has been presented in [59]. Matrix formulation-based method for homogeneous gyrotropic cylinders has been proposed in [60]. Scattering of obliquely incident waves by homogeneous cylinders was studied in [61] by means of a volume integral equation (VIE) formulation. A finite element method (FEM) for obliquely incident waves on inhomogeneous anisotropic cylinders has been applied in [62] and numerical results for homogeneous structures have been presented. Circular homogeneous cylinders have been examined in [63] and [64] for normal and oblique incidence, respectively, then, a surface integral representation for homogeneous anisotropic cylinders has been developed in [65] based on a mapping technique. Equivalence theorem-based combined field surface integral equation formulations for arbitrarily shaped homogeneous anisotropic cylinders, including perfectly conducting objects, have been applied in [66-68]. In [69, 70], the FEM-multifilament current method and the measured equation of invariance-based finite difference method, have been applied for the EM scattering of normally incident waves by gyrotropic inhomogeneous cylinders. More recently, Volterra integral equation formulation for the oblique scattering by radially inhomogeneous dielectric cylinders has been developed in [71], while, a multifilament current method [72] has been extended to support EM scattering by anisotropic cylinders under normal incidence.

In this work we develop a CFVIE method for the EM scattering by normally illuminated electrically large, continuously varying highly inhomogeneous gyroelectric/gyromagnetic circular cylinders, with infinite extension in z-direction. The anisotropy is described by the inhomogeneous permittivity and permeability tensors $\boldsymbol{\epsilon}(\boldsymbol{\rho})$, $\boldsymbol{\mu}(\boldsymbol{\rho})$, respectively—their precise expression will be given below—with $\boldsymbol{\rho}$ being the position vector in the polar coordinate system. The novel points of our work include:

(i) Development of a full-wave CFVIE-CDSE method based on entire domain orthogonal cylindrical vectorial basis functions. In particular, the CFVIEs are solved by CDSE method, where the unknown fields are expanded by the divergenceless Dini-type CVWFs $\mathbf{M}_{ml}(k_{ml}^M, \boldsymbol{\rho})$, $\mathbf{N}_{ml}(k_{ml}^N, \boldsymbol{\rho})$, and by the irrotational Dini-type CVWF $\mathbf{L}_{ml}(k_{ml}^L, \boldsymbol{\rho})$. The cylindrical Dini-type vectors are introduced for the first time here.

(ii) Establishment of fully orthogonal properties for the Dini-type CVWFs, within the domain of the cylinder. Specifically, Dini-type CVWFs feature the special arguments k_{ml}^M, k_{ml}^N, k_{ml}^L (see above). For these CVWFs to be fully orthogonal, k_{ml}^M, k_{ml}^N, k_{ml}^L must satisfy appropriate eigen-equations which we first report here.

(iii) Analytical reduction of the original CFVIEs to algebraic sets of equations. This is the main advantage of our formulation since the specific Dini-type CVWFs allow

to analytically integrate the 2-D volumetric integrals, thus leading to the analytical composition of one part of the final system matrix. The remaining part of the final system matrix is populated after application of the Galerkin technique on the constitutive relation connecting the electric field $\mathbf{E}(\boldsymbol{\rho})$, the inverse permittivity tensor $\boldsymbol{\epsilon}^{-1}(\boldsymbol{\rho})$, and the electric displacement $\mathbf{D}(\boldsymbol{\rho})$, as well as on the dual relation connecting the magnetic field $\mathbf{H}(\boldsymbol{\rho})$, the inverse permeability tensor $\boldsymbol{\mu}^{-1}(\boldsymbol{\rho})$, and the magnetic flux density $\mathbf{B}(\boldsymbol{\rho})$.
(iv) Rigorous construction of a 2-D tensorial GF, similar to the three-dimensional (3-D) one of [73, p. 1875]. This tensorial form is a dyadic expansion of the free space 2-D GF into divergenceless and irrotational CVWFs, and it is required to allow for the analytical integration of the involved 2-D volumetric integrals.

Within the CFVIE-CDSE approach, continuously varying highly inhomogeneous permittivity/permeability profiles, including anisotropic ones, can be readily considered, since the material properties are already incorporated in the constitutive relations and the solution is obtained by simple integration over the inhomogeneous anisotropic region of the cylinder. In the past, the VIE-Dini series expansion (DSE) and the CFVIE-DSE were developed for the respective 3-D problems regarding EM scattering by anisotropic spheres [74, 75], but certainly the current work concerns a different problem and requires development from the scratch. The CFVIE-CDSE is exhaustively validated by comparisons with the exact SVM solution for isotropic/gyroelectric/gyromagnetic cylinders [59], for both TE and TM incidence, with the HFSS commercial software for two- and three-layered gyroelectric/gyromagnetic cylinders, as well as with HPM [41] for electrially large continuously varying highly inhomogeneous isotropic cylinders.

2.2   *Coupled fields volume integral equations*

Using matrix notation where each vector is represented by a 3×1 matrix and a dyad by a 3×3 matrix, the CFVIEs for the 2-D case—obtained from the respective ones for the 3-D case [75]—are

$$\begin{bmatrix} \mathbf{E}(\boldsymbol{\rho}) \\ \mathbf{H}(\boldsymbol{\rho}) \end{bmatrix} = \begin{bmatrix} \mathbf{E}^{\mathrm{inc}}(\boldsymbol{\rho}) \\ \mathbf{H}^{\mathrm{inc}}(\boldsymbol{\rho}) \end{bmatrix} + \begin{bmatrix} k_0^2 \mathbb{I} + \nabla\nabla^T & -ik_0\sqrt{\frac{\mu_0}{\epsilon_0}}\nabla\times \\ ik_0\sqrt{\frac{\epsilon_0}{\mu_0}}\nabla\times & k_0^2 \mathbb{I} + \nabla\nabla^T \end{bmatrix}$$

$$\int_{\boldsymbol{\rho}' \in S} g(\boldsymbol{\rho} - \boldsymbol{\rho}') \begin{bmatrix} \mathbb{X}_{\mathrm{e}}(\boldsymbol{\rho}') & 0 \\ 0 & \mathbb{X}_{\mathrm{m}}(\boldsymbol{\rho}') \end{bmatrix} \begin{bmatrix} \mathbf{E}(\boldsymbol{\rho}) \\ \mathbf{H}(\boldsymbol{\rho}) \end{bmatrix} \mathrm{d}\boldsymbol{\rho}', \boldsymbol{\rho} \in \mathbb{R}^2. \qquad (2.1)$$

In the left hand-side of (2.1), which represents the total $\mathbf{E}(\boldsymbol{\rho})$, $\mathbf{H}(\boldsymbol{\rho})$, we have grouped the 3-vectors $\mathbf{E} = [E_\rho, E_\varphi, E_z]^T$, $\mathbf{H} = [H_\rho, H_\varphi, H_z]^T$—with T denoting transposition—into a 6-vector $[\mathbf{E}, \mathbf{H}]^T$. Similarly, the 6-vector $[\mathbf{E}^{\mathrm{inc}}, \mathbf{H}^{\mathrm{inc}}]^T$ represents the electric and magnetic fields of the incident plane wave. Moreover in (2.1), $S = \{(\rho, \varphi) \in \mathbb{R}^2 \mid 0 \leqslant \rho \leqslant a, 0 \leqslant \varphi < 2\pi\}$ is the transverse domain of the cylinder having radius a, $k_0 = \omega\sqrt{\epsilon_0\mu_0}$ is the free space—i.e., the background medium—wavenumber with ϵ_0 and μ_0 the free space premittivity and permeability respectively, $\mathbb{I}$ is the unity dyadic, $g(\boldsymbol{\rho} - \boldsymbol{\rho}') = -i/4H_0^{(2)}(k_0|\boldsymbol{\rho} - \boldsymbol{\rho}'|)$—with $H_0^{(2)}$ the Hankel function of the second kind and zeroth order; from now on, the superscript (2) is omitted for simplicity—is the 2-D free space GF [41], and $\mathbb{X}_{\mathrm{e}}(\boldsymbol{\rho}) = \boldsymbol{\epsilon}(\boldsymbol{\rho})/\epsilon_0 - \mathbb{I}$, $\mathbb{X}_{\mathrm{m}}(\boldsymbol{\rho}) = \boldsymbol{\mu}(\boldsymbol{\rho})/\mu_0 - \mathbb{I}$ are the normalized tensorial electric and magnetic contrast functions. From the form of GF, the adopted time dependence is $\exp(i\omega t)$. The inhomogeneous permittivity and permeability tensors appearing in the contrast functions are given by

$$\boldsymbol{\epsilon}(\boldsymbol{\rho}) = \begin{bmatrix} \epsilon_1(\boldsymbol{\rho}) & i\epsilon_2(\boldsymbol{\rho}) & 0 \\ -i\epsilon_2(\boldsymbol{\rho}) & \epsilon_1(\boldsymbol{\rho}) & 0 \\ 0 & 0 & \epsilon_3(\boldsymbol{\rho}) \end{bmatrix}, \boldsymbol{\rho} \in S,$$

$$\boldsymbol{\mu}(\boldsymbol{\rho}) = \begin{bmatrix} \mu_1(\boldsymbol{\rho}) & i\mu_2(\boldsymbol{\rho}) & 0 \\ -i\mu_2(\boldsymbol{\rho}) & \mu_1(\boldsymbol{\rho}) & 0 \\ 0 & 0 & \mu_3(\boldsymbol{\rho}) \end{bmatrix}, \boldsymbol{\rho} \in S, \tag{2.2}$$

while, for the background medium $S_0 = \mathbb{R}^2 \setminus S$, the relations $\boldsymbol{\epsilon}(\boldsymbol{\rho}) = \epsilon_0\mathbb{I}$, $\boldsymbol{\mu}(\boldsymbol{\rho}) = \mu_0\mathbb{I}$, $\boldsymbol{\rho} \in S_0$, hold. It should be clarified that each element in (2.2) can be further written as $\epsilon_j = \epsilon_{jr}\epsilon_0$ and $\mu_j = \mu_{jr}\mu_0$, $j = 1, 2, 3$, with ϵ_{jr}, μ_{jr} the respective relative values.

2.3   Two dimensional Green's function

In this Section we present the rigorous construction of a 2-D tensorial GF $\mathbb{G}(\boldsymbol{\rho} - \boldsymbol{\rho}') = \mathbb{I}g(\boldsymbol{\rho} - \boldsymbol{\rho}')$, similar to the 3-D one of [73, p. 1875]. We begin by expanding the scalar 2-D GF as [76]

$$g(\boldsymbol{\rho} - \boldsymbol{\rho}') = -\frac{i}{4}H_0(k_0|\boldsymbol{\rho} - \boldsymbol{\rho}'|) = -\frac{i}{4}\sum_{m=-\infty}^{\infty} \begin{cases} \psi_m^{(1)}(\rho', \varphi)\psi_m^{(4)*}(\rho, \varphi'), & \rho > \rho' \\ \psi_m^{(1)}(\rho, \varphi)\psi_m^{(4)*}(\rho', \phi'), & \rho < \rho' \end{cases}$$

$$= -\frac{i}{4}\sum_{m=-\infty}^{\infty} \psi_m^{(1)}(\rho_<, \varphi)\psi_m^{(4)*}(\rho_>, \varphi'), \tag{2.3}$$

where $\psi_m^{(1)}(\rho, \varphi) = J_m(k_0\rho)e^{-im\varphi}$ and $\psi_m^{(4)}(\rho, \varphi) = H_m(k_0\rho)e^{-im\varphi}$ are the generating functions—with J_m the Bessel function and H_m the Hankel function of the second kind—while $\rho_< = \min\{\rho, \rho'\}$ and $\rho_> = \max\{\rho, \rho'\}$. In (2.3), the asterisk denotes complex conjugation and is applied only in the exponential function in $\psi_m^{(4)}$. To get the desired tensorial form, we apply on the product $\psi_m^{(1)}\psi_m^{(4)*}$ the tensorial definitions of the $\mathbf{M}_m\mathbf{M}_m^T$, $\mathbf{N}_m\mathbf{N}_m^T$ and $\mathbf{L}_m\mathbf{L}_m^T$ dyads [73, p. 1874], where now $\mathbf{M}_m$, $\mathbf{N}_m$, $\mathbf{L}_m$ are the standard CWVFs which, when $\partial/\partial z = 0$, are given by [77, 78]

$$\mathbf{M}_m(k_0, \boldsymbol{\rho}) = e^{-im\varphi}\Big[-i\frac{m}{\rho}Z_m(k_0\rho)\hat{\rho} - \frac{\mathrm{d}Z_m(k_0\rho)}{\mathrm{d}\rho}\hat{\varphi}\Big],$$

$$\mathbf{N}_m(k_0, \boldsymbol{\rho}) = e^{-im\varphi}k_0Z_m(k_0\rho)\hat{z},$$

$$\mathbf{L}_m(k_0, \boldsymbol{\rho}) = e^{-im\varphi}\Big[\frac{\mathrm{d}Z_m(k_0\rho)}{\mathrm{d}\rho}\hat{\rho} - i\frac{m}{\rho}Z_m(k_0\rho)\hat{\varphi}\Big]. \tag{2.4}$$

In (3.4) Z_m can be either J_m or H_m. Therefore we get

$$\mathbb{G}(\boldsymbol{\rho} - \boldsymbol{\rho}') = -\frac{i}{4}\mathbb{I}H_0(k_0|\boldsymbol{\rho} - \boldsymbol{\rho}'|) = -\frac{i}{4}\frac{1}{k_0^2}\sum_{m=-\infty}^{\infty}\Big[\nabla \times (\nabla' \times)^T\hat{z}(\hat{z}')^T$$

$$+ \frac{1}{k_0^2}\nabla \times \nabla \times (\nabla' \times)^T(\nabla' \times)^T\hat{z}(\hat{z}')^T + \nabla(\nabla')^T\Big]\psi_m^{(1)}(\rho_<, \varphi)\psi_m^{(4)*}(\rho_>, \varphi'). \tag{2.5}$$

The $1/k_0^2$ term outside the summation is introduced to keep the 2-D $\mathbb{G}(\boldsymbol{\rho} - \boldsymbol{\rho}')$ dimensionless as it should be, while the primed operators should be applied on the functions appearing in $\psi_m^{(1)}\psi_m^{(4)*}$, having the primed variables ρ', φ' in their

arguments. By rearranging terms and using the properties $(\mathbb{A}\mathbb{B}^T)^T = \mathbb{B}\mathbb{A}^T$—where $\mathbb{A}$, $\mathbb{B}$ are dyads—and $\mathbb{G}(\rho, \varphi; \rho', \varphi') = \mathbb{G}^{*T}(\rho, \varphi'; \rho', \varphi)$, we finally arrive at

$$
\mathbb{G}(\boldsymbol{\rho} - \boldsymbol{\rho}') = -\frac{i}{4}\frac{1}{k_0^2} \sum_{m=-\infty}^{\infty} \Big[\mathbf{M}_m^{(1)}(k_0, \rho_<, \varphi)\mathbf{M}_m^{(4)*T}(k_0, \rho_>, \varphi')
$$

$$
+ \mathbf{N}_m^{(1)}(k_0, \rho_<, \varphi)\mathbf{N}_m^{(4)*T}(k_0, \rho_>, \varphi') + \mathbf{L}_m^{(1)}(k_0, \rho_<, \varphi)\mathbf{L}_m^{(4)*T}(k_0, \rho_>, \varphi') \Big]. \quad (2.6)
$$

Eq. (2.6) is the desired 2-D tensorial GF. The superscripts (1), (4) in the CVWFs denote that J_m, H_m, respectively, should be used in Eq.(2.4). This tensorial form is a dyadic expansion of the scalar free space 2-D GF into divergenceless and irrotational CVWFs, and it is required to permit the analytical integration of the involved 2-D volumetric integrals of the CFVIEs (2.1).

2.4 Solution of the coupled field volume integral equations

2.4.1 Entire Domain Orthogonal Vectorial Basis Functions

The CFVIEs in (2.1) are rewritten by introducing the $\mathbf{D}(\boldsymbol{\rho})$ and $\mathbf{B}(\boldsymbol{\rho})$ fields, i.e.,

$$
\begin{bmatrix} \mathbf{E}(\boldsymbol{\rho}) \\ \mathbf{H}(\boldsymbol{\rho}) \end{bmatrix} = \begin{bmatrix} \mathbf{E}^{\text{inc}}(\boldsymbol{\rho}) \\ \mathbf{H}^{\text{inc}}(\boldsymbol{\rho}) \end{bmatrix} + \begin{bmatrix} \frac{1}{\epsilon_0}(k_0^2 + \nabla\nabla^T) & -\frac{ik_0}{\mu_0}\sqrt{\frac{\mu_0}{\epsilon_0}}\nabla\times \\ \frac{ik_0}{\epsilon_0}\sqrt{\frac{\epsilon_0}{\mu_0}}\nabla\times & \frac{1}{\mu_0}(k_0^2 + \nabla\nabla^T) \end{bmatrix} \int_{\boldsymbol{\rho}'\in S} \begin{bmatrix} \mathbb{G}(\boldsymbol{\rho}-\boldsymbol{\rho}')\mathbf{D}(\boldsymbol{\rho}') \\ \mathbb{G}(\boldsymbol{\rho}-\boldsymbol{\rho}')\mathbf{B}(\boldsymbol{\rho}') \end{bmatrix} \mathrm{d}\boldsymbol{\rho}'
$$

$$
- \begin{bmatrix} k_0^2 + \nabla\nabla^T & -ik_0\sqrt{\frac{\mu_0}{\epsilon_0}}\nabla\times \\ ik_0\sqrt{\frac{\epsilon_0}{\mu_0}}\nabla\times & k_0^2 + \nabla\nabla^T \end{bmatrix} \int_{\boldsymbol{\rho}'\in S} \begin{bmatrix} \mathbb{G}(\boldsymbol{\rho}-\boldsymbol{\rho}')\mathbf{E}(\boldsymbol{\rho}') \\ \mathbb{G}(\boldsymbol{\rho}-\boldsymbol{\rho}')\mathbf{H}(\boldsymbol{\rho}') \end{bmatrix} \mathrm{d}\boldsymbol{\rho}', \quad (2.7)
$$

where $\mathbf{D}(\boldsymbol{\rho}) = \boldsymbol{\epsilon}(\boldsymbol{\rho})\mathbf{E}(\boldsymbol{\rho})$ and $\mathbf{B}(\boldsymbol{\rho}) = \boldsymbol{\mu}(\boldsymbol{\rho})\mathbf{H}(\boldsymbol{\rho})$. The $\mathbf{E}(\boldsymbol{\rho})$ and $\mathbf{H}(\boldsymbol{\rho})$ fields are expanded in complete and orthogonal vectorial sets of divergenceless—$\mathbf{M}_{ml}(k_{ml}^M, \boldsymbol{\rho})$, $\mathbf{N}_{ml}(k_{ml}^N, \boldsymbol{\rho})$—and irrotational—$\mathbf{L}_{ml}(k_{ml}^L, \boldsymbol{\rho})$—Dini-type CVWFs, as

$$
\begin{bmatrix} \mathbf{E}(\boldsymbol{\rho}) \\ \mathbf{H}(\boldsymbol{\rho}) \end{bmatrix} = \sum_{m=-\infty}^{\infty} \sum_{l=1}^{\infty} \Big[\begin{matrix} \Gamma_{ml}\mathbf{M}_{ml}(\gamma_{ml}^M/a, \boldsymbol{\rho}) \\ \Sigma_{ml}\mathbf{M}_{ml}(\gamma_{ml}^M/a, \boldsymbol{\rho}) \end{matrix}
$$

$$
+ \begin{matrix} \Delta_{ml}\mathbf{N}_{ml}(\gamma_{ml}^N/a, \boldsymbol{\rho}) + Z_{ml}\mathbf{L}_{ml}(\gamma_{ml}^L/a, \boldsymbol{\rho}) \\ T_{ml}\mathbf{N}_{ml}(\gamma_{ml}^N/a, \boldsymbol{\rho}) + \Pi_{ml}\mathbf{L}_{ml}(\gamma_{ml}^L/a, \boldsymbol{\rho}) \end{matrix} \Big], \quad (2.8)
$$

with Γ_{ml}, Δ_{ml}, Z_{ml}, Σ_{ml}, T_{ml}, Π_{ml} unknown expansion coefficients. The Dini-type CVWFs in (2.8) are given by the same expressions as in (2.4), but with $Z_m = J_m$ and k_0 replaced by $\gamma_{ml}^{M,N,L}/a$. The sets γ_{ml}^M, γ_{ml}^N are selected to establish self-orthogonality of divergenceless CVWFs, i.e., $\langle \mathbf{M}_{ml}, \mathbf{M}_{\mu p} \rangle = M_{ml}\delta_{m\mu}\delta_{lp}$ and $\langle \mathbf{N}_{ml}, \mathbf{N}_{\mu p} \rangle = N_{ml}\delta_{m\mu}\delta_{lp}$—with δ Kronecker's delta—while, the set γ_{ml}^L is selected to decouple $\mathbf{M}_{ml}$ from $\mathbf{L}_{\mu p}$, i.e., $\langle \mathbf{M}_{ml}, \mathbf{L}_{\mu p} \rangle = 0$, since in general $\langle \mathbf{M}_{ml}, \mathbf{L}_{\mu p} \rangle \neq 0$. In particular, $\gamma_{ml}^{M,N,L}$ are roots of specific eigen-equations, the development of which is presented in detail in Appendix 1. The $\mathbf{D}(\boldsymbol{\rho})$ and $\mathbf{B}(\boldsymbol{\rho})$ fields satisfy $\nabla^T\mathbf{D}(\boldsymbol{\rho}) = 0$—no impressed volumetric charge is applied within the cylinder—and $\nabla^T\mathbf{B}(\boldsymbol{\rho}) = 0$. Therefore, the irrotational vector $\mathbf{L}_{ml}$ is not included in the expansion of $\mathbf{D}(\boldsymbol{\rho})$, $\mathbf{B}(\boldsymbol{\rho})$, with the latter being

$$
\begin{bmatrix} \frac{1}{\epsilon_0}\mathbf{D}(\boldsymbol{\rho}) \\ \frac{1}{\mu_0}\mathbf{B}(\boldsymbol{\rho}) \end{bmatrix} = \sum_{m=-\infty}^{\infty} \sum_{l=1}^{\infty} \begin{bmatrix} A_{ml}\mathbf{M}_{ml}(\gamma_{ml}^M/a, \boldsymbol{\rho}) + B_{ml}\mathbf{N}_{ml}(\gamma_{ml}^N/a, \boldsymbol{\rho}) \\ K_{ml}\mathbf{M}_{ml}(\gamma_{ml}^M/a, \boldsymbol{\rho}) + \Lambda_{ml}\mathbf{N}_{ml}(\gamma_{ml}^N/a, \boldsymbol{\rho}) \end{bmatrix}, \quad (2.9)
$$

where A_{ml}, B_{ml}, K_{ml}, Λ_{ml} unknown expansion coefficients.

2.4.2 Analytical Evaluation of the 2-D Volumetric Integrals

The 2-D volumetric integrals appeaing in (2.7) can be analytically evaluated via the entire domain orthogonal Dini-type CVWFs introduced in the previous Subsection. This will allow the analytical reduction of the CFVIEs to algebraic sets of equations. Observing the form of the fields expansions in (2.8), (2.9), and the form of the 2-D GF expansion in (2.6), the 2-D volumetric integrals $(\mathbb{G}\mathbf{M}_{ml})(\boldsymbol{\rho})$, $(\mathbb{G}\mathbf{N}_{ml})(\boldsymbol{\rho})$, $(\mathbb{G}\mathbf{L}_{ml})(\boldsymbol{\rho})$—where $(\mathbb{G}\mathbf{F})(\boldsymbol{\rho}) := \int_{\boldsymbol{\rho}' \in S} \mathbb{G}(\boldsymbol{\rho} - \boldsymbol{\rho}')\mathbf{F}(\boldsymbol{\rho}')\mathrm{d}\boldsymbol{\rho}'$—must be carried out in (2.7). The results depend on whether $\boldsymbol{\rho} \in S$ or $\boldsymbol{\rho} \in S_0$. When $\boldsymbol{\rho} \in S$, after various integrations by terms and cumbersome analytical manipulations involving various properties of Bessel functions, we can analytically carry out the 2-D integrations and get the following convenient results:

$$(\mathbb{G}\mathbf{M}_{ml})(\boldsymbol{\rho})|_{\boldsymbol{\rho} \in S} = -\frac{i\pi}{2} \Bigg\{ \frac{a^2}{(k_0 a)^2 - (k_{ml}^M a)^2}$$

$$\times \Bigg\{ -\frac{2i}{\pi}\mathbf{M}_{ml}(k_{ml}^M, \boldsymbol{\rho}) + (k_{ml}^M a)^2 H_m(k_0 a) J_m(k_{ml}^M a)$$

$$\times \Bigg[-\frac{H_m'(k_0 a)}{(k_0 a)H_m(k_0 a)} + \frac{J_m'(k_{ml}^M a)}{(k_{ml}^M a)J_m(k_{ml}^M a)} \Bigg] \mathbf{M}_m^{(1)}(k_0, \boldsymbol{\rho}) \Bigg\}$$

$$-\frac{a^2}{(k_0 a)^2} im H_m(k_0 a) J_m(k_{ml}^M a)\mathbf{L}_m^{(1)}(k_0, \boldsymbol{\rho}) \Bigg\}, \qquad (2.10)$$

$$(\mathbb{G}\mathbf{N}_{ml})(\boldsymbol{\rho})|_{\boldsymbol{\rho} \in S} = -\frac{i\pi}{2} \frac{a^2}{(k_0 a)^2 - (k_{ml}^N a)^2}$$

$$\times \Bigg\{ -\frac{2i}{\pi}\mathbf{N}_{ml}(k_{ml}^N, \boldsymbol{\rho}) + \frac{k_{ml}^N a}{k_0 a} H_m(k_0 a) J_m(k_{ml}^N a)$$

$$\times \Bigg[-(k_0 a)\frac{H_m'(k_0 a)}{H_m(k_0 a)} + (k_{ml}^N a)\frac{J_m'(k_{ml}^N a)}{J_m(k_{ml}^N a)} \Bigg] \mathbf{N}_m^{(1)}(k_0, \boldsymbol{\rho}) \Bigg\}, \qquad (2.11)$$

$$(\mathbb{G}\mathbf{L}_{ml})(\boldsymbol{\rho})|_{\boldsymbol{\rho} \in S} = -\frac{i\pi}{2} \Bigg\{ \frac{a^2}{(k_0 a)^2 - (k_{ml}^L a)^2}$$

$$\times \Bigg\{ -\frac{2i}{\pi}\mathbf{L}_{ml}(k_{ml}^L, \boldsymbol{\rho}) + (k_{ml}^L a)^2 H_m(k_0 a) J_m(k_{ml}^L a)$$

$$\times \Bigg[-\frac{H_m'(k_0 a)}{(k_0 a)H_m(k_0 a)} + \frac{J_m'(k_{ml}^L a)}{(k_{ml}^L a)J_m(k_{ml}^L a)} \Bigg] \mathbf{L}_m^{(1)}(k_0, \boldsymbol{\rho}) \Bigg\}$$

$$+\frac{a^2}{(k_0 a)^2} im H_m(k_0 a) J_m(k_{ml}^L a)\mathbf{M}_m^{(1)}(k_0, \boldsymbol{\rho}) \Bigg\}. \qquad (2.12)$$

In (2.10)–(2.12) the prime denotes differentiation with respect to the argument. These results will be used in the next Subsection for the analytical reduction of the CFVIEs to algebraic sets of equations.

2.4.3 Analytical Reduction of CFVIEs to Algebraic Equations

An incident plane wave, which impinges on the cylinder from negative values of x towards positive values of x, can be expanded in CVWFs as [78]

$$\mathbf{E}^{\mathrm{inc}}(\boldsymbol{\rho}) = \hat{y}e^{-ik_0 x}$$

$$= \sum_{m=-\infty}^{\infty} \Big[A_m^{\mathrm{inc}}\mathbf{M}_m^{(1)}(k_0, \boldsymbol{\rho}) + B_m^{\mathrm{inc}}\mathbf{N}_m^{(1)}(k_0, \boldsymbol{\rho}) \Big], \qquad (2.13)$$

with $A_m^{\text{inc}} = (-i)^{m+1}/k_0$ and $B_m^{\text{inc}} = (-i)^m/k_0$. The $\mathbf{M}_m^{(1)}$-part of this expansion represents TE incidence—or H-wave polarization (i.e., $E_z = 0$)—and the $\mathbf{N}_m^{(1)}$-part represents TM incidence—or E-wave polarization (i.e., $H_z = 0$). The respective incident magnetic field is obtained from (2.13) by $\mathbf{H}^{\text{inc}}(\boldsymbol{\rho}) = i/(\omega\mu_0)\nabla \times \mathbf{E}^{\text{inc}}(\boldsymbol{\rho})$. To use (2.13) and the respective one for $\mathbf{H}^{\text{inc}}(\boldsymbol{\rho})$ in (2.7), we further expand them in Dini-type CVWFs by

$$\begin{bmatrix} \mathbf{E}^{\text{inc}}(\boldsymbol{\rho}) \\ \mathbf{H}^{\text{inc}}(\boldsymbol{\rho}) \end{bmatrix} = \sum_{m=-\infty}^{\infty} \sum_{l=1}^{\infty} \begin{bmatrix} A_m^{\text{inc}}T_{ml}^M\mathbf{M}_{ml}(k_{ml}^M, \boldsymbol{\rho}) & + & B_m^{\text{inc}}T_{ml}^N\mathbf{N}_{ml}(k_{ml}^N, \boldsymbol{\rho}) \\ i\sqrt{\frac{\epsilon_0}{\mu_0}}B_m^{\text{inc}}T_{ml}^M\mathbf{M}_{ml}(k_{ml}^M, \boldsymbol{\rho}) & + & i\sqrt{\frac{\epsilon_0}{\mu_0}}A_m^{\text{inc}}T_{ml}^N\mathbf{N}_{ml}(k_{ml}^N, \boldsymbol{\rho}) \end{bmatrix},$$
(2.14)

with T_{ml}^M, T_{ml}^N given by

$$T_{ml}^M = \frac{\langle \mathbf{M}_m(k_0, \boldsymbol{\rho}), \mathbf{M}_{ml}(k_{ml}^M, \boldsymbol{\rho})\rangle}{\langle \mathbf{M}_{ml}(k_{ml}^M, \boldsymbol{\rho}), \mathbf{M}_{ml}(k_{ml}^M, \boldsymbol{\rho})\rangle},$$

$$T_{ml}^N = \frac{\langle \mathbf{N}_m(k_0, \boldsymbol{\rho}), \mathbf{N}_{ml}(k_{ml}^N, \boldsymbol{\rho})\rangle}{\langle \mathbf{N}_{ml}(k_{ml}^N, \boldsymbol{\rho}), \mathbf{N}_{ml}(k_{ml}^N, \boldsymbol{\rho})\rangle}.$$
(2.15)

The dot-products in the numerators of T_{ml}^M and T_{ml}^N are evaluated by (A.6) and (A.9), respectively, while the respective denominators by (A.8) and (A.11).

At this point it should be made clear that the differential operators $\nabla\nabla^T$, $\nabla\times$ in (2.7) remain always outside the integral sign and never apply on the integrand functions. That is to say, the development of the solution includes a two-step procedure: firstly perform the integrations analytically and secondly apply the differential operators. To implement the first step, we substitute (2.6), (2.8), (2.9) and (2.14) into (2.7), we carry out the 2-D integrations—this was already performed via (2.10)–(2.12)—and finally we use the Dini-type orthogonality relations (A.8), (A.11). This leads to four differential equations (DEs): two DEs involving $\{\Gamma_{ml}, A_m^{\text{inc}}, A_{ml}, \Lambda_{ml}, T_{ml}\}$ and $\{\Delta_{ml}, B_m^{\text{inc}}, B_{ml}, K_{ml}, \Sigma_{ml}\}$ from the first row of (2.7), and another two involving $\{\Sigma_{ml}, B_m^{\text{inc}}, K_{ml}, B_{ml}, \Delta_{ml}\}$ and $\{T_{ml}, A_m^{\text{inc}}, \Lambda_{ml}, A_{ml}, \Gamma_{ml}\}$ from the second row of (2.7).

To implement the second step, we apply the differential operators on the CVWFs and Dini-type CVWFs appearing in the aforementioned four DEs. To this end, we employ the properties $\nabla^T\mathbf{M}_m(k_0, \boldsymbol{\rho}) = \nabla^T\mathbf{N}_m(k_0, \boldsymbol{\rho}) = 0$ and $\nabla\nabla^T\mathbf{L}_m(k_0, \boldsymbol{\rho}) + k_0^2\mathbf{L}_m(k_0, \boldsymbol{\rho}) = 0$, as well as the properties $\nabla \times \mathbf{M}_m(k_0, \boldsymbol{\rho}) = k_0\mathbf{N}_m(k_0, \boldsymbol{\rho})$, $\nabla\times\mathbf{N}_m(k_0, \boldsymbol{\rho}) = k_0\mathbf{M}_m(k_0, \boldsymbol{\rho})$, $\nabla\times\mathbf{L}_m(k_0, \boldsymbol{\rho}) = 0$, and the respective ones satisfied by the Dini-type CVWFs. After laborious algebraic manipulations, we analytically arrive at four sets of infinite algebraic equations: the first two sets involve $\{\Gamma_{ml}, A_m^{\text{inc}}, A_{ml}, \Lambda_{ml}, T_{ml}\}$ and $\{\Delta_{ml}, B_m^{\text{inc}}, B_{ml}, K_{ml}, \Sigma_{ml}\}$. These are given by (2.16) and (2.17), respectively, shown at the top of next page. The remaining two algebraic sets involve $\{\Sigma_{ml}, B_m^{\text{inc}}, K_{ml}, B_{ml}, \Delta_{ml}\}$ and $\{T_{ml}, A_m^{\text{inc}}, \Lambda_{ml}, A_{ml}, \Gamma_{ml}\}$, and are also given by (2.16), (2.17), respectively, by substituting Γ_{ml}, A_m^{inc}, A_{ml}, Λ_{ml}, T_{ml} in (2.16) with Σ_{ml}, $i\sqrt{\epsilon_0/\mu_0}B_m^{\text{inc}}$, K_{ml}, Δ_{ml}, B_{ml}, and Δ_{ml}, B_m^{inc}, B_{ml}, Σ_{ml}, K_{ml} in (2.17) with T_{ml}, $i\sqrt{\epsilon_0/\mu_0}A_m^{\text{inc}}$, Λ_{ml}, A_{ml}, Γ_{ml}. It should be noted that the terms involving the irrotational vector $\mathbf{L}_{ml}$ cancel out after the application of the aforementioned differential properties, therefore the expansion coefficients Z_{ml}, Π_{ml} related to these vectors do not appear in the final algebraic equations.

Concluding, (2.16), (2.17) and their accompanied ones represent the algebraic reduction of the original CFVIEs (2.7). This analytical reduction constitutes the main advantage of our method since the specific Dini-type CVWFs allow the analytical integration of the 2-D volumetric integrals in (2.7).

$$\Gamma_{ml} = A_m^{\text{inc}} T_{ml}^M - \frac{(k_0 a)^2}{(k_0 a)^2 - (k_{ml}^M a)^2}(A_{ml} - \Gamma_{ml})$$

$$- \frac{i\pi}{2} T_{ml}^M \sum_{p=1}^{\infty}(A_{mp} - \Gamma_{mp})\frac{(k_0 a)^2 (k_{mp}^M a)^2}{(k_0 a)^2 - (k_{mp}^M a)^2} H_m(k_0 a) J_m(k_{mp}^M a)$$

$$\left[-\frac{H_m'(k_0 a)}{k_0 a H_m(k_0 a)} + \frac{J_m'(k_{mp}^M a)}{k_{mp}^M a J_m(k_{mp}^M a)} \right] + \sqrt{\frac{\mu_0}{\epsilon_0}} \sum_{p=1}^{\infty}(\Lambda_{mp} - T_{mp})$$

$$\frac{k_0 a k_{mp}^N a}{(k_0 a)^2 - (k_{mp}^N a)^2}\left\{ i\frac{\langle \mathbf{M}_{mp}(\gamma_{mp}^N/a, \boldsymbol{\rho}), \mathbf{M}_{ml}(\gamma_{ml}^M/a, \boldsymbol{\rho})\rangle}{\langle \mathbf{M}_{ml}(\gamma_{ml}^M/a, \boldsymbol{\rho}), \mathbf{M}_{ml}(\gamma_{ml}^M/a, \boldsymbol{\rho})\rangle} - \frac{\pi}{2}T_{ml}^M \right.$$

$$\left. \times H_m(k_0 a) J_m(k_{mp}^N a)\left[-k_0 a\frac{H_m'(k_0 a)}{H_m(k_0 a)} + k_{mp}^N a\frac{J_m'(k_{mp}^N a)}{J_m(k_{mp}^N a)} \right] \right\},$$

$$\text{(2.16)}$$

$$\Delta_{ml} = B_m^{\text{inc}} T_{ml}^N - \frac{(k_0 a)^2}{(k_0 a)^2 - (k_{ml}^N a)^2}(B_{ml} - \Delta_{ml})$$

$$- \frac{i\pi}{2} T_{ml}^N \sum_{p=1}^{\infty}(B_{mp} - \Delta_{mp})\frac{k_0 a k_{mp}^N a}{(k_0 a)^2 - (k_{mp}^N a)^2} H_m(k_0 a) J_m(k_{mp}^N a)$$

$$\left[-k_0 a\frac{H_m'(k_0 a)}{H_m(k_0 a)} + k_{mp}^N a\frac{J_m'(k_{mp}^N a)}{J_m(k_{mp}^N a)} \right] + \sqrt{\frac{\mu_0}{\epsilon_0}} \sum_{p=1}^{\infty}(K_{mp} - \Sigma_{mp})$$

$$\frac{k_0 a k_{mp}^M a}{(k_0 a)^2 - (k_{mp}^M a)^2}\left\{ i\frac{\langle \mathbf{N}_{mp}(\gamma_{mp}^M/a, \boldsymbol{\rho}), \mathbf{N}_{ml}(\gamma_{ml}^N/a, \boldsymbol{\rho})\rangle}{\langle \mathbf{N}_{ml}(\gamma_{ml}^N/a, \boldsymbol{\rho}), \mathbf{N}_{ml}(\gamma_{ml}^N/a, \boldsymbol{\rho})\rangle} - \frac{\pi}{2}T_{ml}^N k_0 a k_{mp}^M a \right.$$

$$\left. \times H_m(k_0 a) J_m(k_{mp}^M a)\left[-\frac{H_m'(k_0 a)}{k_0 a H_m(k_0 a)} + \frac{J_m'(k_{mp}^M a)}{k_{mp}^M a J_m(k_{mp}^M a)} \right] \right\}.$$

$$\text{(2.17)}$$

2.4.4 Constitutive Relations

The above four sets of infinite algebraic equations involve eight unknown expansion coefficients. Other four equations can be obtained by Galerkin technique from the constitutive relations $\mathbf{E}(\boldsymbol{\rho}) = \boldsymbol{\epsilon}^{-1}(\boldsymbol{\rho})\mathbf{D}(\boldsymbol{\rho})$ and $\mathbf{H}(\boldsymbol{\rho}) = \boldsymbol{\mu}^{-1}(\boldsymbol{\rho})\mathbf{B}(\boldsymbol{\rho})$. To employ these relations the inverse tensors $\boldsymbol{\epsilon}(\boldsymbol{\rho})^{-1}$, $\boldsymbol{\mu}(\boldsymbol{\rho})^{-1}$ must be transformed from cartesian to cylindrical coordinates. First, we readily express the inverse tensors in cartesian coordinates in terms of elements of (2.2) by

$$\boldsymbol{\zeta}^{-1}(\boldsymbol{\rho}) = \begin{bmatrix} \zeta_\perp(\boldsymbol{\rho}) & -i\zeta_x(\boldsymbol{\rho}) & 0 \\ i\zeta_x(\boldsymbol{\rho}) & \zeta_\perp(\boldsymbol{\rho}) & 0 \\ 0 & 0 & \zeta_\parallel(\boldsymbol{\rho}) \end{bmatrix},$$

$$\boldsymbol{\zeta}^{-1} = \boldsymbol{\epsilon}^{-1}, \boldsymbol{\mu}^{-1}, \quad \zeta_{\perp,x,\parallel} = \epsilon_{\perp,x,\parallel}, \mu_{\perp,x,\parallel}, \tag{2.18}$$

where $\epsilon_\perp(\mathbf{r}) = \epsilon_1(\boldsymbol{\rho})/[\epsilon_1^2(\boldsymbol{\rho}) - \epsilon_2^2(\boldsymbol{\rho})]$, $\epsilon_x(\boldsymbol{\rho}) = \epsilon_2(\boldsymbol{\rho})/[\epsilon_1^2(\boldsymbol{\rho}) - \epsilon_2^2(\boldsymbol{\rho})]$, $\epsilon_\parallel(\boldsymbol{\rho}) = 1/\epsilon_3(\boldsymbol{\rho})$, $\mu_\perp(\mathbf{r}) = \mu_1(\boldsymbol{\rho})/[\mu_1^2(\boldsymbol{\rho}) - \mu_2^2(\boldsymbol{\rho})]$, $\mu_x(\boldsymbol{\rho}) = \mu_2(\boldsymbol{\rho})/[\mu_1^2(\boldsymbol{\rho}) - \mu_2^2(\boldsymbol{\rho})]$ and $\mu_\parallel(\boldsymbol{\rho}) = 1/\mu_3(\boldsymbol{\rho})$. Then $\boldsymbol{\zeta}^{-1}(\boldsymbol{\rho})$ is transformed from cartesian to cylindrical coordinates by applying

the similarity transformation $\mathbb{Q}\boldsymbol{\zeta}^{-1}\mathbb{Q}^T$, with

$$\mathbb{Q} = \begin{bmatrix} \cos\varphi & \sin\varphi & 0 \\ -\sin\varphi & \cos\varphi & 0 \\ 0 & 0 & 1 \end{bmatrix}, \tag{2.19}$$

which yields $\mathbb{Q}\boldsymbol{\zeta}^{-1}\mathbb{Q}^T \equiv \boldsymbol{\zeta}^{-1}$. Therefore, $\boldsymbol{\zeta}^{-1}(\boldsymbol{\rho})$ in cylindrical coordinates is given by exactly the same expression as its cartesian counterpart in (2.16).

Substituting (2.8) in the left hand-side of $\mathbf{E}(\boldsymbol{\rho}) = \boldsymbol{\epsilon}^{-1}(\boldsymbol{\rho})\mathbf{D}(\boldsymbol{\rho})$ and $\mathbf{H}(\boldsymbol{\rho}) = \boldsymbol{\mu}^{-1}(\boldsymbol{\rho})\mathbf{B}(\boldsymbol{\rho})$, and (2.9) in the respective right hand-sides, and employing the Dini-type orthogonality relations (A.8), (A.11), we conclude to the following four sets of infinite linear equations, i.e.,

$$\Gamma_{ml}\langle\mathbf{M}_{ml},\mathbf{M}_{ml}\rangle = \epsilon_0 \sum_{p=1}^{\infty} A_{mp}\langle\boldsymbol{\epsilon}^{-1}\mathbf{M}_{mp},\mathbf{M}_{ml}\rangle,$$

$$\Delta_{ml}\langle\mathbf{N}_{ml},\mathbf{N}_{ml}\rangle = \epsilon_0 \sum_{p=1}^{\infty} B_{mp}\langle\boldsymbol{\epsilon}^{-1}\mathbf{N}_{mp},\mathbf{N}_{ml}\rangle,$$

$$\Sigma_{ml}\langle\mathbf{M}_{ml},\mathbf{M}_{ml}\rangle = \mu_0 \sum_{p=1}^{\infty} K_{mp}\langle\boldsymbol{\mu}^{-1}\mathbf{M}_{mp},\mathbf{M}_{ml}\rangle,$$

$$T_{ml}\langle\mathbf{N}_{ml},\mathbf{N}_{ml}\rangle = \mu_0 \sum_{p=1}^{\infty} \Lambda_{mp}\langle\boldsymbol{\mu}^{-1}\mathbf{N}_{mp},\mathbf{N}_{ml}\rangle. \tag{2.20}$$

The dot-products appearing in (2.20) are gathered in Appendix 2. The missing terms $B_{mp}\langle\boldsymbol{\epsilon}^{-1}\mathbf{N}_{mp},\mathbf{M}_{ml}\rangle$, $A_{mp}\langle\boldsymbol{\epsilon}^{-1}\mathbf{M}_{mp},\mathbf{N}_{ml}\rangle$, $\Lambda_{mp}\langle\boldsymbol{\mu}^{-1}\mathbf{N}_{mp},\mathbf{M}_{ml}\rangle$, $K_{mp}\langle\boldsymbol{\mu}^{-1}\mathbf{M}_{mp},\mathbf{N}_{ml}\rangle$ in (2.20) are zero due to the fact that $\mathbf{M}_{ml} \perp \mathbf{N}_{mp}$.

Although (2.16), (2.17) and their accompanied ones are set up analytically, (2.20) are set up numerically. However, in the case where the tensors' elements in (2.2) are independent of $\boldsymbol{\rho}$, the dot-products in (2.20) can be computed analytically. This results to a system of linear equations composed by exact formulas. In the general case where the anisotropy is inhomogeneous, these integrals are computed numerically using higher-order Gauss-Kronrod quadrature. Hence the CFVIE-CDSE method, in general, can be characterized as a hybrid—analytical-numerical—method.

In addition, (2.16), (2.17), their accompanied ones and (2.20) reveal that the first family of the expansion coefficients Γ_{ml}, A_{ml}, T_{ml}, Λ_{ml} is decoupled from the second family Δ_{ml}, B_{ml}, K_{ml}, Σ_{ml}. This proves the TE^z/TM^z mode separation in EM scattering on inhomogeneous gyrotropic cylinders by normally illuminated plane waves (the superscript z declares absence of E_z/H_z components, respectively—in the following this superscript is omitted). The first/second family corresponds to the TE/TM solution. In addition, the dot-products $\langle\boldsymbol{\epsilon}^{-1}\mathbf{M}_{mp},\mathbf{M}_{ml}\rangle$, $\langle\boldsymbol{\mu}^{-1}\mathbf{N}_{mp},\mathbf{N}_{ml}\rangle$ are involved in the TE solution and the $\langle\boldsymbol{\epsilon}^{-1}\mathbf{N}_{mp},\mathbf{N}_{ml}\rangle$, $\langle\boldsymbol{\mu}^{-1}\mathbf{M}_{mp},\mathbf{M}_{ml}\rangle$ in the TM solution. From the final form of these dot-products—as shown in Appendix 2 —it is concluded that the TE solution depends solely on ϵ_{1r}, ϵ_{2r}, μ_{3r} and the TM solution solely on μ_{1r}, μ_{2r}, ϵ_{3r}. In summary, (2.16), (2.17), their accompanied ones and (2.20) constitute sets of infinite linear simultaneous equations for the determination of the unknown expansion coefficients. After truncation, these sets lead to two separated linear systems, each one of which yields the TE/TM solution.

2.4.5 Scattered Fields

The scattered field $\mathbf{E}^{\text{sc}}(\boldsymbol{\rho})$ is obtained from (2.7) as $\mathbf{E}^{\text{sc}}(\boldsymbol{\rho}) = \mathbf{E}(\boldsymbol{\rho}) - \mathbf{E}^{\text{inc}}(\boldsymbol{\rho})$ for $\boldsymbol{\rho} \in S_0$. When $\boldsymbol{\rho} \in S_0$, analytical integrations in a similar manner as in (2.10)–(2.12), yield

$$(\mathbb{G}\mathbf{M}_{ml})(\boldsymbol{\rho})|_{\boldsymbol{\rho} \in S_0} = -\frac{i\pi a^2}{2(k_0 a)^2}$$

$$\times \left\{ -imJ_m(k_0 a)J_m(k_{ml}^M a)\mathbf{L}_m^{(4)}(k_0, \boldsymbol{\rho}) \right.$$

$$+ \left\{ k_0 a J_m'(k_0 a)J_m(k_{ml}^M a) + (k_0 a)^2[J_m(k_0 a)J_m'(k_{ml}^M a)k_{ml}^M a \right.$$

$$\left. - k_0 a J_m'(k_0 a)J_m(k_{ml}^M a)]/[(k_{ml}^M a)^2 - (k_0 a)^2] \right\}$$

$$\left. \times \mathbf{M}_m^{(4)}(k_0, \boldsymbol{\rho}) \right\}, \tag{2.21}$$

$$(\mathbb{G}\mathbf{N}_{ml})(\boldsymbol{\rho})|_{\boldsymbol{\rho} \in S_0} = -\frac{i\pi}{2}\frac{(k_{ml}^N a)^2}{k_0 a}\frac{a^2}{(k_{ml}^N a)^2 - (k_0 a^2)}$$

$$\times J_m(k_{ml}^N a)J_m(k_0 a)\left[(k_0 a)\frac{J_m'(k_0 a)}{J_m(k_0 a)} - (k_{ml}^N a)\frac{J_m'(k_{ml}^N a)}{J_m(k_{ml}^N a)}\right]$$

$$\times \mathbf{N}_m^{(4)}(k_0, \boldsymbol{\rho}), \tag{2.22}$$

$$(\mathbb{G}\mathbf{L}_{ml})(\boldsymbol{\rho})|_{\boldsymbol{\rho} \in S_0} = -\frac{i\pi a^2}{2(k_0 a)^2}$$

$$\times \left\{ imJ_m(k_0 a)J_m(k_{ml}^L a)\mathbf{M}_m^{(4)}(k_0, \boldsymbol{\rho}) \right.$$

$$+ \left\{ k_0 a J_m(k_{ml}^L a)J_m'(k_0 a) - (k_0 a)^2[k_0 a J_m(k_{ml}^L a)J_m'(k_0 a) \right.$$

$$\left. - k_{ml}^L a J_m'(k_{ml}^L a)J_m(k_0 a)]/[(k_0 a)^2 - (k_{ml}^L a)^2] \right\}$$

$$\left. \times \mathbf{L}_m^{(4)}(k_0, \boldsymbol{\rho}) \right\}. \tag{2.23}$$

Substituting (2.6), (2.8), (2.9) in (2.7), applying the aforementioned analytical 2-D integrations for $\boldsymbol{\rho} \in S_0$, and making analytical manipulations, the scattered electric field is expressed in the form $\mathbf{E}^{\text{sc}}(\boldsymbol{\rho}) = \sum_{m=-\infty}^{\infty}\sum_{l=1}^{\infty}[C_{ml}^M \mathbf{M}_m^{(4)}(k_0, \boldsymbol{\rho}) + C_{ml}^N \mathbf{N}_m^{(4)}(k_0, \boldsymbol{\rho})]$, with C_{ml}^M, C_{ml}^N given by

$$C_{ml}^M = (\Gamma_{ml} - A_{ml})\frac{i\pi}{2}\left\{ k_0 a J_m'(k_0 a)J_m(k_{ml}^M a) \right.$$

$$+ (k_0 a)^2\frac{J_m(k_{ml}^M a)J_m(k_0 a)}{(k_{ml}^M a)^2 - (k_0 a)^2}$$

$$\left. \times \left[-k_{ml}^M a\frac{J_m'(k_{ml}^M a)}{J_m(k_{ml}^M a)} + k_0 a\frac{J_m'(k_0 a)}{J_m(k_0 a)} \right] \right\}$$

$$- (\Lambda_{ml} - T_{ml})\frac{\pi}{2}\sqrt{\frac{\mu_0}{\epsilon_0}}\frac{k_{ml}^N a k_0 a}{(k_{ml}^N a)^2 - (k_0 a)^2}J_m(k_{ml}^N a)$$

$$\times J_m(k_0 a)\left[k_0 a\frac{J_m'(k_0 a)}{J_m(k_0 a)} - k_{ml}^N a\frac{J_m'(k_{ml}^N a)}{J_m(k_{ml}^N a)} \right], \tag{2.24}$$

$$C_{ml}^N = (\Delta_{ml} - B_{ml})\frac{i\pi}{2}\frac{k_{ml}^N a k_0 a}{(k_{ml}^N a)^2 - (k_0 a)^2} J_m(k_{ml}^N a) J_m(k_0 a)$$

$$\times \left[k_0 a \frac{J_m'(k_0 a)}{J_m(k_0 a)} - k_{ml}^N a \frac{J_m'(k_{ml}^N a)}{J_m(k_{ml}^N a)} \right]$$

$$- (K_{ml} - \Sigma_{ml})\frac{\pi}{2}\sqrt{\frac{\mu_0}{\epsilon_0}}\left\{ k_0 a J_m'(k_0 a) J_m(k_{ml}^M a) \right.$$

$$+ (k_0 a)^2 \frac{J_m(k_{ml}^M a) J_m(k_0 a)}{(k_{ml}^M a)^2 - (k_0 a)^2}$$

$$\left. \times \left[-k_{ml}^M a \frac{J_m'(k_{ml}^M a)}{J_m(k_{ml}^M a)} + k_0 a \frac{J_m'(k_0 a)}{J_m(k_0 a)} \right] \right\}. \tag{2.25}$$

Then, the scattered electric far-field and in sequence the normalized scattering cross section (or normalized scattering width) $\sigma(\varphi)/\lambda_0$—with λ_0 the free space wavelength—can be readily computed.

2.5   *Numerical Results*

Herein we demonstrate the validity and performance of the developed CFVIE-CDSE method, for electrically large and electrically small anisotropic/isotropic and homogeneous/inhomogeneous cylinders. To this end we perform comparisons with various alternative methods. Although the TE solution depends on ϵ_{1r}, ϵ_{2r}, μ_{3r} and the TM solution on μ_{1r}, μ_{2r}, ϵ_{3r}, in the following presentation we compactly declare the relative permittivity elements of (2.2) all together in a set notation as $\boldsymbol{\epsilon}_r = \{\epsilon_{1r}, \epsilon_{2r}, \epsilon_{3r}\}$, and similarly the permeability elements as $\boldsymbol{\mu}_r = \{\mu_{1r}, \mu_{2r}, \mu_{3r}\}$. In the previous notations, $\boldsymbol{\epsilon}_r$, $\boldsymbol{\mu}_r$ stand for the relative tensors.

In Figures 2.1(a)–(b) we compare the CFVIE-CDSE, for both TE/TM incidence, with the exact solution for isotropic cylinders [79], as obtained by SVM. Figure 2.1(a) depicts the normalized scattering cross section σ/λ_0 for an electrically large homogeneous cylinder consisting of a high refractive index isotropic dielectric using $k_0 a = 3\pi$—or equivalently $a/\lambda_0 = 1.5$. The values of the parameters used are gathered in Figure's caption. In addition, Figure 2.1(b) depicts σ/λ_0 for a core-shell set-up where the core is composed of a high refractive index dielectric coated by a shell with plasmonic properties. In this case both regions are still isotropic. This latter example is implemented for $k_0 a = 2\pi$ (i.e., the radius of the cylinder equals one free space wavelength). As is concluded from Figures 2.1(a)–(b), the agreement between CFVIE-CDSE/SVM is evident for both TE/TM incidence. Next we proceed to anisotropic cylinders and Figure 2.1(c) illustrates the validation for homogeneous uniaxial anisotropy in both permittivity/permeability for $k_0 a = 4\pi$—now radius a is twice the incident wavelength. For this case, the exact TE/TM solution via the SVM is available from [59]. Obviously the CFVIE-CDSE perfectly follows the exact solution. In addition, Figure 2.1(d) demonstrates the excellent agreement for a homogeneous gyroelectric/gyromagnetic cylinder, keeping $k_0 a = 4\pi$ as previously, with the exact solution given again by [59].

The HFSS commercial software is employed to establish validity for two- and three-layered configurations. In Figure 2.2(a) we examine σ/λ_0 for a three-layered set-up: the core ($0 \leqslant \rho \leqslant 0.6a$) is a high-index dielectric, the first layer ($0.6a < \rho \leqslant 0.8a$) has gyroelectric properties, and the second-outer layer ($0.8a < \rho \leqslant a$) is again characterized by gyroelectric properties different from those of the first layer. The agreement shown in Figure 2.2(a) is for $k_0 a = 0.6\pi$. This small value in
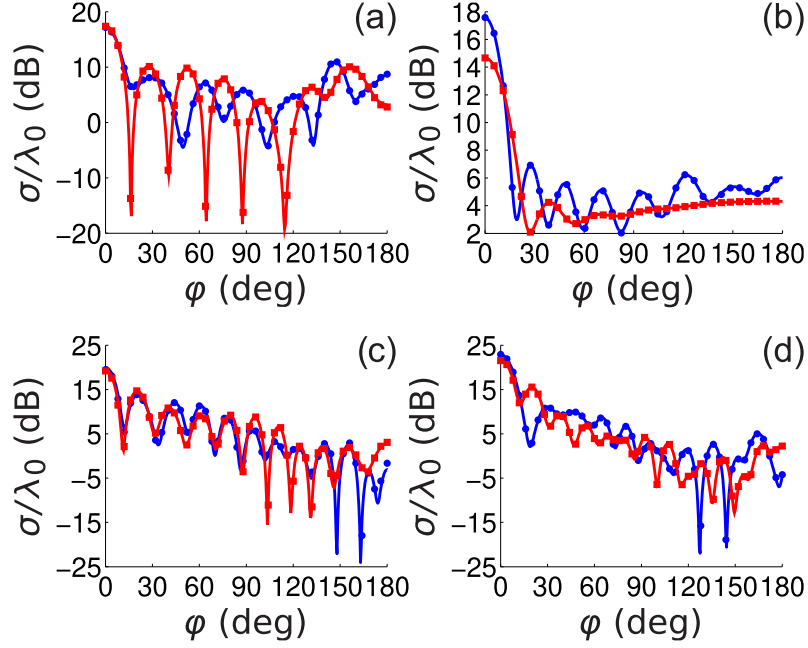
Figure 2.1 Normalized scattering cross section for various cylindrical set-ups. (a) High-index dielectric cylinder at $k_0 a = 3\pi$ with $\boldsymbol{\epsilon}_r = \{16, 0, 16\}$, $\boldsymbol{\mu}_r = \{1, 0, 1\}$. Blue: TE incidence; red: TM incidence; curves: CFVIE; dots/squares: SVM. (b) Core-shell dielectric-plasmonic cylinder at $k_0 a = 2\pi$. Core: high-index dielectric with $\boldsymbol{\epsilon}_r = \{16, 0, 16\}$, $\boldsymbol{\mu}_r = \{1, 0, 1\}$, $0 \leqslant \rho \leqslant 0.6a$; shell: plasmonic material with $\boldsymbol{\epsilon}_r = \{-2 - i0.1, 0, -2 - i0.1\}$, $\boldsymbol{\mu}_r = \{1, 0, 1\}$, $0.6a < \rho \leqslant a$. Blue: TE incidence; red: TM incidence; curves: CFVIE; dots/squares: SVM. (c) Uniaxial cylinder at $k_0 a = 4\pi$ with $\boldsymbol{\epsilon}_r = \{3, 0, 4\}$, $\boldsymbol{\mu}_r = \{2.25, 0, 3.5\}$. Blue: TE incidence; red: TM incidence; curves: CFVIE; dots/squares: SVM. (d) Gyrotropic cylinder at $k_0 a = 4\pi$ with $\boldsymbol{\epsilon}_r = \{3, 1, 1\}$, $\boldsymbol{\mu}_r = \{2.25, 0.5, 1\}$. Blue: TE incidence; red: TM incidence; curves: CFVIE; dots/squares: SVM.

electrical size—as compared to the above larger ones—is indicative of HFSS' limiting performance. To simulate an infinite cylinder in HFSS, a unit cell of sufficient height should be modeled—in our case this height is $16a$—in conjunction with master/slave boundary conditions to mimic the infinite length. In addition, the surface deviation in mesh definition should be small enough to capture the circular cross section of the cylinder—in our model the surface deviation was set to 10^{-3} cm when the radius is 1 cm and the operating frequency 8.99 GHz/these values are equivalent to $k_0 a = 0.6\pi$. On a Dell Precision 2.26 GHz double quad-core Xeon equipped machine, these constraints lead to 4800 s of CPU time and 17.4 GB of RAM in order HFSS to yield the result in Figure 2.2(a) for TE incidence, yet another 4800 s of CPU time to yield the result for TM incidence. On the contrary, CFVIE-CDSE converges in 35 s with 0.06 GB memory consumption, delivering both TE/TM solutions. In case one wants to enhance HFSS' accuracy, a smaller surface deviation of the order of 10^{-4} cm must be set, but this demands more than 48 GB of RAM, thus making the use of the commercial software unrealistic. In case $k_0 a$ is increased, the above computational performance deteriorates, and this is the reason why we have restricted $k_0 a$ to 0.6π. Figure 2.2(b) depicts the agreement between CFVIE-CDSE/HFSS for two
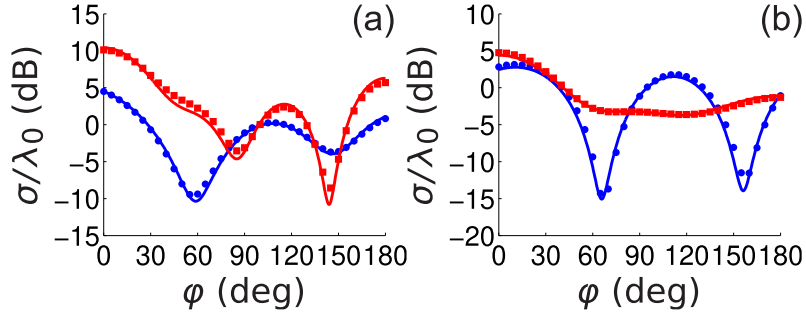
Figure 2.2   Normalized scattering cross section for anisotropic two- and three-layered set-ups. (a) Three-layered isotropic-gyroelectric-gyroelectric cylinder at $k_0 a = 0.6\pi$. Core: high-index dielectric with $\boldsymbol{\epsilon}_r = \{16, 0, 16\}$, $\boldsymbol{\mu}_r = \{1, 0, 1\}$, $0 \leqslant \rho \leqslant 0.6a$; first layer: gyroelectric material with $\boldsymbol{\epsilon}_r = \{3, 1, 4\}$, $\boldsymbol{\mu}_r = \{1, 0, 1\}$, $0.6a < \rho \leqslant 0.8a$; second-outer layer: gyroelectric material with $\boldsymbol{\epsilon}_r = \{5, 0.5, 6\}$, $\boldsymbol{\mu}_r = \{1, 0, 1\}$, $0.8a < \rho \leqslant a$. Blue: TE incidence; red: TM incidence; curves: CFVIE; dots/squares: HFSS. (b) Core-shell isotropic-gyroelectric cylinder and core-shell isotropic-gyromagnetic cylinder. Both set-ups are stimulated at $k_0 a = 0.6\pi$. Blue: TE incidence for a high-index dielectric core with $\boldsymbol{\epsilon}_r = \{16, 0, 16\}$, $\boldsymbol{\mu}_r = \{1, 0, 1\}$, $0 \leqslant \rho \leqslant 0.6a$ coated by a gyroelectric shell with $\boldsymbol{\epsilon}_r = \{3, 1, 4\}$, $\boldsymbol{\mu}_r = \{1, 0, 1\}$, $0.6a < \rho \leqslant a$. Curve: CFVIE; dots: HFSS. Red: TM incidence for a $0 \leqslant \rho \leqslant 0.6a$ hollow cylinder (i.e., free space) having a gyromagnetic shell with $\boldsymbol{\epsilon}_r = \{1, 0, 1\}$, $\boldsymbol{\mu}_r = \{3.5, 0.1, 5\}$, $0.6a < \rho \leqslant a$. Curve: CFVIE; squares: HFSS.

different two-layered scenarios, keeping $k_0 a = 0.6\pi$. In the first scenario—blue curve/dots in Figure 2.2(b)—the core is a high-index isotropic dielectric coated by a gyroelectric shell. In this case we examine the validity for TE incidence. In the second scenario—red curve/squares in Figure 2.2(b)—the core is hollow (i.e., free space) and the coating is gyromagnetic. This second example illustrates the validity for the TM incidence. The computational performance of HFSS for these two-layered scenarios is better than the above reported one for the three-layered set-up, i.e., 2640 s/12 GB RAM for the TE solution and 1500 s/7.1 GB RAM for the TM solution. This is mainly due to one less region with different constitutive parameters, which must be discretized by the finite element solver. CFVIE-CDSE performs at the same level—for both scenarios—as in the three-layered case.

     The main advantage of the CFVIE-CDSE is its capability to support continuously varying highly inhomogeneous gyrotropic profiles. Since an alternative technique to compare with CFVIE-CDSE for continuously varying tensorial elements is not available at our disposal, to demonstrate validity, we employ the recently developed HPM, capable of supporting continuously varying isotropic profiles. We calculate the EM scattering from an electrically large cylindrical Luneberg lens—$k_0 a = 20$ or $a/\lambda_0 = 3.18$—whose isotropic permittivity is given by $\boldsymbol{\epsilon}_r = \{\epsilon_r(\rho), 0, \epsilon_r(\rho)\}$, $\epsilon_r(\rho) = 2 - (\rho/a)^2$, $0 \leqslant \rho \leqslant a$, $\boldsymbol{\mu}_r = \{1, 0, 1\}$. The results are shown in Figures 2.3(a)–(b) for both TE/TM incidence. Due to the large scale of a vs λ_0, the response in σ/λ_0 has many variations vs observation angle φ. For such an electric size, the comparison between CFVIE-CDSE/HPM is excellent, while in particular the variations above $\varphi = 120°$ are well captured by both methods and for both polarizations. As far as CFVIE-CDSE is concerned, the converged results required 20 cylindrical harmonics and 20 Dini roots, whilst the order in Gauss-Kronrod quadra-
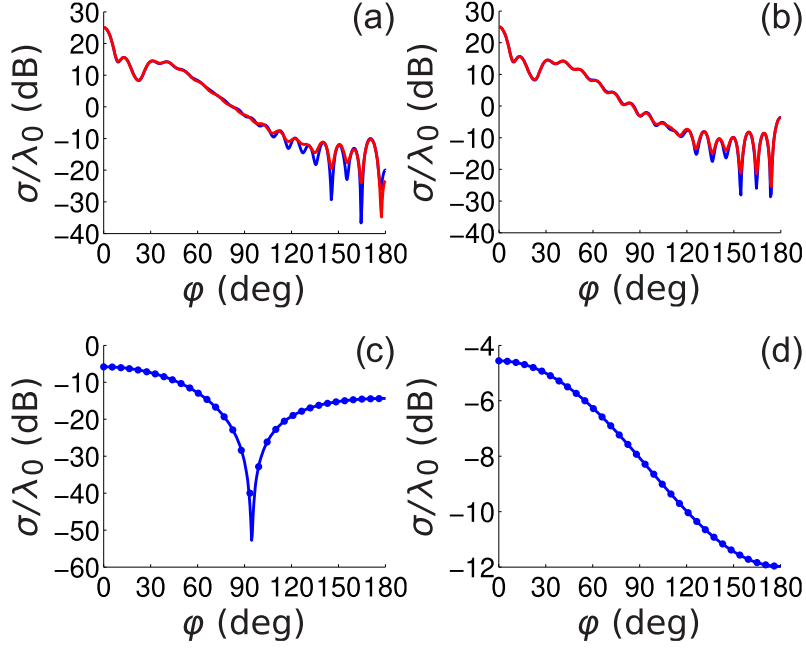
Figure 2.3   Normalized scattering cross section for Luneberg lens with $\epsilon_r = \{\epsilon_r(\rho), 0, \epsilon_r(\rho)\}$, $\epsilon_r(\rho) = 2 - (\rho/a)^2$, $\boldsymbol{\mu}_r = \{1, 0, 1\}$, $0 \leqslant \rho \leqslant a$. (a) $k_0 a = 20$, TE incidence; blue: CFVIE; red: HPM. (b) $k_0 a = 20$, TM incidence; blue: CFVIE; red: HPM. (c) $k_0 a = 1.4$, TE incidence; curve: CFVIE; dots: HPM. (d) $k_0 a = 1.4$, TM incidence; curve: CFVIE; dots: HPM.

ture was set to 64. This corresponds to a performance of 34 s in CPU time and 0.06 GB in RAM. To complement the above case with an electrically small problem, in Figures 2.3(c)–(d) we illustrate the agreement between CFVIE-CDSE/HPM for $k_0 a = 1.4$. The rest values of parameters are the same as in Figures 2.3(a)–(b). Respective details for CFVIE-CDSE's performance are 14 cylindrical harmonics, 14 Dini roots, same order in quadrature, 10 s in CPU time and the same memory consumption as previously.

Until this point verification is established on σ/λ_0, which involves the scattered far-field. In the following we show the validity of CFVIE-CDSE on near-fields. For this purpose we employ the exact SVM solution [59] for a homogeneous anisotropic cylinder having simultaneous gyroelectric/gyromagnetic properties $\epsilon_r = \{3, 1, 4\}$ and $\boldsymbol{\mu}_r = \{2.25, 0.5, 3.5\}$, and illustrate the comparison with CFVIE-CDSE. Figures 2.4(a)–(d) show the excellent agreement for TE incidence on xy-plane. In particular, Figures 2.4(a), (b) depict the normalized magnitude of the transversal and longitudinal components $|E_t|/\max\{|E_t|\}$—with $|E_t| = \sqrt{|E_\rho|^2 + |E_\varphi|^2}$— $|H_z|/\max\{|H_z|\}$, respectively, as obtained by CFVIE-CDSE. Then Figures 2.4(c), (d) show the respective results calculated by SVM. A similar comparison is performed for TM incidence in Figures 2.4(e)–(h) where now the normalized components $|H_t|/\max\{|H_t|\}$—with $|H_t| = \sqrt{|H_\rho|^2 + |H_\varphi|^2}$—and $|E_z|/\max\{|E_z|\}$ are present.

To demonstrate the advantage of the developed method, in Figure 2.5 we plot σ/λ_0 for a combined configuration consisting of a continuously varying highly
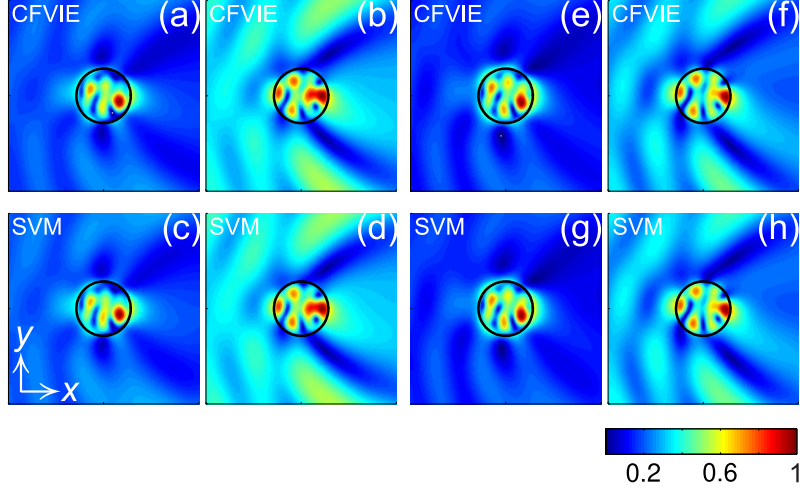
Figure 2.4   Near-fields on xy-plane for a homogeneous gyroelectric/gyromagnetic cylinder at $k_0a = 0.6\pi$ with $\boldsymbol{\epsilon}_r = \{3, 1, 4\}$, $\boldsymbol{\mu}_r = \{2.25, 0.5, 3.5\}$. (a)–(d): TE incidence. (a) $|E_t|/\max\{|E_t|\}$ by CFVIE. (b) $|H_z|/\max\{|H_z|\}$ by CFVIE. (c) $|E_t|/\max\{|E_t|\}$ by SVM. (d) $|H_z|/\max\{|H_z|\}$ by SVM. (e)–(h): TM incidence. (e) $|H_t|/\max\{|H_t|\}$ by CFVIE. (f) $|E_z|/\max\{|E_z|\}$ by CFVIE. (g) $|H_t|/\max\{|H_t|\}$ by SVM. (h) $|E_z|/\max\{|E_z|\}$ by SVM.
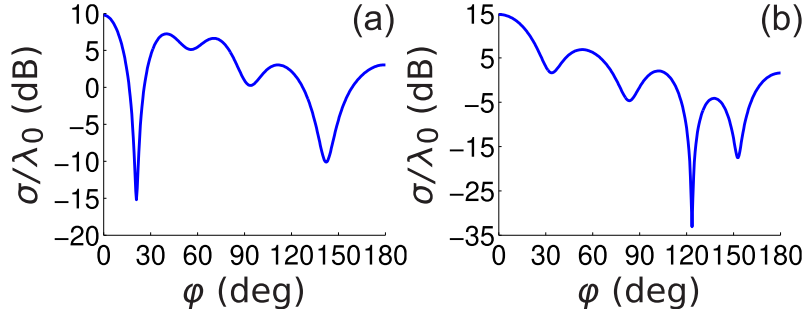
Figure 2.5   Normalized scattering cross section for fish-eyes lens shell coating a gyroelectric core at $k_0a = 2\pi$. Core: gyroelectric material with $\boldsymbol{\epsilon}_r = \{6, 0.2, 5\}$, $\boldsymbol{\mu}_r = \{1, 0, 1\}$, $0 \leqslant \rho \leqslant 0.7a$; shell: fish-eyes lens with $\boldsymbol{\epsilon}_r = \{\epsilon_r(\rho), 0, \epsilon_r(\rho)\}$, $\epsilon_r(\rho) = 4/[1 + (\rho/a)^2]^2$, $\boldsymbol{\mu}_r = \{1, 0, 1\}$, $0.7a < \rho \leqslant a$. (a) TE incidence; blue: CFVIE. (b) TM incidence; blue: CFVIE.

inhomogeneous shell coating a gyroelectric core. The shell is composed by a cylindrical fish-eyes lens with constitutive properties $\boldsymbol{\epsilon}_r = \{\epsilon_r(\rho), 0, \epsilon_r(\rho)\}$, $\epsilon_r(\rho) = 4/[1 + (\rho/a)^2]^2$, $\boldsymbol{\mu}_r = \{1, 0, 1\}$, $0.7a < \rho \leqslant a$, [80]. The gyroelectric core has $\boldsymbol{\epsilon}_r = \{6, 0.2, 5\}$, $\boldsymbol{\mu}_r = \{1, 0, 1\}$, $0 \leqslant \rho \leqslant 0.7a$ and the stimulation is set at $k_0a = 2\pi$. Since we cannot compare this combined set-up with another method, we have performed a self-consistent check where we have changed the parameters t_m^M, t_m^N from the ones discussed in Appendix 1, to other values and we have obtained exactly the same results for both TE/TM incidence, thus proving the reliability of the CFVIE-CDSE method.

2.6 Conclusion

We developed a CFVIE-CDSE method for the EM scattering by electrically large continuously varying highly inhomogeneous cylinders. The constitutive parameters can be of gyroelectric and gyromagnetic type. After construction of the appropriate 2-D tensorial GF, the CFVIEs were solved by utilizing an entire domain expansion of the fields in terms of orthogonal Dini-type CVWFs, whose orthogonal properties are constructed and presented for the first time in this work. The main advantage of our method is that it allows the analytical reduction of the involved 2-D volumetric integrals to sets of algebraic equations. The CFVIE-CDSE method validated vs SVM, HFSS and HPM for a variety of cases, including homogeneous/inhomogeneous profiles—by employing two and three layers as well as continuously varying highly inhomogeneous permittivity functions—in conjunction with isotropic and gyroelectric/gyromagnetic properties.

2.7 Appendix 1

The sets γ_{ml}^M, γ_{ml}^N, $m = -\infty, \ldots, \infty$, $l = 1, 2, \ldots, \infty$, appearing in (2.8), (2.9) are selected to establish self-orthogonality of the divergenceless CVWFs. In the following, we present in detail the procedure for constructing the self-orthogonality relation for $\mathbf{M}_{ml}$ vectors, i.e., $\langle \mathbf{M}_{ml}, \mathbf{M}_{\mu p} \rangle = M_{ml}\delta_{m\mu}\delta_{lp}$. The dot-product in this case is defined by

$$\langle \mathbf{M}_{ml}, \mathbf{M}_{\mu p} \rangle \equiv \int_{\boldsymbol{\rho} \in S} \mathbf{M}_{ml}^T \left(\frac{\gamma_{ml}^M}{a}, \boldsymbol{\rho}\right) \mathbf{M}_{\mu p}^* \left(\frac{\gamma_{\mu p}^M}{a}, \boldsymbol{\rho}\right) \mathrm{d}\boldsymbol{\rho}. \tag{A.1}$$

Substituting $\mathbf{M}_{ml}$, $\mathbf{M}_{\mu p}$ from (2.4), grouping terms and using the orthogonality relation for the exponential functions, we arrive at

$$\langle \mathbf{M}_{ml}, \mathbf{M}_{\mu p} \rangle = 2\pi \Big[\int_0^a \frac{m^2}{\rho} J_m\left(\frac{\gamma_{ml}^M}{a}\rho\right) J_m\left(\frac{\gamma_{mp}^M}{a}\rho\right) \mathrm{d}\rho$$

$$+ \int_0^a \rho \frac{\mathrm{d}J_m\left(\frac{\gamma_{ml}^M}{a}\rho\right)}{\mathrm{d}\rho} \frac{\mathrm{d}J_m\left(\frac{\gamma_{mp}^M}{a}\rho\right)}{\mathrm{d}\rho} \mathrm{d}\rho \Big] \delta_{m\mu}$$

$$\equiv 2\pi \Big(I_1 + I_2 \Big) \delta_{m\mu}. \tag{A.2}$$

Using the definitions $k_{ml}^M \equiv \gamma_{ml}^M/a$, $k_{mp}^M \equiv \gamma_{mp}^M/a$, integral I_2 in (A.2) can be further processed using integration by parts along with the relation $\mathrm{d}/(\mathrm{d}\rho)[\rho \mathrm{d}J_m(k_{ml}^M\rho)/(\mathrm{d}\rho)]$ $= [m^2/\rho - (k_{ml}^M)^2\rho]J_m(k_{ml}^M\rho)$ obtained from Bessel's differential equation. This leads to

$$I_2 = k_{ml}^M a \frac{\mathrm{d}J_m(k_{ml}^M a)}{\mathrm{d}(k_{ml}^M a)} J_m(k_{mp}^M a) - \int_0^a \frac{m^2}{\rho} J_m(k_{ml}^M\rho) J_m(k_{mp}^M\rho) \mathrm{d}\rho$$

$$+ \int_0^a J_m(k_{ml}^M\rho) J_m(k_{mp}^M\rho)(k_{ml}^M)^2 \rho \mathrm{d}\rho. \tag{A.3}$$

Substituting (A.3) back to (A.2), I_1 is eliminated, yielding

$$\langle \mathbf{M}_{ml}, \mathbf{M}_{\mu p}\rangle = 2\pi\Big[k_{ml}^M a J_m'(k_{ml}^M a)J_m(k_{mp}^M a)$$

$$+ (k_{ml}^M)^2 \int\limits_0^a J_m(k_{ml}^M\rho)J_m(k_{mp}^M\rho)\rho\mathrm{d}\rho\Big]\delta_{m\mu}. \tag{A.4}$$

The last integral in (A.4) is evaluated analytically using the same order-different argument property [81]

$$\int^\zeta Z_\mu(kz)W_\mu(\lambda z)z\mathrm{d}z = \frac{\zeta Z_\mu(k\zeta)W_\mu(\lambda\zeta)}{k^2 - \lambda^2}\Big[-k\frac{Z_\mu'(k\zeta)}{Z_\mu(k\zeta)} + \lambda\frac{W_\mu'(\lambda\zeta)}{W_\mu(\lambda\zeta)}\Big], \tag{A.5}$$

where Z_μ, W_μ can be Bessel, Neumann, or Hankel functions of order μ. Doing so, and after some algebra, (A.4) leads to

$$\langle \mathbf{M}_{ml}, \mathbf{M}_{\mu p}\rangle = 2\pi\frac{(\gamma_{ml}^M)^2(\gamma_{mp}^M)^2}{(\gamma_{ml}^M)^2 - (\gamma_{mp}^M)^2}J_m(\gamma_{m\ell}^M)J_m(\gamma_{mp}^M)$$

$$\times\Big\{-\frac{1}{\gamma_{ml}^M}\frac{J_m'(\gamma_{ml}^M)}{J_m(\gamma_{ml}^M)} + \frac{1}{\gamma_{mp}^M}\frac{J_m'(\gamma_{mp}^M)}{J_m(\gamma_{mp}^M)}\Big\}\delta_{m\mu}, \quad l \neq p. \tag{A.6}$$

From (A.6), if γ_{ml}^M are selected as the roots of the eigen-equation

$$\frac{1}{\gamma_{ml}^M}\frac{J_m'(\gamma_{ml}^M)}{J_m(\gamma_{ml}^M)} - t_m^M = 0, \quad t_m^M \in \mathbb{C},$$

$$m = -\infty,\ldots,\infty, \quad l = 1,2,\ldots,\infty, \tag{A.7}$$

then $\mathbf{M}_{ml}$ vectors constitute a fully orthogonal set, with orthogonality relation given by (A.4) with $l = p$. Using the well-known property $\int^\zeta Z_\mu^2(kz)z\mathrm{d}z = \zeta^2/2[Z_\mu^2(k\zeta) - Z_{\mu-1}(k\zeta)Z_{\mu+1}(k\zeta)]$ for the integral in (A.4), we finally get

$$\langle \mathbf{M}_{ml}, \mathbf{M}_{mp}\rangle = M_{ml}\delta_{m\mu}\delta_{lp} \equiv 2\pi\Big\{\gamma_{ml}^M J_m'(\gamma_{ml}^M)J_m(\gamma_{ml}^M) + \frac{(\gamma_{ml}^M)^2}{2}$$

$$\times\Big[J_m^2(\gamma_{ml}^M) - J_{m-1}(\gamma_{ml}^M)J_{m+1}(\gamma_{ml}^M)\Big]\Big\}\delta_{m\mu}\delta_{\ell p}. \tag{A.8}$$

Following a similar procedure for $\mathbf{N}_{ml}$ vectors we arrive at

$$\langle \mathbf{N}_{ml}, \mathbf{N}_{\mu p}\rangle \equiv \int_{\boldsymbol{\rho}\in S}\mathbf{N}_{ml}^T(\frac{\gamma_{ml}^N}{a},\boldsymbol{\rho})\mathbf{N}_{\mu p}^*(\frac{\gamma_{\mu p}^N}{a},\boldsymbol{\rho})\mathrm{d}\boldsymbol{\rho}$$

$$= 2\pi\frac{\gamma_{ml}^N\gamma_{mp}^N}{(\gamma_{ml}^N)^2 - (\gamma_{mp}^N)^2}J_m(\gamma_{m\ell}^N)J_m(\gamma_{mp}^N)$$

$$\times\Big\{-\gamma_{ml}^N\frac{J_m'(\gamma_{ml}^N)}{J_m(\gamma_{ml}^N)} + \gamma_{mp}^N\frac{J_m'(\gamma_{mp}^N)}{J_m(\gamma_{mp}^N)}\Big\}\delta_{m\mu}, \quad l \neq p. \tag{A.9}$$

Therefore, their orthogonality relation is established if γ_{ml}^N are selected as the roots of the eigen-equation

$$\gamma_{ml}^N\frac{J_m'(\gamma_{ml}^N)}{J_m(\gamma_{ml}^N)} - t_m^N = 0, \quad t_m^N \in \mathbb{C},$$

$$m = -\infty,\ldots,\infty, \quad l = 1,2,\ldots,\infty, \tag{A.10}$$

which finally yields

$$\langle \mathbf{N}_{ml}, \mathbf{N}_{\mu p} \rangle = N_{ml} \delta_{m\mu} \delta_{lp} \equiv \pi (\gamma_{ml}^N)^2 \left[J_m^2(\gamma_{ml}^N) \quad - J_{m-1}(\gamma_{ml}^N) J_{m+1}(\gamma_{ml}^N) \right] \delta_{m\mu} \delta_{lp}. \tag{A.11}$$

The parameters t_m^M, t_m^N appearing in (A.7), (A.10) may take arbitrary complex values. Each selection will lead to different sets γ_{ml}^M, γ_{ml}^N, but all of them will yield the same final solution. In this work we have used the values $t_{ml}^M = 1/5$ and $t_{ml}^N = -1/5$.

The remaining set γ_{ml}^L appearing in (2.8) is selected to decouple $\mathbf{M}_{ml}$ from $\mathbf{L}_{\mu p}$, i.e., $\langle \mathbf{M}_{ml}, \mathbf{L}_{\mu p} \rangle = 0$. Following a similar to the aforementioned procedure, we arrive at

$$\langle \mathbf{M}_{ml}, \mathbf{L}_{\mu p} \rangle \equiv \int_{\boldsymbol{\rho} \in S} \mathbf{M}_{ml}^T (\frac{\gamma_{ml}^M}{a}, \boldsymbol{\rho}) \mathbf{L}_{\mu p}^* (\frac{\gamma_{\mu p}^L}{a}, \boldsymbol{\rho}) \mathrm{d}\boldsymbol{\rho}$$

$$= -2\pi i m J_m(\gamma_{ml}^M) J_m(\gamma_{mp}^L) \equiv 0 \tag{A.12}$$

if γ_{ml}^L are selected as the roots of the eigen-equation

$$J_m(\gamma_{ml}^L) = 0,$$
$$m = -\infty, \ldots, \infty, \quad l = 1, 2, \ldots, \infty. \tag{A.13}$$

Finally, the relations $\langle \mathbf{M}_{ml}, \mathbf{N}_{\mu p} \rangle = 0$ and $\langle \mathbf{N}_{ml}, \mathbf{L}_{\mu p} \rangle = 0$ hold trivially, since the vectors in each dot-product are mutually orthogonal.

2.8   Appendix 2

The dot-products appearing in the first two equations of (2.20) are given by

$$\langle \boldsymbol{\epsilon}^{-1} \mathbf{M}_{mp}, \mathbf{M}_{ml} \rangle = \int_{\boldsymbol{\rho} \in S} \left[\boldsymbol{\epsilon}^{-1}(\boldsymbol{\rho}) \mathbf{M}_{mp} (\frac{\gamma_{mp}^M}{a}, \boldsymbol{\rho}) \right]^T \mathbf{M}_{ml}^* (\frac{\gamma_{ml}^M}{a}, \boldsymbol{\rho}) \mathrm{d}\boldsymbol{\rho} =$$

$$= m^2 \int_0^a \frac{1}{\rho} J_m(k_{mp}^M \rho) \epsilon_\perp(\rho) J_m(k_{ml}^M \rho) \mathrm{d}\rho - m \int_0^a \epsilon_x(\rho) \frac{\mathrm{d}J_m(k_{mp}^M \rho)}{\mathrm{d}\rho} J_m(k_{ml}^M \rho) \mathrm{d}\rho$$

$$- m \int_0^a \epsilon_x(\rho) \frac{\mathrm{d}J_m(k_{ml}^M \rho)}{\mathrm{d}\rho} J_m(k_{mp}^M \rho) \mathrm{d}\rho + \int_0^a \epsilon_\perp(\rho) \frac{\mathrm{d}J_m(k_{mp}^M \rho)}{\mathrm{d}\rho} \frac{\mathrm{d}J_m(k_{ml}^M \rho)}{\mathrm{d}\rho} \rho \mathrm{d}\rho, \tag{B.1}$$

$$\langle \boldsymbol{\epsilon}^{-1} \mathbf{N}_{mp}, \mathbf{N}_{ml} \rangle = \int_{\boldsymbol{\rho} \in S} \left[\boldsymbol{\epsilon}^{-1}(\boldsymbol{\rho}) \mathbf{N}_{mp} (\frac{\gamma_{mp}^N}{a}, \boldsymbol{\rho}) \right]^T \mathbf{N}_{ml}^* (\frac{\gamma_{ml}^N}{a}, \boldsymbol{\rho}) \mathrm{d}\boldsymbol{\rho} =$$

$$= k_{mp}^N k_{ml}^N \int_0^a \epsilon_\|(\rho) J_m(k_{mp}^N \rho) J_m(k_{ml}^N \rho) \rho \mathrm{d}\rho. \tag{B.2}$$

The dot-products $\langle \boldsymbol{\mu}^{-1} \mathbf{M}_{mp}, \mathbf{M}_{ml} \rangle$, $\langle \boldsymbol{\mu}^{-1} \mathbf{N}_{mp}, \mathbf{N}_{ml} \rangle$ appearing in the last two equations of (2.20) are given by (B.1), (B.2), respectively, by substituting $\epsilon_\perp(\rho)$, $\epsilon_x(\rho)$, $\epsilon_\|(\rho)$ with $\mu_\perp(\rho)$, $\mu_x(\rho)$ and $\mu_\|(\rho)$.

Calculation of Cutoff Wavenumbers for Multilayered Gyrotropic Circular Waveguides

A coupled-field volume integral equation (CFVIE) method is developed for the calculation of the normalized cutoff wavenumbers of circular metallic walled waveguides having concentric continuously varying highly inhomogeneous gyrotropic (i.e., gyroelectric and gyromagnetic) infill. The normalized cutoff wavenumbers are obtained as the roots of a determinantal equation formed by solving the CFVIEs using the cylindrical Dini series expansion (CDSE) method, where the unknown fields inside the waveguide are expanded by entire domain orthogonal Dini-type vectorial basis functions. To account for the electric boundary condition (BC) on waveguide's circular perfect electric conducting (PEC) surface, two modified two-dimensional (2-D) tensorial Green's functions (GFs), expanded in cylindrical vector wave functions (CVWFs), are employed in the kernels of the CFVIEs. These modified 2-D tensorial GFs are constructed by enforcing, on their dyadic form, the satisfaction of the electric boundary condition. The CDSE, along with the modified 2-D tensorial GFs, allow for the analytical integration of the volumentric-type integrals and the reduction of the CFVIEs to a set of algebraic equations. We exhaustively demonstrate the validity of the CFVIE-DSE by a series of comparisons on the normalized cutoff wavenumbers: we firstly construct the solutions for obtaining the normalized cutoff wavenumbers in homogeneous gyrotropic waveguides by the separation of variables method (SVM), and secondly we employ HFSS commercial software for two-layered isotropic and three-layered gyroelectric loaded waveguides. We characterize the type of modes, i.e., TE/TM or hybrid HE/EH, for each configuration presented, and discuss the efficiency of the CFVIE-DSE method.

3.1 Introduction

The calculation of the cutoff wavenumbers, or frequencies, in waveguiding structures, is particularly important for the design of various microwave elements including multifrequency transducers [82], dual-mode filters [83], circular waveguide-based multiplexers [84], or radial power dividers [85]. Other potential applications utilize the development of metamaterial-based guiding structures [86], which has led to the reduction of the cutoff frequency and a below-cutoff propagation in metamaterial-lined circular waveguides [87], to the miniaturization of circular waveguide probe antennas [88], or to the synthesization of horn antennas whose metamaterial inner wall can be seen as a waveguiding structure having an anisotropic surface impedance [89].

Modal analysis and cutoff characteristics in circular waveguiding configurations have been examined by different approaches. Concerning single homogeneous isotropic loaded waveguides, the characteristic equations and a generic modal analysis for cylindrical structures with anisotropic walls, where the inner surface is characterized by a pair of surface reactances or impedances, has been carried out by the SVM [89], [90] and by numerical simulations [91] while, arbitrary anisotropic surface impedance has been recently applied in [92] for the exploration of circular corrugated waveguides. Lately, a point-matching and a variational meshless method have been developed for arbitrarily shaped waveguides [93], [94], with [94] applied for the determination of propagating modes in circular shapes. Inhomogeneous isotropic structures, such as concentric step-index profiles, have also been studied by some approaches. The characteristic equations of a dielectric core coated by a metamaterial cladding have been resolved by the SVM [95] and applied for the demonstration of a below-cutoff propagation [87]. More recently, the variational meshless method has been applied for the evaluation of the dispersion diagram in isotropic double-layered shielded waveguides [96]. Apart from concentric core-cladding configurations, non-concentric structures consisting of circular isotropic infills have been considered by the point-matching [97], the least-squares boundary residual [98] and perturbation [99], [100] methods, as well as by the SVM in the bipolar coordinate system [101], [102].

Although the aforementioned contributions include a great variety of methods/applications concerning isotropic infills in circular waveguides, works on the use of anisotropic media have also been considered. In particular, uniaxial materials have been used for the formation of microstrip substrates [103]–[106], to study the accuracy of integrated-circuit modeling due to anisotropy [107], or in rectangular waveguides for effective-medium modeling [108] of metamaterial-based transmission [109]. In addition, other rectangular-based waveguide applications include the reconstruction of the constitutive parameters for materials having biaxial [110] or bianisotropic [111] properties. Aside from applications, rigorous modal analysis concerning anisotropic loadings has been presented for rectangular waveguides filled with a skew uniaxial dielectric [112], and latterly in [113] for various orientations of the optic axis of the crystal. Regarding circular structures, appropriate eigensolutions have been extracted for gyroelectric loaded waveguides [114]–[116], for waveguides composed of anisotropic conductivity material [117], and for anisotropic loaded core-cladding waveguides, where an isotropic core is coated by a uniaxial medium [118].

In this work we develop a CFVIE-CDSE method for the calculation of the normalized cutoff wavenumbers in circular PEC-walled waveguides, loaded with
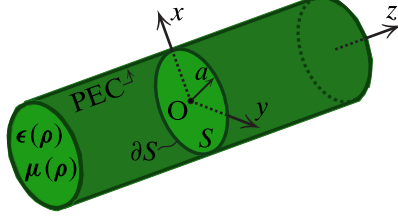
Figure 3.1   Schematic of the concentric multilayered gyrotropic circular waveguide.

concentric continuously varying highly inhomogeneous gyrotropic infill. The geometry of the configuration is shown in Figure 3.1, where S is waveguide's circular cross section having radius a, ∂S is its boundary, and z is the axis of the cylinder along which propagation takes place. The gyrotropic infill is described by concentric multilayered permittivity $\boldsymbol{\epsilon}(\boldsymbol{\rho})$ and permeability $\boldsymbol{\mu}(\boldsymbol{\rho})$ tensors given by

$$\boldsymbol{\zeta}(\boldsymbol{\rho}) = \begin{bmatrix} \zeta_1(\boldsymbol{\rho}) & i\zeta_2(\boldsymbol{\rho}) & 0 \\ -i\zeta_2(\boldsymbol{\rho}) & \zeta_1(\boldsymbol{\rho}) & 0 \\ 0 & 0 & \zeta_3(\boldsymbol{\rho}) \end{bmatrix}, \boldsymbol{\rho} \in S, \ \boldsymbol{\zeta} = \boldsymbol{\epsilon}, \boldsymbol{\mu}, \tag{3.1}$$

with $\zeta_j = \epsilon_j, \mu_j$, $j = 1, 2, 3$, and $\boldsymbol{\rho} = (\rho, \varphi)$ the position vector in the polar coordinate system. Each permittivity/permeability element in (3.1) is expressed as $\epsilon_j = \epsilon_{jr}\epsilon_0$ and $\mu_j = \mu_{jr}\mu_0$, $j = 1, 2, 3$, where ϵ_{jr}, μ_{jr} are the respective relative values and ϵ_0, μ_0 the free space permittivity and permeability, respectively. The specific gyrotropic form (3.1) is realized under external magnetic bias with direction parallel to cylinder's z axis. For off-angle directions of the biasing field, (3.1) are fully populated. In general, since the cutoff frequencies are the final quantities of interest in practical applications, then the configuration of Figure 3.1 has the following degrees of freedom (DoF): one DoF due to the radius a, $N - 1$ DoF due to the N layers, and one DoF due to the external biasing field, the magnitude of which actively affects the values of the tensors.

The proposed method of solution is based on a recently developed CFVIE method for the EM plane wave scattering by gyrotropic circular cylinders [119]. The solution in [119] was based on the expansion of the total electric $\mathbf{E}(\boldsymbol{\rho})$ and magnetic $\mathbf{H}(\boldsymbol{\rho})$ fields in entire domain orthogonal CVWFs of the Dini-type, i.e., $\mathbf{M}_{ml}(k_{ml}^M, \boldsymbol{\rho})$, $\mathbf{N}_{ml}(k_{ml}^N, \boldsymbol{\rho})$ and $\mathbf{L}_{ml}(k_{ml}^L, \boldsymbol{\rho})$, whose arguments k_{ml}^M, k_{ml}^N and k_{ml}^L have been selected to establish orthogonal and decoupling properties for the CVWFs, within the entire domain of the circular cross section. For the needs of the present work, i.e., the evaluation of the normalized cutoff wavenumbers, the CFVIEs are rewritten in absence of external excitation which, using the six-vector notation $[\mathbf{E}, \mathbf{H}]^T$—where T denotes transposition—are read

$$\begin{bmatrix} \mathbf{E}(\boldsymbol{\rho}) \\ \mathbf{H}(\boldsymbol{\rho}) \end{bmatrix} - \begin{bmatrix} k_0^2\mathbb{I} + \nabla\nabla^T & -ik_0\sqrt{\frac{\mu_0}{\epsilon_0}}\nabla\times \\ ik_0\sqrt{\frac{\epsilon_0}{\mu_0}}\nabla\times & k_0^2\mathbb{I} + \nabla\nabla^T \end{bmatrix}$$

$$\int_{\boldsymbol{\rho}'\in S} \begin{bmatrix} \mathbb{E}(\boldsymbol{\rho}, \boldsymbol{\rho}')\mathbb{X}_e(\boldsymbol{\rho}') & 0 \\ 0 & \mathbb{H}(\boldsymbol{\rho}, \boldsymbol{\rho}')\mathbb{X}_m(\boldsymbol{\rho}') \end{bmatrix} \begin{bmatrix} \mathbf{E}(\boldsymbol{\rho}') \\ \mathbf{H}(\boldsymbol{\rho}') \end{bmatrix} \mathrm{d}\boldsymbol{\rho}'$$

$$= 0, \quad \boldsymbol{\rho} \in S. \tag{3.2}$$

In (3.2), where the $\exp(i\omega t)$ time dependence has been adopted, $k_0 = \omega\sqrt{\epsilon_0\mu_0}$ is the free space wavenumber, $\mathbb{I}$ is the unity dyadic, $\mathbb{X}_e(\boldsymbol{\rho}) = \boldsymbol{\epsilon}(\boldsymbol{\rho})/\epsilon_0 - \mathbb{I}$ and

$\mathbb{X}_{\mathrm{m}}(\boldsymbol{\rho}) = \boldsymbol{\mu}(\boldsymbol{\rho})/\mu_0 - \mathbb{I}$ are the normalized tensorial electric and magnetic contrast functions and $\mathbb{E}(\boldsymbol{\rho}, \boldsymbol{\rho}')$, $\mathbb{H}(\boldsymbol{\rho}, \boldsymbol{\rho}')$ are modified 2-D tensorial GFs of the hollow waveguide. Based on the form (3.2) the present contribution has the following novel points:
(i) Construction of modified 2-D tensorial GFs $\mathbb{E}(\boldsymbol{\rho}, \boldsymbol{\rho}')$ and $\mathbb{H}(\boldsymbol{\rho}, \boldsymbol{\rho}')$, appearing in the two kernels of the electric-field VIE (EFVIE)—i.e., the VIE in the first row of (3.2)—so as to satisfy the electric BC at $\rho = a$. $\mathbb{H}(\boldsymbol{\rho}, \boldsymbol{\rho}')$ should exist in the kernel of the second integral term in the EFVIE—the one that features the $\nabla \times$ operator— as well as in the magnetic-field VIE (MFVIE)—i.e., the VIE in the second row of (3.2)—since the loading has, in addition, gyromagnetic properties. It should be noted that, as opposed to the CFVIEs (3.2), the CFVIEs in [119] employ, in both the EFVIE and MFVIE, the 2-D free space tensorial GF $\mathbb{G}(\boldsymbol{\rho}, \boldsymbol{\rho}') \equiv \mathbb{I}g(\boldsymbol{\rho}, \boldsymbol{\rho}')$, where $g(\boldsymbol{\rho}, \boldsymbol{\rho}') = -i/4 H_0^{(2)}(k_0|\boldsymbol{\rho} - \boldsymbol{\rho}'|)$—with $H_0^{(2)}$ the Hankel function of the second kind and zeroth order—is the 2-D free space GF [76].
(ii) The CVWF-based expansions of the $\mathbb{E}(\boldsymbol{\rho}, \boldsymbol{\rho}')$ and $\mathbb{H}(\boldsymbol{\rho}, \boldsymbol{\rho}')$, in conjunction with the expansions of $\mathbf{E}(\boldsymbol{\rho})$ and $\mathbf{H}(\boldsymbol{\rho})$ in Dini-type CVWFs, allow for the analytical evaluation of the volumetric-type integrals, giving rise to additional to the ones in [119] terms, due to the different GFs appearing in the kernels of the CFVIEs.
(iii) Analytical reduction of the CFVIEs (3.2) to algebraic sets of equations. These sets differ from the algebraic ones in [119], owing to the extra terms imposed through $\mathbb{E}(\boldsymbol{\rho}, \boldsymbol{\rho}')$ and $\mathbb{H}(\boldsymbol{\rho}, \boldsymbol{\rho}')$ for the satisfaction of the electric BC.
(iv) The CFVIE-CDSE method permits for the calculation of the normalized cutoff wavenumbers for continuously varying highly inhomogeneous gyroelectric and gyro-magnetic profiles, including dispersive materials. This is an effortless feature of the CDSE method, since the material properties are incorporated in the constitutive relations $\mathbf{E}(\boldsymbol{\rho}) = \boldsymbol{\epsilon}^{-1}(\boldsymbol{\rho})\mathbf{D}(\boldsymbol{\rho})$ and $\mathbf{H}(\boldsymbol{\rho}) = \boldsymbol{\mu}^{-1}(\boldsymbol{\rho})\mathbf{B}(\boldsymbol{\rho})$—where $\mathbf{D}(\boldsymbol{\rho})$ is the electric displacement and $\mathbf{B}(\boldsymbol{\rho})$ the magnetic flux density—and due to the fact that one part of the determinantal equation is formed by simple integration of the aforementioned constitutive relations, over the inhomogeneous anisotropic region of the cylinder.

We exhaustively demonstrate the validity of the CFVIE-CDSE, by construct-ing rigorous SVM solutions for homogeneously gyrotropic loaded waveguides, and compare the normalized cutoff wavenumbers. In addition, we perform HFSS com-mercial software simulations for two-layered isotropic and three-layered gyroelectric infills, and compare the resulting cutoff frequencies. For each configuration pre-sented, we assess the efficiency of the CFVIE-DSE versus HFSS and show that CFVIE proves much more efficient and accurate, as opposed to commercial's soft-ware time consuming finite element solver (FEM). Finally, we characterize the type of modes—i.e., TE/TM or hybrid HE/EH—maintained in such structures.

3.2 Modified two dimensional tensorial Green's function

The total $\mathbf{E}(\boldsymbol{\rho})$, as represented by the EFVIE (3.2), must satisfy $\hat{\rho} \times \mathbf{E}(\boldsymbol{\rho}) = 0$, $\boldsymbol{\rho} \in \partial S$. This requirement is met via the construction of two modified 2-D tenso-rial GFs $\mathbb{E}(\boldsymbol{\rho}, \boldsymbol{\rho}')$ and $\mathbb{H}(\boldsymbol{\rho}, \boldsymbol{\rho}')$ valid for the problem of the hollow waveguide, such that the original BC on $\mathbf{E}(\boldsymbol{\rho})$ is permuted to two BCs on the dyadic GFs (DGFs) of $\mathbb{E}(\boldsymbol{\rho}, \boldsymbol{\rho}')$ and $\mathbb{H}(\boldsymbol{\rho}, \boldsymbol{\rho}')$. The first BC reads $\hat{\rho} \times \mathbb{G}_e(\boldsymbol{\rho}, \boldsymbol{\rho}') = 0$, $\boldsymbol{\rho} \in \partial S$, where $\mathbb{G}_e(\boldsymbol{\rho}, \boldsymbol{\rho}') \equiv (\mathbb{I} + \nabla\nabla^T/k_0^2)\mathbb{E}(\boldsymbol{\rho}, \boldsymbol{\rho}')$ is the modified DGF of the electric type; the second BC reads $\hat{\rho} \times \widetilde{\mathbb{G}}_m(\boldsymbol{\rho}, \boldsymbol{\rho}') = 0$, $\boldsymbol{\rho} \in \partial S$, where $\widetilde{\mathbb{G}}_m(\boldsymbol{\rho}, \boldsymbol{\rho}') \equiv \nabla \times \mathbb{H}(\boldsymbol{\rho}, \boldsymbol{\rho}')$ is an additional modified DGF with $\widetilde{\mathbb{G}}_m(\boldsymbol{\rho}, \boldsymbol{\rho}') \neq \mathbb{G}_m(\boldsymbol{\rho}, \boldsymbol{\rho}') \equiv \nabla \times \mathbb{G}_e(\boldsymbol{\rho}, \boldsymbol{\rho}') = \nabla \times \mathbb{E}(\boldsymbol{\rho}, \boldsymbol{\rho}')$, where $\mathbb{G}_m(\boldsymbol{\rho}, \boldsymbol{\rho}')$ is the modified DGF of the magnetic type. The in-equation $\widetilde{\mathbb{G}}_m(\boldsymbol{\rho}, \boldsymbol{\rho}') \neq \mathbb{G}_m(\boldsymbol{\rho}, \boldsymbol{\rho}')$ stems from the fact that the electric BC must be

enforced. The aforementioned procedure concerning the use of modified tensorial GFs, was previously applied for three-dimensional problems in [120], [121] regarding the computation of eigenfrequencies in gyroelectric and in gyrotropic-metallic spherical cavities. Doubtlessly, the present case examines a waveguide problem and demands development from scratch.

To meet the aforesaid requirements, $\mathbb{E}(\boldsymbol{\rho}, \boldsymbol{\rho}')$ is written in the form $\mathbb{E}(\boldsymbol{\rho}, \boldsymbol{\rho}') = \mathbb{G}(\boldsymbol{\rho}, \boldsymbol{\rho}') + \mathbb{A}_e(\boldsymbol{\rho}, \boldsymbol{\rho}')$, where $\mathbb{G}(\boldsymbol{\rho}, \boldsymbol{\rho}')$ is the 2-D free space tensorial GF [119]—also referred to in the introduction—and $\mathbb{A}_e(\boldsymbol{\rho}, \boldsymbol{\rho}')$ is an auxiliary term that permits the satisfaction of $\hat{\rho} \times \mathbb{G}_e(\boldsymbol{\rho}, \boldsymbol{\rho}') = 0$, $\boldsymbol{\rho} \in \partial S$. If the electric dipole—the generating source for $\mathbb{G}_e(\boldsymbol{\rho}, \boldsymbol{\rho}')$—is located at $\boldsymbol{\rho}'$, then the BC at $\rho = a$ is satisfied in the region $\rho > \rho'$, therefore $\mathbb{A}_e(\boldsymbol{\rho}, \boldsymbol{\rho}')$ should be expressed by the tensorial expansion

$$\mathbb{A}_e(\boldsymbol{\rho}, \boldsymbol{\rho}') = \sum_{m=-\infty}^{\infty} \Big[P_m \mathbf{M}_m(k_0, \rho, \varphi) \mathbf{M}_m^{*T}(k_0, \rho', \varphi')$$
$$+ Q_m \mathbf{N}_m(k_0, \rho, \varphi) \mathbf{N}_m^{*T}(k_0, \rho', \varphi')$$
$$+ R_m \mathbf{L}_m(k_0, \rho, \varphi) \mathbf{L}_m^{*T}(k_0, \rho', \varphi') \Big], \tag{3.3}$$

with P_m, Q_m and R_m unknown expansion coefficients. In (3.3) the asterisk denotes complex conjugation and $\mathbf{M}_m$, $\mathbf{N}_m$, $\mathbf{L}_m$ are the CVWFs of the first kind which, under the cutoff condition $\beta = 0$ and thus $\partial/\partial z \to -i\beta = 0$—where β is the propagation constant—are given by [78]

$$\mathbf{M}_m(k_0, \boldsymbol{\rho}) = e^{-im\varphi} \Big[-i\frac{m}{\rho} J_m(k_0\rho)\hat{\rho} - \frac{\mathrm{d}J_m(k_0\rho)}{\mathrm{d}\rho}\hat{\varphi} \Big],$$
$$\mathbf{N}_m(k_0, \boldsymbol{\rho}) = e^{-im\varphi} k_0 J_m(k_0\rho)\hat{z},$$
$$\mathbf{L}_m(k_0, \boldsymbol{\rho}) = e^{-im\varphi} \Big[\frac{\mathrm{d}J_m(k_0\rho)}{\mathrm{d}\rho}\hat{\rho} - i\frac{m}{\rho} J_m(k_0\rho)\hat{\varphi} \Big], \tag{3.4}$$

with J_m the Bessel function. Applying, next, the BC $\hat{\rho} \times (\mathbb{I} + \nabla\nabla^T/k_0^2)[\mathbb{G}(\boldsymbol{\rho}, \boldsymbol{\rho}') + \mathbb{A}_e(\boldsymbol{\rho}, \boldsymbol{\rho}')] = 0$, $\rho = a$, utilizing the expansion (3.3) as well as the one for $\mathbb{G}(\boldsymbol{\rho}, \boldsymbol{\rho}')$ [119], and making use of the orthogonality relations of complex exponentials, we yield

$$P_m = \frac{i}{4}\frac{1}{k_0^2}\frac{H_m'(k_0 a)}{J_m'(k_0 a)} \equiv \frac{i}{4}\frac{1}{k_0^2} P_m',$$
$$Q_m = \frac{i}{4}\frac{1}{k_0^2}\frac{H_m(k_0 a)}{J_m(k_0 a)} \equiv \frac{i}{4}\frac{1}{k_0^2} Q_m', \tag{3.5}$$

where H_m is Hankel function of the second kind with the superscript (2) omitted and the prime denotes differentiation with respect to the argument. It should be noted that the expansion coefficient R_m is still undetermined, yet it will be defined in Section "Solution of the coupled fields volume integral equations" during the analytical evaluation of the volumetric-type integrals.

From the BC $\hat{\rho} \times \widetilde{\mathbb{G}}_m(\boldsymbol{\rho}, \boldsymbol{\rho}') = 0$, $\boldsymbol{\rho} \in \partial S$, and the definition $\widetilde{\mathbb{G}}_m(\boldsymbol{\rho}, \boldsymbol{\rho}') \equiv \nabla \times \mathbb{H}(\boldsymbol{\rho}, \boldsymbol{\rho}')$, it is concluded that $\mathbb{H}(\boldsymbol{\rho}, \boldsymbol{\rho}')$ should be expressed as $\mathbb{H}(\boldsymbol{\rho}, \boldsymbol{\rho}') = \mathbb{G}(\boldsymbol{\rho}, \boldsymbol{\rho}') + \mathbb{A}_m(\boldsymbol{\rho}, \boldsymbol{\rho}')$, where $\mathbb{A}_m(\boldsymbol{\rho}, \boldsymbol{\rho}')$ has the same expansion (3.3), but with P_m and Q_m swapped. This is the reason why $\widetilde{\mathbb{G}}_m(\boldsymbol{\rho}, \boldsymbol{\rho}') \neq \nabla \times \mathbb{E}(\boldsymbol{\rho}, \boldsymbol{\rho}')$ as stated above.

3.3   Solution of the coupled fields volume integral equations

The CFVIEs (3.2) define a homogeneous system $\mathbb{A}(x)\mathbf{v} = 0$ whose determinantal equation $\det\mathbb{A}(x) = 0$ will yield the normalized cutoff wavenumbers $x = k_0 a$. The system matrix $\mathbb{A}(x)$ is constructed in two steps: firstly, the CFVIEs are reduced, analytically to algebraic sets of equations; secondly, the constitutive relations $\mathbf{E}(\boldsymbol{\rho}) = \boldsymbol{\epsilon}^{-1}(\boldsymbol{\rho})\mathbf{D}(\boldsymbol{\rho})$ and $\mathbf{H}(\boldsymbol{\rho}) = \boldsymbol{\mu}^{-1}(\boldsymbol{\rho})\mathbf{B}(\boldsymbol{\rho})$ are employed to take into account the gyrotropic properties of the loading. To reduce the CFVIEs to their algebraic form, $\mathbf{E}(\boldsymbol{\rho})$ and $\mathbf{H}(\boldsymbol{\rho})$ are expanded in Dini-type CVWFs by

$$\mathbf{E}(\boldsymbol{\rho}) = \sum_{m=-\infty}^{\infty} \sum_{l=1}^{\infty} \Big[\Gamma_{ml}\mathbf{M}_{ml}(k_{ml}^M, \boldsymbol{\rho}) + \Delta_{ml}\mathbf{N}_{ml}(k_{ml}^N, \boldsymbol{\rho}) + Z_{ml}\mathbf{L}_{ml}(k_{ml}^L, \boldsymbol{\rho}) \Big],$$

$$\mathbf{H}(\boldsymbol{\rho}) = \sum_{m=-\infty}^{\infty} \sum_{l=1}^{\infty} \Big[\Sigma_{ml}\mathbf{M}_{ml}(k_{ml}^M, \boldsymbol{\rho}) + T_{ml}\mathbf{N}_{ml}(k_{ml}^N, \boldsymbol{\rho}) + \Pi_{ml}\mathbf{L}_{ml}(k_{ml}^L, \boldsymbol{\rho}) \Big], \quad (3.6)$$

where Γ_{ml}, Δ_{ml}, Z_{ml} and Σ_{ml}, T_{ml}, Π_{ml} are unknown expansion coefficients to be determined. The $\mathbf{D}(\boldsymbol{\rho})$ and $\mathbf{B}(\boldsymbol{\rho})$ fields—revealed in (3.2) by the relations $\mathbf{D}(\boldsymbol{\rho}) = \boldsymbol{\epsilon}(\boldsymbol{\rho})\mathbf{E}(\boldsymbol{\rho})$ and $\mathbf{B}(\boldsymbol{\rho}) = \boldsymbol{\mu}(\boldsymbol{\rho})\mathbf{H}(\boldsymbol{\rho})$ through the matrix-vector products $\mathbb{X}_{\mathrm{e}}(\boldsymbol{\rho})\mathbf{E}(\boldsymbol{\rho})$ and $\mathbb{X}_{\mathrm{m}}(\boldsymbol{\rho})\mathbf{H}(\boldsymbol{\rho})$—are expanded by

$$\mathbf{D}(\boldsymbol{\rho}) = \epsilon_0 \sum_{m=-\infty}^{\infty} \sum_{l=1}^{\infty} \Big[A_{ml}\mathbf{M}_{ml}(k_{ml}^M, \boldsymbol{\rho}) + B_{ml}\mathbf{N}_{ml}(k_{ml}^N, \boldsymbol{\rho}) \Big],$$

$$\mathbf{B}(\boldsymbol{\rho}) = \mu_0 \sum_{m=-\infty}^{\infty} \sum_{l=1}^{\infty} \Big[K_{ml}\mathbf{M}_{ml}(k_{ml}^M, \boldsymbol{\rho}) + \Lambda_{ml}\mathbf{N}_{ml}(k_{ml}^N, \boldsymbol{\rho}) \Big], \quad (3.7)$$

where A_{ml}, B_{ml} and K_{ml}, Λ_{ml} are unknown expansion coefficients to be determined. In (3.6)–(3.7), the Dini-type CVWFs are given by the same definitions (3.4) however, the arguments $k_{ml}^M \equiv \gamma_{ml}^M/a$ and $k_{ml}^N \equiv \gamma_{ml}^N/a$ are used to establish orthogonality of $\mathbf{M}_{ml}$ and $\mathbf{N}_{ml}$ vectors within domain S and are constructed using the formulas (A.7) and (A.10) in Appendix A of [119]. The argument $k_{ml}^L \equiv \gamma_{ml}^L/a$—given by (A.13) of the aforesaid Appendix—is selected to decouple $\mathbf{M}_{ml}$ and $\mathbf{L}_{ml}$ vectors so that their inner product is nil.

Substituting (3.6), (3.7) into (3.2), together with the expansions of $\mathbb{E}(\boldsymbol{\rho}, \boldsymbol{\rho}')$ and $\mathbb{H}(\boldsymbol{\rho}, \boldsymbol{\rho}')$, the volumetric-type integrals $(\mathbb{A}\mathbf{F})(\boldsymbol{\rho}) := \int_{\boldsymbol{\rho}' \in S} \mathbb{A}(\boldsymbol{\rho}, \boldsymbol{\rho}')\mathbf{F}(\boldsymbol{\rho}')\mathrm{d}\boldsymbol{\rho}'$, with $\mathbb{A} \equiv \mathbb{E}, \mathbb{H}$ and $\mathbf{F} \equiv \mathbf{M}_{ml}, \mathbf{N}_{ml}, \mathbf{L}_{ml}$, need to be evaluated. Employing various properties of Bessel functions, we carry out the 2-D integrations analytically which, after laborious manipulations, yield

$$(\mathbb{E}\mathbf{M}_{ml})(\boldsymbol{\rho})\big|_{\boldsymbol{\rho} \in S} = -\frac{i\pi a^2}{2x^2} \bigg\{ \frac{x^2}{x^2 - (k_{ml}^M a)^2}$$

$$\times \left\{ -\frac{2i}{\pi}\mathbf{M}_{ml}(k_{ml}^M, \boldsymbol{\rho}) + (k_{ml}^M a)^2 H_m(x) J_m(k_{ml}^M a) \right.$$

$$\times \left[-\frac{H_m'(x)}{x H_m(x)} + \frac{J_m'(k_{ml}^M a)}{k_{ml}^M a J_m(k_{ml}^M a)} \right] \mathbf{M}_m(k_0, \boldsymbol{\rho}) \right\}$$

$$- i m H_m(x) J_m(k_{ml}^M a) \mathbf{L}_m(k_0, \boldsymbol{\rho})$$

$$- P_m' \left\{ \frac{x^2}{x^2 - (k_{ml}^M a)^2} J_m(x) J_m(k_{ml}^M a) \right.$$

$$\times \left[-x\frac{J_m'(x)}{J_m(x)} + k_{ml}^M a \frac{J_m'(k_{ml}^M a)}{J_m(k_{ml}^M a)} \right]$$

$$+ x J_m'(x) J_m(k_{ml}^M a) \Big\} \mathbf{M}_m(k_0, \boldsymbol{\rho})$$

$$+ P_m' i m J_m(x) J_m(k_{ml}^M a) \mathbf{L}_m(k_0, \boldsymbol{\rho}) \bigg\}, \tag{3.8}$$

$$(\mathbb{E}\mathbf{N}_{ml})(\boldsymbol{\rho})|_{\boldsymbol{\rho} \in S} = -\frac{i\pi a^2}{2x} \frac{1}{x^2 - (k_{ml}^N a)^2}$$

$$\times \left\{ -\frac{2i}{\pi} x \mathbf{N}_{ml}(k_{ml}^N, \boldsymbol{\rho}) + k_{ml}^N a H_m(x) J_m(k_{ml}^N a) \right.$$

$$\times \left[-x\frac{H_m'(x)}{H_m(x)} + k_{ml}^N a \frac{J_m'(k_{ml}^N a)}{J_m(k_{ml}^N a)} \right] \mathbf{N}_m(k_0, \boldsymbol{\rho})$$

$$- Q_m' k_{ml}^N a \Big[-x J_m(k_{ml}^N a) J_m'(x)$$

$$+ k_{ml}^N a J_m(x) J_m'(k_{ml}^N a) \Big] \mathbf{N}_m(k_0, \boldsymbol{\rho}) \bigg\}, \tag{3.9}$$

$$(\mathbb{E}\mathbf{L}_{ml})(\boldsymbol{\rho})|_{\boldsymbol{\rho} \in S} = -\frac{i\pi a^2}{2x^2} \left\{ \frac{x^2}{x^2 - (k_{ml}^L a)^2} \right.$$

$$\times \left\{ -\frac{2i}{\pi}\mathbf{L}_{ml}(k_{ml}^L, \boldsymbol{\rho}) + (k_{ml}^L a)^2 H_m(x) J_m(k_{ml}^L a) \right.$$

$$\times \left[-\frac{H_m'(x)}{x H_m(x)} + \frac{J_m'(k_{ml}^L a)}{k_{ml}^L a J_m(k_{ml}^L a)} \right] \mathbf{L}_m(k_0, \boldsymbol{\rho}) \right\}$$

$$+ i m H_m(x) J_m(k_{ml}^L a) \mathbf{M}_m(k_0, \boldsymbol{\rho})$$

$$- P_m' \left\{ \frac{x^2}{x^2 - (k_{ml}^L a)^2} J_m(x) J_m(k_{ml}^L a) \right.$$

$$\times \left[-x\frac{J_m'(x)}{J_m(x)} + k_{ml}^L a \frac{J_m'(k_{ml}^L a)}{J_m(k_{ml}^L a)} \right]$$

$$+ x J_m'(x) J_m(k_{ml}^L a) \Big\} \mathbf{L}_m(k_0, \boldsymbol{\rho})$$

$$- P_m' i m J_m(x) J_m(k_{ml}^L a) \mathbf{M}_m(k_0, \boldsymbol{\rho}) \bigg\}. \tag{3.10}$$

In (3.8)–(3.10), the terms having P_m' and Q_m' as common factors were absent in the respective integrals $(\mathbb{G}\mathbf{F})(\boldsymbol{\rho})$, $\mathbf{F} \equiv \mathbf{M}_{ml}, \mathbf{N}_{ml}, \mathbf{L}_{ml}$, evaluated in [119], and contribute here due to the modified 2-D tensorial GFs. It should be stressed that the analytical evaluation of $(\mathbb{E}\mathbf{M}_{ml})(\boldsymbol{\rho})$ and $(\mathbb{E}\mathbf{L}_{ml})(\boldsymbol{\rho})$ is feasible only if the unknown so far expansion coefficient R_m in (3.3) attains the value $R_m \equiv P_m$. With this

choice, the determinantal equation obtained by the CFVIEs can be transformed to the two well-known characteristic equations for TE/TM modes—as given in Section 3.5—for a homogeneous isotropic loaded waveguide. Finally, the respective integrals $(\mathbb{H}\mathbf{F})(\boldsymbol{\rho})$, $\mathbf{F} \equiv \mathbf{M}_{ml}, \mathbf{N}_{ml}, \mathbf{L}_{ml}$, are again given by (3.8)–(3.10) with P'_m and Q'_m swapped.

Taking into account (3.8)–(3.10), as well as the accompanying integrals $(\mathbb{H}\mathbf{F})(\boldsymbol{\rho})$, $\mathbf{F} \equiv \mathbf{M}_{ml}, \mathbf{N}_{ml}, \mathbf{L}_{ml}$, applying the matrix differential operator existing outside the integral sign in (3.2), and making use of the orthogonality and decoupling properties of Dini-type CVWFs, the CFVIEs are reduced analytically to four sets of infinite algebraic equations. The first two sets are obtained by the EFVIE of (3.2) and are given by (3.11) and (3.12), shown at the top of next page. The other two sets are obtained by the MFVIE of (3.2) and are again given by (3.11) and (3.12) using the following substitutions: first, in (3.11) we apply $\Gamma_{ml} \to \Sigma_{ml}$, $A_{ml} \to K_{ml}$, $T_{ml} \to B_{ml}$, $\Lambda_{ml} \to \Delta_{ml}$ and $\sqrt{\mu_0/\epsilon_0} \to \sqrt{\epsilon_0/\mu_0}$; second, in (3.12) we apply $\Delta_{ml} \to T_{ml}$, $B_{ml} \to \Lambda_{ml}$, $K_{ml} \to \Gamma_{ml}$, $\Sigma_{ml} \to A_{ml}$ and $\sqrt{\mu_0/\epsilon_0} \to \sqrt{\epsilon_0/\mu_0}$. In (3.11), (3.12) the quantities T^M_{ml}, T^N_{ml} are given by [119, eq. (15)], while the dot products $\langle \mathbf{M}_{mp}(\gamma^N_{mp}/a, \boldsymbol{\rho}), \mathbf{M}_{ml}(\gamma^M_{ml}/a, \boldsymbol{\rho}) \rangle$ and $\langle \mathbf{M}_{ml}(\gamma^M_{ml}/a, \boldsymbol{\rho}), \mathbf{M}_{ml}(\gamma^M_{ml}/a, \boldsymbol{\rho}) \rangle$ in (3.11) are evaluated by [119, eqs. (A.6) and (A.8)], respectively, and $\langle \mathbf{N}_{mp}(\gamma^M_{mp}/a, \boldsymbol{\rho}), \mathbf{N}_{ml}(\gamma^N_{ml}/a, \boldsymbol{\rho}) \rangle$ and $\langle \mathbf{N}_{ml}(\gamma^N_{ml}/a, \boldsymbol{\rho}), \mathbf{N}_{ml}(\gamma^N_{ml}/a, \boldsymbol{\rho}) \rangle$ in (3.12) by [119, eqs. (A.9) and (A.11)], respectively. It should be mentioned that (3.11), (3.12) and the accompanying ones, feature the additional terms with P'_m and Q'_m as common factors. These terms were absent in the respective algebraic sets in [119]. Other four sets of infinite homogeneous equations are obtained by utilizing the constitutive relations $\mathbf{E}(\boldsymbol{\rho}) = \boldsymbol{\epsilon}^{-1}(\boldsymbol{\rho})\mathbf{D}(\boldsymbol{\rho})$ and $\mathbf{H}(\boldsymbol{\rho}) = \boldsymbol{\mu}^{-1}(\boldsymbol{\rho})\mathbf{B}(\boldsymbol{\rho})$, and integrating them over the inhomogeneous anisotropic region of the cylinder. These additional four sets are given by [119, eq. (20)]. For the case of an off-axis biasing magnetic field, or for a uniaxial infill with tilted optic axis, the tensors (3.1) change and lead to more complicated sets obtained from the above constitutive relations, as compared to the ones in [119]. For instance, for an off-axis bias, Γ_{ml} and Δ_{ml} do not only depend on A_{ml} and B_{ml}, respectively—as in [119, eq. (20)]—but they simultaneously depend on A_{ml} and B_{ml}. Similarly, Σ_{ml} and T_{ml} are coupled via K_{ml} and Λ_{ml}. This coupling leads to extra dot-product terms. Such a task constitutes a non trivial extension of the present method and is outside the scope of the present work.

From the above description of the eight sets of infinite homogeneous equations, four of them relate unknown expansion coefficients that multiply the $\mathbf{M}_{ml}$ vector appearing in the expansions of the $\mathbf{E}(\boldsymbol{\rho})$, $\mathbf{D}(\boldsymbol{\rho})$ fields in (3.6), (3.7), and the $\mathbf{N}_{ml}$ vector in the expansions of the $\mathbf{H}(\boldsymbol{\rho})$, $\mathbf{B}(\boldsymbol{\rho})$ fields. In addition, the other four sets relate unknown expansion coefficients that multiply the $\mathbf{N}_{ml}$ vector of the $\mathbf{E}(\boldsymbol{\rho})$, $\mathbf{D}(\boldsymbol{\rho})$ fields and the $\mathbf{M}_{ml}$ vector of the $\mathbf{H}(\boldsymbol{\rho})$, $\mathbf{B}(\boldsymbol{\rho})$ fields. These two families of sets constitute, after truncation, two homogeneous systems of the form $\mathbb{A}(x)\mathbf{v} = 0$. The determinantal equation $\det \mathbb{A}(x) = 0$ of each system matrix yields a sequence of the desired normalized cutoff wavenumbers $x_q = k_{0,q}a$, $k_{0,q} = \omega_q\sqrt{\epsilon_0\mu_0}$, $q = 1, 2, \ldots$. From (3.11), (3.12) it follows that $\mathbb{A}$ is constructed for every different value of m. The size of $\mathbb{A}$ is then $2L \times 2L$, where L is the maximum number of terms that indices l and p can acquire. In the case where the infill has only gyroelectric behavior with $\boldsymbol{\mu} = \mu_0\mathbb{I}$, the size of $\mathbb{A}$ is reduced to $L \times L$.

From the form the $\mathbf{M}_{ml}$, $\mathbf{N}_{ml}$ vectors have in (3.4), one may wrongly assume that a gyrotropic loaded waveguide allows for mode separation and that the first aforementioned family of the four sets yields the x for the TE^z modes ($E_z = 0, H_z \neq 0$), and the second family the x for the TM^z modes ($E_z \neq 0, H_z = 0$). This is not absolute since the type of mode depends on the type of anisotropy and whether the

$$\Gamma_{ml} = -\frac{x^2}{x^2 - (k_{ml}^M a)^2}(A_{ml} - \Gamma_{ml})$$
$$- \frac{i\pi}{2}T_{ml}^M \sum_{p=1}^{\infty}(A_{mp} - \Gamma_{mp})\bigg\{ \frac{x^2}{x^2 - (k_{mp}^M a)^2}\Big\{(k_{mp}^M a)^2 H_m(x)$$
$$\Big[-\frac{H_m'(x)}{xH_m(x)} + \frac{J_m'(k_{ml}^M a)}{k_{ml}^M a J_m(k_{ml}^M a)}\Big] - P_m' J_m(x)\Big[-x\frac{J_m'(x)}{J_m(x)} + k_{ml}^M a\frac{J_m'(k_{ml}^M a)}{J_m(k_{ml}^M a)}\Big]\Big\}$$
$$J_m(k_{mp}^M a) - P_m' x J_m'(x) J_m(k_{mp}^M a)\Big\} + \sqrt{\frac{\mu_0}{\epsilon_0}}\sum_{p=1}^{\infty}(\Lambda_{mp} - T_{mp})\frac{xk_{mp}^N a}{x^2 - (k_{mp}^N a)^2}$$
$$\Big\{ i\frac{\langle \mathbf{M}_{mp}(\gamma_{mp}^N/a, \boldsymbol{\rho}), \mathbf{M}_{ml}(\gamma_{ml}^M/a, \boldsymbol{\rho})\rangle}{\langle \mathbf{M}_{ml}(\gamma_{ml}^M/a, \boldsymbol{\rho}), \mathbf{M}_{ml}(\gamma_{ml}^M/a, \boldsymbol{\rho})\rangle} - \frac{\pi}{2}T_{ml}^M\Big\{H_m(x)J_m(k_{mp}^N a)$$
$$\Big[-x\frac{H_m'(x)}{H_m(x)} + k_{ml}^N a\frac{J_m'(k_{ml}^N a)}{J_m(k_{ml}^N a)}\Big] - Q_m'\Big[-xJ_m(k_{ml}^N a)J_m'(x)$$
$$+ k_{ml}^N a J_m(x) J_m'(k_{ml}^N a)\Big]\Big\}\Big\}, \tag{3.11}$$

$$\Delta_{ml} = -\frac{x^2}{x^2 - (k_{ml}^N a)^2}(B_{ml} - \Delta_{ml})$$
$$- \frac{i\pi}{2}T_{ml}^N \sum_{p=1}^{\infty}(B_{mp} - \Delta_{mp})\frac{xk_{mp}^N a}{x^2 - (k_{mp}^N a)^2}\Big\{H_m(x)J_m(k_{mp}^N a)$$
$$\Big[-x\frac{H_m'(x)}{H_m(x)} + k_{ml}^N a\frac{J_m'(k_{ml}^N a)}{J_m(k_{ml}^N a)}\Big] - Q_m'\Big[-xJ_m(k_{ml}^N a)J_m'(x)$$
$$+ k_{ml}^N a J_m(x) J_m'(k_{ml}^N a)\Big]\Big\} + \sqrt{\frac{\mu_0}{\epsilon_0}}\sum_{p=1}^{\infty}(K_{mp} - \Sigma_{mp})$$
$$\times \Big\{ i\frac{\langle \mathbf{N}_{mp}(\gamma_{mp}^M/a, \boldsymbol{\rho}), \mathbf{N}_{ml}(\gamma_{ml}^N/a, \boldsymbol{\rho})\rangle}{\langle \mathbf{N}_{ml}(\gamma_{ml}^N/a, \boldsymbol{\rho}), \mathbf{N}_{ml}(\gamma_{ml}^N/a, \boldsymbol{\rho})\rangle}\frac{xk_{mp}^M a}{x^2 - (k_{mp}^M a)^2} +$$
$$\frac{\pi}{2}T_{ml}^N\Big\{P_m' x J_m'(x) J_m(k_{ml}^M a) - \frac{x^2}{x^2 - (k_{mp}^M a)^2}$$
$$\times J_m(k_{mp}^M a)\Big\{(k_{mp}^M a)^2 H_m(x)\Big[-\frac{H_m'(x)}{xH_m(x)} + \frac{J_m'(k_{ml}^M a)}{k_{ml}^M a J_m(k_{ml}^M a)}\Big] - P_m' J_m(x)$$
$$\times \Big[-x\frac{J_m'(x)}{J_m(x)} + k_{ml}^M a\frac{J_m'(k_{ml}^M a)}{J_m(k_{ml}^M a)}\Big]\Big\}\Big\}\Big\}. \tag{3.12}$$

infill is homogeneous or inhomogeneous. This is elucidated in the following Section.

3.4   Modal Analysis and Designation

In this Section we use SVM and show that a homogeneous anisotropic loaded waveguide supports either $\mathrm{TE}^z/\mathrm{TM}^z$ or hybrid $\mathrm{HE}^z/\mathrm{EH}^z$ modes, depending on the type of anisotropy. To simplify the analysis, we assume only gyroelectric infill. In the

following, the superscript z in mode designation is omitted for simplicity.

Starting from $\nabla \times \mathbf{E}(\boldsymbol{\rho}) = -i\omega\mu_0 \mathbf{H}(\boldsymbol{\rho})$ and $\nabla \times \mathbf{H}(\boldsymbol{\rho}) = i\omega\boldsymbol{\epsilon}\mathbf{E}(\boldsymbol{\rho})$, it can be worked out that, for a homogeneous gyroelectric loaded waveguide, the H_z and E_z components satisfy the second order partial differential equations (PDEs)

$$\nabla_t^2 H_z + [(K^H)^2 - \beta^2]H_z = -\frac{\epsilon_{2r}}{\epsilon_{1r}}\beta\Big[-\frac{1}{\rho}\frac{\partial H_\rho}{\partial \varphi} + \frac{\partial H_\varphi}{\partial \rho} + \frac{1}{\rho}H_\varphi\Big],$$

$$\nabla_t^2 E_z + \Big[(K^E)^2 - \frac{\epsilon_{3r}}{\epsilon_{1r}}\beta^2\Big]E_z = -\frac{\epsilon_{2r}}{\epsilon_{1r}}\beta\Big[-\frac{1}{\rho}\frac{\partial E_\rho}{\partial \varphi} + \frac{\partial E_\varphi}{\partial \rho} + \frac{1}{\rho}E_\varphi\Big], \qquad (3.13)$$

where ∇_t^2 is the transverse Laplacian, $\partial/\partial z \to -i\beta$, and

$$(K^H)^2 \equiv \frac{\epsilon_{1r}^2 - \epsilon_{2r}^2}{\epsilon_{1r}}k_0^2, \quad (K^E)^2 \equiv \epsilon_{3r}k_0^2. \qquad (3.14)$$

Based on (3.13), we distinguish the following three cases.

1. Isotropic homogeneous case ($\epsilon_{1r} = \epsilon_{3r} \equiv \epsilon_r$, $\epsilon_{2r} = 0$): the PDEs (3.13) are reduced to two Helmholtz equations $\nabla_t^2\psi + k_c^2\psi = 0$, with $\psi \equiv H_z, E_z$ and $k_c^2 \equiv \epsilon_r k_0^2 - \beta^2$. The propagating modes are TE/TM [79]. At cutoff ($\beta = 0$), the characteristic equations are the well-known ones given by

$$J_m'(\sqrt{\epsilon_r}x) = 0 \text{ (for TE modes)},$$
$$J_m(\sqrt{\epsilon_r}x) = 0 \text{ (for TM modes)}. \qquad (3.15)$$

2. Uniaxial homogeneous case ($\epsilon_{1r} \neq \epsilon_{3r}$, $\epsilon_{2r} = 0$): the PDEs (3.13) are reduced to two Helmholtz equations $\nabla_t^2\psi + k_c^2\psi = 0$, with $(\psi, k_c^2) \equiv (H_z, (K^{\mathrm{TE}})^2 - \beta^2)$, $(K^{\mathrm{TE}})^2 \equiv \epsilon_{1r}k_0^2$ and $(\psi, k_c^2) \equiv (E_z, (K^{\mathrm{TM}})^2 - \beta^2)$, $(K^{\mathrm{TM}})^2 \equiv \epsilon_{3r}k_0^2$. In this case, the PDEs are decoupled and the solution is separated to TE/TM modes. At cutoff, it is straightforward to show that the characteristic equations are given by

$$J_m'(\sqrt{\epsilon_{1r}}x) = 0 \text{ (for TE modes)},$$
$$J_m(\sqrt{\epsilon_{3r}}x) = 0 \text{ (for TM modes)}. \qquad (3.16)$$

Obviously, (3.16) are identical to (3.15), with the only difference that the isotropic material wavenumber $\sqrt{\epsilon_r}k_0$ used in (3.15) is now replaced by K^{TE} and K^{TM} for TE and TM modes, respectively.

3. Gyroelectric homogeneous case ($\epsilon_{2r} \neq 0$): in this case the right hand-sides (RHSs) in (3.13) are not zero and the two PDEs are coupled. This can be understood from the fact that the transversal components $\psi = H_{\rho,\varphi}, E_{\rho,\varphi}$ in the RHSs of (3.13) can be written in the form $\psi = \psi^{H_z} + \psi^{E_z}$, where ψ^{H_z} is expressed only versus H_z, and ψ^{E_z} only versus E_z. Therefore, the H_z, E_z components cannot be separated and consequently the propagating modes are hybrid HE and EH.

At cutoff, however, it is possible to construct two characteristic equations that yield the cutoff x for the HE/EH modes. Following $\mathbf{E}(\boldsymbol{\rho}) = 1/(i\omega)\boldsymbol{\epsilon}^{-1}\nabla \times \mathbf{H}(\boldsymbol{\rho})$ and $\mathbf{H}(\boldsymbol{\rho}) = -1/(i\omega\mu_0)\nabla \times \mathbf{E}(\boldsymbol{\rho})$, the transversal components of the electromagnetic field inside the gyroelectric loaded waveguide are given by

$$E_\rho = \frac{1}{i\omega\epsilon_0}\Big[\frac{\epsilon_{1r}}{\epsilon_{1r}^2 - \epsilon_{2r}^2}\frac{1}{\rho}\frac{\partial H_z}{\partial \varphi} + i\frac{\epsilon_{2r}}{\epsilon_{1r}^2 - \epsilon_{2r}^2}\frac{\partial H_z}{\partial \rho}\Big],$$

$$E_\varphi = \frac{1}{i\omega\epsilon_0}\Big[i\frac{\epsilon_{2r}}{\epsilon_{1r}^2 - \epsilon_{2r}^2}\frac{1}{\rho}\frac{\partial H_z}{\partial \varphi} - \frac{\epsilon_{1r}}{\epsilon_{1r}^2 - \epsilon_{2r}^2}\frac{\partial H_z}{\partial \rho}\Big],$$

$$H_\rho = -\frac{1}{i\omega\mu_0}\frac{1}{\rho}\frac{\partial E_z}{\partial \varphi},$$

$$H_\varphi = \frac{1}{i\omega\mu_0}\frac{\partial E_z}{\partial \rho}. \qquad (3.17)$$

It should be stressed that (3.17) are valid at cutoff and that the phenomenal TE/TM separation—since $E_{\rho,\varphi}$ depend only on H_z and $H_{\rho,\varphi}$ only on E_z—does not hold. To clarify this point, when $\beta \neq 0$—i.e., at propagation—(3.17) are much more complicated and $E_{\rho,\varphi}$, $H_{\rho,\varphi}$ depend simultaneously on H_z and E_z; in addition, since the longitudinal components are coupled through the aforesaid DEs, the modes are hybrid. The same is true even for the special case $m = 0$, which is equivalent to $\partial/\partial\varphi \to 0$. The expressions (3.17) are simply the modal components of HE/EH modes right on cutoff. When $\beta = 0$, the RHSs in (3.13) equal to zero and the solutions of the resulting Helmholtz equations are

$$H_z = \sum_{m=-\infty}^{\infty} A_m J_m(K^H \rho) e^{-im\varphi} \text{ (for HE modes)},$$

$$E_z = \sum_{m=-\infty}^{\infty} B_m J_m(K^E \rho) e^{-im\varphi} \text{ (for EH modes).} \tag{3.18}$$

Satisfying, next, the boundary conditions $E_\varphi = 0$—through (3.17) and (3.18)—and $E_z = 0$—directly via (3.18)—at $\rho = a$, we get the following two characteristic equations that yield the cutoff x for the HE/EH modes, i.e.,

$$m\frac{\epsilon_{2r}}{\epsilon_{1r}^2 - \epsilon_{2r}^2} J_m\big(\sqrt{(\epsilon_{1r}^2 - \epsilon_{2r}^2)/\epsilon_{1r}}x\big) - \sqrt{\frac{\epsilon_{1r}}{\epsilon_{1r}^2 - \epsilon_{2r}^2}}x$$

$$\times J_m'\big(\sqrt{(\epsilon_{1r}^2 - \epsilon_{2r}^2)/\epsilon_{1r}}x\big) = 0 \text{ (for HE modes)},$$

$$J_m(\sqrt{\epsilon_{3r}}x) = 0 \text{ (for EH modes).} \tag{3.19}$$

Our remark that the cutoff x obtained from (3.19) correspond to HE/EH and not to TE/TM modes, is in line with the analysis for two-layered dielectric waveguides [87], where HE/EH modes are maintained. In particular, in [87, p. 3171], the cutoff condition $\gamma = 0$ was discussed and resulted to two uncoupled characteristic equations (7b) and (7c), that determine the cutoff frequencies of the HE and EH modes, respectively. In the general case where the infill is gyrotropic, the characteristic equations at cutoff for HE/EH modes are the same with (3.19), with the only difference that x in the first of (3.19) should be substituted by $\sqrt{\mu_{3r}}x$, and in the second of (3.19) by $\sqrt{(\mu_{1r}^2 - \mu_{2r}^2)/\mu_{1r}}x$.

From (3.16) and (3.19) it is deduced that, precisely at cutoff, the x are the same for TM and EH modes when uniaxial and gyroelectric infills are used, respectively, in the waveguide. However, above cutoff, the dispersion curves $\beta = \beta(\omega)$ for the TM/EH propagating modes differ. On the contrary, the cutoff x for the respective TE/HE modes, are different.

The above analysis is valid for homogeneous gyroelectric loaded waveguides. When the infill is multilayered, even for the two-layered isotropic configuration, the propagating modes are HE/EH [87], except for the case $m = 0$, where the modes are TE/TM; physically, the existence of the hybrid modes is due to the interface between the two dielectric layers. Therefore, for multilayered isotropic/uniaxial infills, the modes are hybrid, except for the case $m = 0$. The multilayered gyrotropic infills lead only to hybrid modes.

Concluding, the four out of eight sets of infinite homogeneous equations defined in Section "Solution of the Coupled Field Volume Integral Equation" and relate unknown expansion coefficients that multiply the $\mathbf{M}_{ml}$ vector of the $\mathbf{E}(\boldsymbol{\rho})$, $\mathbf{D}(\boldsymbol{\rho})$ fields and the $\mathbf{N}_{ml}$ vector of the $\mathbf{H}(\boldsymbol{\rho})$, $\mathbf{B}(\boldsymbol{\rho})$ fields in (3.6), lead to a determinantal equation $\det \mathbb{A}^{\text{TE,HE}}(x) = 0$, which resolves the cutoff x for TE or HE modes,

Table   **3.1** x for   uniaxial   loaded   waveguide.
Values of parameters: $\boldsymbol{\epsilon}_r = \{2.54, 0, 4\}$ and $\boldsymbol{\mu}_r = \{1, 0, 1\}$.

	TE_{mq}			TM_{mq}		
		CFVIE	SVM		CFVIE	SVM
No	m, q	x	x	m, q	x	x
1	$\pm 1, 1$	1.1553	1.1553	$0, 1$	1.2024	1.2024
2	$\pm 2, 1$	1.9164	1.9164	$\pm 1, 1$	1.9159	1.9159
3	$0, 1$	2.4042	2.4042	$\pm 2, 1$	2.5679	2.5678
4	$\pm 3, 2$	2.6361	2.6361	$0, 2$	2.7601	2.7600
5	$\pm 4, 1$	3.3366	3.3365	$\pm 3, 1$	3.1901	3.1901
6	$\pm 1, 2$	3.3453	3.3452	$\pm 1, 2$	3.5079	3.5078
7	$\pm 5, 1$	4.0257	4.0255	$\pm 4, 1$	3.7943	3.7942
8	$\pm 2, 2$	4.2079	4.2078	$\pm 2, 2$	4.2088	4.2086
9	$0, 2$	4.4021	4.4020	$0, 3$	4.3271	4.3269
10	$\pm 3, 2$	5.0294	5.0292	$\pm 5, 1$	4.3859	4.3857

depending on the type of anisotropy and on homogeneous/inhomogeneous infill. Similarly, the remaining four sets construct $\det \mathbb{A}^{\text{TM,EH}}(x) = 0$, which determines the cutoff x for TM or EH modes.

3.5   *Numerical Results*

The CFVIE-CDSE is firstly validated by comparing the cutoff x with the ones from SVM for homogeneous loaded waveguides. From (3.15), (3.16) we see that the characteristic equations for the isotropic and uniaxial case are identical. For this reason we skip the validation for the isotropic infill and present only the uniaxial loading. The values of parameters used are given in Table 3.1 where we use the set notations $\boldsymbol{\epsilon}_r = \{\epsilon_{1r}, \epsilon_{2r}, \epsilon_{3r}\}$ and $\boldsymbol{\mu}_r = \{\mu_{1r}, \mu_{2r}, \mu_{3r}\}$ to declare the relative permittivity and permeability elements of (3.1). This introductory example has only one DoF. In Table 3.1 the first ten sequential cutoff x are shown. The agreement up to five significant figures between CFVIE and SVM, for this introductory example, is evident.

Next example concerns a gyroelectric loading, as shown in Table 3.2. This case has two DoF, one additional to the above example due to the gyroelectric loading. The x for SVM are obtained from (3.19). Apart from the evident agreement between CFVIE and SVM, the x for the EH modes are the same with the ones depicted in Table 3.1 for TM modes, since the same numerical value $\epsilon_{3r} = 4$ is used in both examples and because the characteristic equations for these mode families are the same. A notable feature here is that gyroelectricity introduces m-nondegeneracy. This means that the cutoff x for $+|m|$ has different value as compared to the one for $-|m|$. This is observed for HE modes only, since the gyroelectric term ϵ_{2r} exists only in the characteristic equation (3.19) for these specific modes. Contrariwise, the cutoff x for EH modes obey $|m|$-nondegeneracy, i.e., the cutoff x for $\pm|m|$ are the same. To fortify the validity of CFVIE for gyroelectric loadings, we also compare it with [116] by recalculating the cutoff x depicted in Fig. 4 of [116]—using $\boldsymbol{\epsilon}_r = \{3.6, 1, 3.2\}$ and $\boldsymbol{\mu}_r = \{1, 0, 1\}$—by setting there $k_z a = 0$. Since x in [116] are part of a Figure and not given in decimal form, we cannot compare in terms of accuracy. Nevertheless, the x from CFVIE are 0.87824 ($m = 1$), 1.1164 ($m = -1$), 1.4745 ($m = 2$), 1.8303 ($m = -2$), and 2.1022 ($m = 0$) for HE modes, while for EH

Table 3.2 x for gyroelectric loaded waveguide. Values of parameters: $\boldsymbol{\epsilon}_r = \{2.54, 0.1, 4\}$ and $\boldsymbol{\mu}_r = \{1, 0, 1\}$.

No	HE$_{mq}$ m, q	CFVIE x	SVM x	EH$_{mq}$ m, q	CFVIE x	SVM x
1	$+1, 1$	1.1368	1.1368	$0, 1$	1.2024	1.2024
2	$-1, 1$	1.1749	1.1749	$\pm 1, 1$	1.9159	1.9159
3	$+2, 1$	1.8890	1.8890	$\pm 2, 1$	2.5679	2.5678
4	$-2, 2$	1.9457	1.9457	$0, 2$	2.7601	2.7600
5	$0, 1$	2.4061	2.4061	$\pm 3, 1$	3.1902	3.1901
6	$+3, 2$	2.6014	2.6013	$\pm 1, 2$	3.5079	3.5078
7	$-3, 1$	2.6734	2.6734	$\pm 4, 1$	3.7943	3.7942
8	$+4, 2$	3.2954	3.2953	$\pm 2, 2$	4.2088	4.2086
9	$+1, 2$	3.3431	3.3430	$0, 3$	4.3271	4.3269
10	$-1, 2$	3.3527	3.3526	$\pm 5, 1$	4.3859	4.3857

modes we get 1.3443 ($m = 0$). Careful inspection of these values reveals that they match to the ones in Fig. 4 of [116].

In Table 3.3 we proceed to a two-layered isotropic loaded waveguide with two DoF. Here, we compare the CFVIE with the SVM solution given in [87] and with HFSS. Since HFSS computes directly the cutoff frequencies f, we compare the f by calculating the frequency from CFVIE and [87] via $f = x/(2\pi a\sqrt{\epsilon_0 \mu_0})$ where we have set an indicative radius $a = 1$ cm. Table 3.3 lists the first eight successive cutoff f. Based on the analysis of Section "Modified two dimensional tensorial Green's function", $m = 0$ yields TE/TM modes. The comparison establishes an agreement, up to five significant figures between CFVIE and [87], and up to three significant figures, between CFVIE and HFSS. This is because HFSS resolves the f without enough accuracy. In particular, we have initialized HFSS using a surface deviation of 0.04 cm for mesh setting and 0.333 lambda refinement ratio. Then we performed a parametric sweep in the range $[f_{\mathrm{CFVIE}} - 0.05 \text{ GHz}, f_{\mathrm{CFVIE}} + 0.05 \text{ GHz}]$, where f_{CFVIE} is the cutoff frequency as predicted by CFVIE. The step used for this sweep was 0.001 GHz or, equivalently, 101 iterations. With this step, HFSS yields the result in three decimal digits, that is why the first three f shown in Table 3.3 have one less decimal digit than the ones obtained from CFVIE. To attain one more decimal digit, one should decrease the step to 0.0001 GHz, but this would result to ten times more CPU time. In Table 3.4 we collect the data regarding the computational performance of various examples examined. The CPU time required to compute only one f from the depicted list with HFSS is 1200 s, with a fair RAM consumption of 0.4 GB. The simulation should be repeated for the rest f, thus constituting this commercial solver inefficient for such kind of computations. In addition, it should be kept in mind that we have performed the sweep in an *a priori* targeted range defined by firstly computing the cutoff f through CFVIE, otherwise it would take much more time to determine the positions of the cutoff f purely via HFSS. On the other hand, the CFVIE requires 5.4 s CPU time to compute only one f with 0.05 GB RAM, using $L = 20$ number of l terms in the truncation scheme. The value $L = 20$ was selected in order to establish a relative error less than 10^{-3}. Denoting the SVM solution of [87] as x_e, and employing it as the exact solution, the relative error $|x_a - x_e|/|x_e|$ for the fundamental $x_a = 4.8456$, where x_a is the approximate value obtained by CFVIE, is 3.1×10^{-4}. On the contrary, the relative

Table 3.3 x and f for two-layered isotropic loaded waveguide. Inner layer: $\epsilon_r = \{2.54, 0, 2.54\}$, $\rho \in [0, a/2]$; outer layer: $\epsilon_r = \{4, 0, 4\}$, $\rho \in (a/2, a]$; rest values: $\boldsymbol{\mu}_r = \{1, 0, 1\}$, $\rho \in [0, a]$ and $a = 1$ cm. * This is a TE_{01} mode. † These are TM_{01} and TM_{02} modes.

No	HE_{mq} m, q	CFVIE f(GHz)	[87] f(GHz)	HFSS f(GHz)	EH_{mq} m, q	CFVIE f(GHz)	[87] f(GHz)	HFSS f(GHz)
1	$\pm 1, 1$	4.8456	4.8441	4.852	$0, 1^\dagger$	6.5391	6.5344	6.568
2	$\pm 2, 1$	7.5893	7.5875	7.609	$\pm 1, 1$	9.7944	9.7875	9.838
3	$0, 1^*$	9.7944	9.7875	9.819	$\pm 2, 1$	12.698	12.692	12.792
4	$\pm 3, 1$	10.195	10.193	10.226	$0, 2^\dagger$	14.648	14.648	14.778
5	$\pm 4, 1$	12.778	12.777	12.801	$\pm 3, 1$	15.504	15.499	15.618
6	$\pm 1, 2$	13.749	13.747	13.839	$\pm 4, 1$	18.275	18.271	18.343
7	$\pm 5, 1$	15.353	15.352	15.385	$\pm 1, 2$	18.906	18.896	18.998
8	$\pm 2, 2$	17.352	17.351	17.379	$\pm 5, 1$	21.027	21.024	21.145

Table 3.4 Computational performance on a 2.26 GHz double quad-core equipped machine. HFSS initialization: 0.04 cm surface deviation, 0.333 lambda refinement ratio, 1st order solver, and 10^{-6} relative residual. * Fundamental $HE_{\pm 1, 1}$ mode.

Example	CFVIE CPU time (s)	RAM (GB)	L	HFSS CPU time (s)	RAM (GB)
Table 3.3	5.4	0.05	20	1200	0.4
Table 3.6	4.4	0.06	20	1180	2.5
Table 3.8*	2.3	0.05	8	—	—
Table 3.8	4.2	0.05	20	—	—

error for HFSS's $x_a = 4.852$ is 1.6×10^{-3}, almost one order of magnitude greater. In some cases, with the same $L = 20$, even lower relative errors are maintained for CFVIE, as for the $x_a = 14.648$ of the TM_{02} mode.

A serious limitation regarding HFSS is that it cannot retrieve higher-order cutoff f when the waveguide is filled with a gyroelectric medium. In particular, the commercial software returns only the fundamental f. This is depicted in Table 3.5, where a core-shell infill is used and each layer has different gyroelectric properties. This example has three DoF, one due to radius a, one due to the two-layered configuration, and one due to the gyroelectric loading. The validity for this case is established only for the lowest f from both mode families, i.e., the cutoff f for HE_{11} mode. For the remaining higher-order f computed by CFVIE, we have performed a self-validity test by progressively increasing the number of terms L in the truncation strategy, and achieved convergence up to five significant digits, as listed in Table 3.5. In addition, we point out that the only difference between the examples of Tables 3.3 and 3.5 is the values in permittivity tensors, otherwise the setups are identical. Therefore, the two-layered setup results in Table 3.5 are confident, because the CFVIE has been successfully validated for a two-layered configuration in Table 3.3. In Table 3.6 we present a three-layered gyroelectric loaded waveguide with four DoF. Same conclusions for HFSS as the ones above can be drawn. Still, the CFVIE yields convergent results for higher-order cutoff f, while the compu-

Table 3.5 x and f for two-layered gyroelectric loaded waveguide. Inner layer: $\epsilon_r = \{2.54, 0.1, 3\}$, $\rho \in [0, a/2]$; outer layer: $\epsilon_r = \{2, 0.2, 4\}$, $\rho \in (a/2, a]$; rest values: $\boldsymbol{\mu}_r = \{1, 0, 1\}$, $\rho \in [0, a]$ and $a = 1$ cm.

| No | HE$_{mq}$ | | | | EH$_{mq}$ | | | |
| | | CFVIE | | HFSS | | CFVIE | | HFSS |
	m, q	x	f(GHz)	f(GHz)	m, q	x	f(GHz)	f(GHz)
1	$1, 1$	1.2068	5.7581	5.795	$0, 1$	1.3114	6.2570	—
2	$-1, 1$	1.2737	6.0772	—	$\pm 1, 1$	2.0089	9.5852	—
3	$2, 1$	2.0537	9.7990	—	$\pm 2, 1$	2.6330	12.563	—
4	$-2, 1$	2.1809	10.406	—	$0, 2$	2.9486	14.069	—
5	$0, 1$	2.5832	12.325	—	$\pm 3, 1$	3.2320	15.421	—
6	$3, 1$	2.8582	13.637	—	$\pm 1, 2$	3.7914	18.090	—
7	$-3, 1$	3.0413	14.511	—	$\pm 4, 1$	3.8197	18.225	—
8	$-1, 2$	3.6198	17.271	—	$\pm 5, 1$	4.4008	20.998	—

Table 3.6 x and f for three-layered gyroelectric loaded waveguide. Inner layer: $\epsilon_r = \{2, 0.1, 3\}$, $\rho \in [0, 0.2a]$; intermediate layer: $\epsilon_r = \{2.54, 0.2, 4\}$, $\rho \in (0.2a, 0.6a]$; outer layer: $\epsilon_r = \{4, 0.3, 5\}$, $\rho \in (0.6a, a]$; rest values: $\boldsymbol{\mu}_r = \{1, 0, 1\}$, $\rho \in [0, a]$ and $a = 1$ cm.

| No | HE$_{mq}$ | | | | EH$_{mq}$ | | | |
| | | CFVIE | | HFSS | | CFVIE | | HFSS |
	m, q	x	f(GHz)	f(GHz)	m, q	x	f(GHz)	f(GHz)
1	$1, 1$	1.0245	4.8881	4.951	$0, 1$	1.1915	5.6852	—
2	$-1, 1$	1.0974	5.2362	—	$\pm 1, 1$	1.8245	8.7053	—
3	$2, 1$	1.5927	7.5992	—	$\pm 2, 1$	2.3947	11.426	—
4	$-2, 1$	1.6973	8.0987	—	$0, 2$	2.6931	12.850	—
5	$3, 1$	2.1259	10.144	—	$\pm 3, 1$	2.9337	13.998	—
6	$0, 1$	2.1558	10.286	—	$\pm 1, 2$	3.3673	16.067	—
7	$-3, 1$	2.2524	10.747	—	$\pm 4, 1$	3.4563	16.491	—
8	$-4, 1$	2.6502	12.645	—	$\pm 5, 1$	3.970	18.942	—

tational comparison for the first cutoff x between CFVIE and HFSS is given in Table 3.4. Overall, the CFVIE constitutes a valuable tool for the efficient and accurate calculation of the cutoff x, or f, in gyrotropic loaded waveguides, taking into account that the FEM employed in HFSS requires huge CPU time to extract the cutoff frequencies with moderate accuracy.

All previous examples concerned gyroelectric infills. In Table 3.7 we study a gyromagnetic infill with two DoF, and compare the CFVIE with SVM. Apart from excellent agreement, there is a distinctive difference between the present case and the gyroelectric case of Table 3.2, i.e., the cutoff x for HE modes do not obey m-nondegeneracy as the respective ones in Table 3.2 do. This is owing to the absence of the first term in the first eq. of (3.19), and therefore the same roots are obtained for $\pm |m|$.

In Figure 3.2 we plot the modal components for the first four modes, per HE/EH mode family, for the gyroelctric loaded waveguide of Table 3.2. In particular, we depict the normalized real part—denoted as Re in the caption of Figure

Table 3.7 x for gyromagnetic loaded waveguide. Values of parameters: $\boldsymbol{\mu}_r = \{2, 0.2, 4\}$ and $\boldsymbol{\epsilon}_r = \{1, 0, 1\}$.

| | HE_{mq} | | | EH_{mq} | | |
| | | CFVIE | SVM | | CFVIE | SVM |
No	m, q	x	x	m, q	x	x
1	$\pm 1, 1$	0.9206	0.9206	$0, 1$	1.7090	1.7090
2	$\pm 2, 1$	1.5271	1.5271	$\pm 1, 1$	2.7231	2.7231
3	$0, 1$	1.9159	1.9159	$\pm 2, 1$	3.6498	3.6497
4	$\pm 3, 1$	2.1006	2.1006	$0, 2$	3.9230	3.9230
5	$\pm 4, 1$	2.6588	2.6588	$\pm 3, 1$	4.5342	4.5342
6	$\pm 1, 2$	2.6657	2.6657	$\pm 1, 2$	4.9858	4.9858
7	$\pm 5, 1$	3.2078	3.2078	$\pm 4, 1$	5.3928	5.3928
8	$\pm 2, 2$	3.3531	3.3531	$\pm 2, 2$	5.9819	5.9819
9	$0, 2$	3.5078	3.5078	$0, 3$	6.1500	6.1499
10	$\pm 3, 2$	3.7506	3.7506	$\pm 5, 1$	6.2337	6.2336
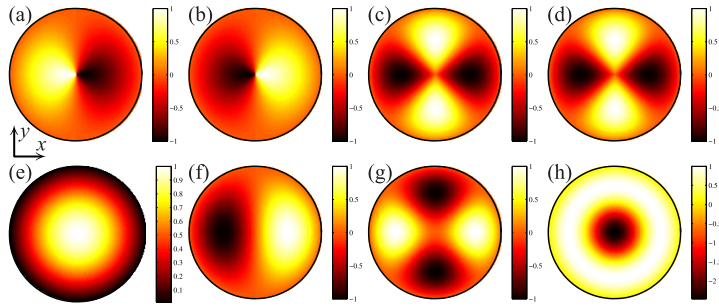
Figure 3.2 Modal electric field components for the gyroelectric loaded waveguide of Table 3.2, as calculated by CFVIE. (a)–(d): $\text{Re}\{E_\varphi\}/\max\{\text{Re}\{E_\varphi\}\}$ for HE modes. (a) 1st mode/$x = 1.1368$; (b) 2nd mode/$x = 1.1749$; (c) 3rd mode/$x = 1.8890$; (d) 4th mode/$x = 1.9457$. (e)–(h): $\text{Re}\{E_z\}/\max\{\text{Re}\{E_z\}\}$ for EH modes. (e) 1st mode/$x = 1.2024$; (f) 2nd mode/$x = 1.9159$; (g) 3rd mode/$x = 2.5679$; (h) 4th mode/$x = 2.7601$.

3.2—of the tangential to the waveguide's wall components E_φ, E_z, on xy plane. The pictures in Figure 3.2 have been obtained by CFVIE, and are exactly the same with the ones obtained by SVM and not depicted here to save some space. This constitutes an extra validation test for the CFVIE. In addition, the BCs $E_\varphi = 0$ and $E_z = 0$ at $\rho = a$ are fully satisfied. Finally, it should be clarified that the similar patterns in Figure 3.2(c), (d) are due to the normalization used, otherwise the unnormalized $\text{Re}\{E_\varphi\}$ patterns differ in magnitude.

One of the merits of our method is its capacity to resolve the cutoff x for continuously varying highly inhomogeneous infills. To demonstrate this capability, we assume the isotropic continuously varying permittivity $\boldsymbol{\epsilon}_r(\rho) = \{\epsilon_r(\rho), 0, \epsilon_r(\rho)\}$, $\epsilon_r(\rho) = 2 - (\rho/a)^2$, $\rho \in [0, a]$, which corresponds to Luneberg lens profile. This case has only one DoF, because the lens is not tunable. This example is difficult to simulate by HFSS, because its FEM solver would require a seriously dense mesh to capture a continuously varying permittivity. On the contrary, the mesh-free CFVIE relies on simple radial integrations over the inhomogeneous profile. To state

Table 3.8 Convergence history of x for HE_{mq} and EH_{mq} modes for a highly inhomogeneous loaded waveguide, due to different truncation number L. Values of parameters: $\boldsymbol{\epsilon}_r(\rho) = \{\epsilon_r(\rho), 0, \epsilon_r(\rho)\}$, $\epsilon_r(\rho) = 2 - (\rho/a)^2$, $\boldsymbol{\mu}_r = \{1, 0, 1\}$, $\rho \in [0, a]$.
* These are TE_{01} and TE_{02} modes. † These are TM_{01}, TM_{02} and TM_{03} modes.

x for HE_{mq} modes

L	1st $\pm 1,1$	2nd $\pm 2,1$	3rd $0,1^*$	4th $\pm 3,1$	5th $\pm 1,2$	6th $\pm 4,1$	7th $\pm 2,2$	8th $0,2^*$	9th $\pm 5,1$	10th $\pm 3,2$
6	1.45821	2.53028	2.96059	3.57216	4.15599	4.60160	5.28557	5.44327	5.62406	6.38275
8	1.45822	2.53022	2.96061	3.57226	4.15607	4.60180	5.28574	5.44343	5.62440	6.38305
10	1.45822	2.53023	2.96062	3.57231	4.15611	4.60188	5.28582	5.44350	5.62454	6.38317
12	1.45822	2.53024	2.96063	3.57232	4.15613	4.60192	5.28585	5.44353	5.62460	6.38323
14	1.45822	2.53024	2.96063	3.57233	4.15614	4.60194	5.28587	5.44355	5.62464	6.38326
16	1.45822	2.53025	2.96063	3.57234	4.15614	4.60195	5.28588	5.44356	5.62466	6.38327
18	1.45822	2.53025	2.96063	3.57234	4.15614	4.60196	5.28588	5.44356	5.62467	6.38328
20	1.45822	2.53025	2.96063	3.57234	4.15615	4.60197	5.28589	5.44357	5.62468	6.38329
22	1.45822	2.53025	2.96063	3.57235	4.15615	4.60197	5.28589	5.44357	5.62468	6.38329

x for EH_{mq} modes

| L	1st $0,1^\dagger$	2nd $\pm 1,1$	3rd $\pm 2,1$	4th $0,2^\dagger$	5th $\pm 3,1$	6th $\pm 1,2$	7th $\pm 4,1$	8th $\pm 2,2$	9th $0,3^\dagger$	10th $\pm 5,1$
6	1.79947	2.96054	4.05680	4.25359	5.12493	5.44296	6.17723	6.58380	6.70265	7.21937
8	1.79949	2.96060	4.05691	4.25384	5.12509	5.44335	6.17745	6.58434	6.70386	7.21965
10	1.79950	2.96062	4.05694	4.25391	5.12515	5.44347	6.17752	6.58451	6.70418	7.21975
12	1.79950	2.96062	4.05696	4.25394	5.12517	5.44352	6.17756	6.58458	6.70429	7.21980
14	1.79950	2.96063	4.05697	4.25395	5.12519	5.44354	6.17758	6.58462	6.70434	7.21983
16	1.79950	2.96063	4.05697	4.25395	5.12519	5.44356	6.17759	6.58463	6.70437	7.21984
18	1.79950	2.96063	4.05697	4.25396	5.12520	5.44356	6.17759	6.58464	6.70438	7.21985
20	1.79950	2.96063	4.05697	4.25396	5.12520	5.44357	6.17760	6.58465	6.70439	7.21985
22	1.79950	2.96063	4.05698	4.25396	5.12520	5.44357	6.17760	6.58465	6.70440	7.21985
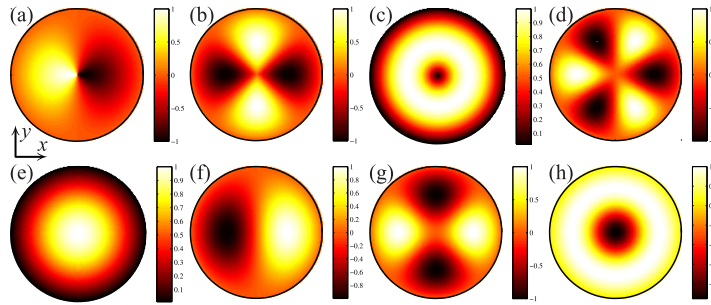
Figure 3.3   Modal electric field components for the Luneberg loaded waveguide of Table 3.8, as calculated by CFVIE. (a)–(d): $\text{Re}\{E_\varphi\}/\max\{\text{Re}\{E_\varphi\}\}$ for HE modes. (a) 1st mode/$x = 1.4582$; (b) 2nd mode/$x = 2.5303$; (c) 3rd mode/$x = 2.9606$; (d) 4th mode/$x = 3.5724$. (e)–(h): $\text{Re}\{E_z\}/\max\{\text{Re}\{E_z\}\}$ for EH modes. (e) 1st mode/$x = 1.7995$; (f) 2nd mode/$x = 2.9606$; (g) 3rd mode/$x = 4.0570$; (h) 4th mode/$x = 4.2540$.

validity, in Table 3.8 we depict the convergence history for the first ten successive cutoff x, for both HE/EH modes, by progressively increasing the number of terms L in the truncation scheme. The x are depicted up to six significant digits in order to conclude about convergence. Still, the $m = 0$ case yields TE/TM modes. As expected, the higher-order x, as compared to the lower-order ones, require, in general, more terms to converge. For instance, if we focus on the first x of $\text{HE}_{\pm 1,1}$ mode, the CFVIE requires $L = 8$ terms to secure the fifth significant figure and yields the rounded result $x = 1.4582$. On the contrary, for the fifth x of $\text{HE}_{\pm 1,2}$ mode, the CFVIE requires $L = 20$ terms to finally yield $x = 4.1562$. The computation performance of CFVIE for these two cases is given in Table 3.4. In case the convergence is examined only on the fourth significant digit, $L = 12$ is adequate for retrieving all x given in Table 3.8, with 3 s execution time for the CFVIE for each cutoff x. Although there is no particular rule of thumb, the number L of terms required for convergence to a specific number of significant digits, generally depends on the electric size of x and on degree of inhomogeneity, especially if the infill is step discontinuous as in Tables 3.3, 3.5, 3.6. For the fundamental cutoff x of a homogeneous or of a continuously varying permittivity, 10 terms would suffice, but for a combination of a step discontinuous permittivity with higher-order x, more terms are required. Finally, in Figure 3.3 we plot the modal components for the first four modes given in Table 3.8, per HE/EH mode family. As it is evident, the BCs $E_\varphi = 0$—for HE modes—and $E_z = 0$—for EH modes—at $\rho = a$, are fully satisfied.

3.6   Conclusion

We calculated the normalized cutoff wavenumbers of circular metallic walled waveguides, with continuously varying highly inhomogeneous gyrotropic infill. To this end we developed a CFVIE-CDSE method which features modified 2-D tensorial GFs, that enable the satisfaction of the electric BCs on waveguide's metallic wall. The CFVIEs were solved using entire domain orthogonal Dini-type CVWFs, for the expansion of the fields inside the waveguide. This kind of expansion resulted in the reduction of the 2-D volumetric-type integrals to sets of algebraic equations. We characterized the types of modes maintained in such waveguiding structures, we

exhaustively validated the CFVIE-CDSE vs SVM for homogeneously loaded waveguides, vs HFSS for two-layered isotropic and three-layered gyroelectric infills, and examined the convergence of our method for a highly inhomogeneous infill.

Calculation of Complex WGM Frequencies for Gyroelectric Cylindrical Resonator

Asymptotic closed-form expressions for the calculation of the complex TE/TM whispering gallery mode (WGM) frequencies, in homogeneous gyroelectric circular cylindrical resonators of infinite length, are derived. In addition, we extend a recently developed volume integral equation-cylindrical Dini series expansion (VIE-CDSE) method, so as to support the prediction of the complex WGMs for continuously varying highly inhomogeneous gyroelectric circular cylindrical resonators. To this end, VIE's entire domain orthogonal vectorial basis is extended to support, via asymptotic closed-form expressions, very large indices of the involved Dini-type cylindrical vector wave functions (CVWFs). This way, the eigenbasis required for the solution of the VIE becomes free of numerical instabilities, arising when very large orders of the involved Bessel functions are employed. The complex frequencies obtained by the asymptotic closed-form expressions for the case of the homogeneous gyroelectric resonator, as well as those obtained by the VIE when the multilayered gyroelectric resonator is reduced to one layer, are validated by comparisons with the complex roots extracted by numerically solving the TE/TM characteristic equations obtained from the separation of variables method (SVM), using complex root finding techniques. We demonstrate the calculation of very high order WGM frequencies for cylindrical resonators composed of homogeneous and highly inhomogeneous permittivity profiles. This asymptotic theory constitutes a rigorous tool which may serve for verification of method of analytical regularisation (MAR)-based numerical solutions for other non-circular inhomogeneous cylinders, and for the interpretation of experimental data for applications such as WGM lasing, refractometric sensing, and magneto-optic coupling.

4.1   Introduction

WGMs of dielectric resonators have attracted increasing attention during recent years, due to their numerous applications ranging from the microwave to the optical frequency regime [122-125]. Among several geometries that can support WGMs, is also the cylindrical resonator. In this context, the propagation of WGMs in an infinite isotropic dielectric cylinder was first studied in [126]. A theoretical and experimental study of terahertz WGMs in a dielectric cylinder coupled to a slab waveguide was presented in [127], while light propagation via WGMs in coupled microcylinders was investigated in [128]. An analysis of the WGM complex natural frequencies of compact and hollow dielectric cylinders immersed in a layered medium was presented in [129]. In addition, the excitation of WGMs in multi-layered dielectric cylinders was examined in [130]. On the other hand, recent applications on spherical geometries, such as WGM lasing, refractometric sensing, and magneto-optic coupling, have shown the theoretical and practical interest that resides in the investigation of the whispering gallery spectra of anisotropic resonators [131-136]. However, although resonant anisotropic cylindrical structures have received the attention of researchers [137-139], the theoretical study of their WGMs remains limited. In particular, the resonant frequencies of higher-order—but not whispering gallery—modes in cylindrical anisotropic dielectric resonators were calculated in [140], whereas low-Q WGMs of cylindrical metamaterial shells were studied in [141].

   In this work we derive the complex WGM frequencies arising in homogeneous and in continuously varying highly inhomogeneous gyroelectric circular cylindrical resonators, with infinite length in z direction. In general, the cylindrical resonator is described by an inhomogeneous gyroelectric permittivity tensor, given by

$$\boldsymbol{\epsilon}(\rho) = \epsilon_0 \begin{bmatrix} \epsilon_{1r}(\rho) & i\epsilon_{2r}(\rho) & 0 \\ -i\epsilon_{2r}(\rho) & \epsilon_{1r}(\rho) & 0 \\ 0 & 0 & \epsilon_{3r}(\rho) \end{bmatrix}, \qquad (4.1)$$

where ϵ_{1r}, ϵ_{2r}, ϵ_{3r} are the relative components, ϵ_0 is the free space permittivity, and ρ the radial distance in the polar coordinate system. The permeability of the resonator is $\mu = \mu_0$, that of free space.

   For the case of homogeneous resonators—i.e., (4.1) does not depend on ρ—asymptotic closed-form expressions are constructed valid for very large mode order, by appropriately applying large order expansions of Bessel, Neumann and Hankel functions appearing in the characteristic equations of TE/TM modes. In the past, asymptotic closed-form expressions for the TE/TM modes of homogeneous isotropic spherical resonators have been extracted in [142]. Those expansions are similar to the TM case examined in the present work, with the difference that spherical Bessel functions were involved in the characteristic equations of [142], instead of the cylindrical functions appearing here. This similarity in the asymptotics stems from the fact that TM modes' complex WGM frequencies of the present problem do not depend on the gyroelectric element ϵ_{2r}. However, the present TE case is more challenging because the complex WGM frequencies also depend on the gyroelectric element ϵ_{2r}. This element adds an additional term in the characteristic equation of TE modes, which complicates the analysis for yielding the asymptotic expressions. In addition, it is known that gyroelectricity lifts m-degeneracy—where m is the order of the cylindrical wavefunctions. That is to say, the complex WGM frequencies are different in value when $m \lessgtr 0$—while, for TM modes, they have the same value and

thus in that case they degenerate vs m. Therefore, one has to derive two closed-form expressions for the TE case, one when $m > 0$ and one when $m < 0$. To the authors' knowledge, asymptotic closed-form solutions for TE WGMs in gyroelectric cylindrical resonators, have not been reported before.

For the case of inhomogeneous resonators, a VIE-CDSE method [119] is extended to support the calculation of very large mode order complex WGM frequencies of continuously varying highly inhomogeneous resonators. The solution of the original VIE in [119] is based on the construction of an orthogonal vectorial Dini-type CVWF-based eigenbasis by numerical evaluation of real roots of two eigenequations for moderate order values of the involved Bessel functions—for details see Section 4.3.1. To apply the VIE for the calculation of the WGM frequencies, however, the computation of the aforementioned real roots for very large orders is required, a demanding task for any root finding algorithm due to the loss of roots when m is very large. In case of root loss, the eigenbasis is not orthogonal anymore, an undesired situation for the VIE which in sequence does not yield the expected complex roots. To overpass this obstacle, we apply large order expansions on Bessel functions appearing in the aforementioned eigenequations, in order to render the VIE suitable for WGM studies. Respective large order expansions were applied in the vectorial eigenbasis of the VIE for WGM lasing in gyroelectric spherical resonators [136]. However, the present TE case requires a different approach than in [136]. This distinction constitutes an additional novel point of the present effort and reflects the influence of gyroelectricity in the calculation of the TE complex WGM frequencies, with the latter being obviously different between cylindrical and spherical anisotropic resonators.

To validate the derived asymptotics, we compare the complex WGM frequencies obtained by the closed-form expressions for the case of the homogeneous gyroelectric resonator, as well as those obtained by the VIE when the multilayered gyroelectric resonator is reduced to one layer, with the complex roots extracted from the numerical solution of the exact TE/TM characteristic equations, using complex root finding techniques. Then, we demonstrate the calculation of very high order WGM frequencies for cylindrical resonators composed of homogeneous and highly inhomogeneous permittivity profiles.

4.2   Homogeneous gyroelectric resonators

4.2.1   Charasteristic equations

For homogeneous gyroelectric resonators, the characteristic equations for TE/TM modes are derived from the exact solution of EM plane wave scattering by gyroelectric cylinders, using the SVM [59]. Employing the $\exp(i\omega t)$ time dependence, the z-components of the magnetic fields for TE modes are expanded as

$$H_z^{\text{inc}} = H_0 \sum_{m=-\infty}^{\infty} i^{-m} J_m(k_0\rho) e^{-im\varphi},$$

$$H_z^{\text{sc}} = \sum_{m=-\infty}^{\infty} A_m H_m(k_0\rho) e^{-im\varphi},$$

$$H_z^{\text{int}} = \sum_{m=-\infty}^{\infty} B_m J_m(K^H\rho) e^{-im\varphi}, \tag{4.2}$$

where H_z^{inc}, H_z^{sc} and H_z^{int} are the incident, scattered, and internal magnetic fields, J_m is Bessel function, H_m is Hankel function of the second kind—the standard superscript (2) notation is omitted for simplicity—$k_0 = \omega\sqrt{\epsilon_0\mu_0}$ the free space wavenumber, $K^H = k_0/\sqrt{\epsilon_\perp}$—with $\epsilon_\perp = \epsilon_{1r}/(\epsilon_{1r}^2 - \epsilon_{2r}^2)$—$H_0$ the magnitude of H_z^{inc}, and A_m, B_m unknown expansion coefficients. The remaining electric field components E_ρ, E_φ are derived by $\mathbf{E} = 1/(i\omega)\boldsymbol{\epsilon}^{-1}\nabla \times \mathbf{H}$. For TM modes, (4.2) hold true with H_z replaced by E_z, K^H by $K^E = \sqrt{\epsilon_{3r}}k_0$, H_0 by E_0, A_m by C_m, and B_m by D_m. The remaining components H_ρ, H_φ are now derived by $\mathbf{H} = -1/(i\omega\mu_0)\nabla \times \mathbf{E}$.

Satisfying, next, at $\rho = a$—where a is the radius of the cylinder—the boundary conditions $H_z^{\mathrm{int}} = H_z^{\mathrm{inc}} + H_z^{\mathrm{sc}}$, $E_\varphi^{\mathrm{int}} = E_\varphi^{\mathrm{inc}} + E_\varphi^{\mathrm{sc}}$ for TE modes, and $E_z^{\mathrm{int}} = E_z^{\mathrm{inc}} + E_z^{\mathrm{sc}}$, $H_\varphi^{\mathrm{int}} = H_\varphi^{\mathrm{inc}} + H_\varphi^{\mathrm{sc}}$ for TM modes, one ends up, exactly, to the following matrix equation for the calculation of the scattered coefficients A_m, C_m, i.e.,

$$\begin{bmatrix} A_m \\ C_m \end{bmatrix} = \mathbb{T} \begin{bmatrix} H_0 i^{-m} \\ E_0 i^{-m} \end{bmatrix} \quad \text{or} \quad \mathbb{T}^{-1} \begin{bmatrix} A_m \\ C_m \end{bmatrix} = \begin{bmatrix} H_0 i^{-m} \\ E_0 i^{-m} \end{bmatrix}, \tag{4.3}$$

with $\mathbb{T}$ the transition matrix. The complex natural frequencies are extracted from (4.3) in absence of incident excitation, therefore, for nontrivial solutions, the condition $\det\{\mathbb{T}^{-1}\} = 0$ must be enforced [143]. Since $\mathbb{T}$ is diagonal, this latter condition yields exactly the following two characteristic equations for TE/TM modes, i.e.,

$$\epsilon_\perp \frac{x}{\sqrt{\epsilon_\perp}} \frac{J_m'(x/\sqrt{\epsilon_\perp})}{J_m(x/\sqrt{\epsilon_\perp})} = \epsilon_x m + x \frac{H_m'(x)}{H_m(x)} \qquad \text{(TE modes)},$$

$$\sqrt{\epsilon_3} \frac{J_m'(x\sqrt{\epsilon_3})}{J_m(x\sqrt{\epsilon_3})} = \frac{H_m'(x)}{H_m(x)} \qquad \text{(TM modes)}. \tag{4.4}$$

In (4.4), J_m' and H_m' are the derivatives of J_m and H_m with respect to the argument and $\epsilon_x = \epsilon_{2r}/(\epsilon_{1r}^2 - \epsilon_{2r}^2)$. The characteristic equations (4.4) have complex solutions $x_l = u_l + iv_l$, $l = 1, 2, \ldots$, $u_l \equiv \mathrm{Re}\{x_l\} > 0$, $v_l \equiv \mathrm{Im}\{x_l\} \geqslant 0$—where Re/Im denotes the real/imaginary part—which are the complex normalized wavenumbers $x_l = k_{0,l}a$, $k_{0,l} = \omega_l\sqrt{\epsilon_0\mu_0}$, of the gyroelectric cylindrical resonator. The complex natural frequencies are then given by $f_l = cx_l/(2\pi a) \equiv \mathrm{Re}\{f_l\} + i\mathrm{Im}\{f_l\}$—with c the speed of light in vacuum—where $\mathrm{Re}\{f_l\}$ is the natural frequency and $2\mathrm{Im}\{f_l\}$ is the linewidth of the resonance. The respective quality factor is given by $Q_l = \mathrm{Re}\{f_l\}/[2\mathrm{Im}\{f_l\}]$. Based on the above, a mode, in general, is classified by m, l indices, thus designating it as TE_{ml} or TM_{ml}.

From (4.4) it is evident that only TE modes depend on the gyroelectric element ϵ_{2r} through $\epsilon_\perp$ and ϵ_x. In particular, gyroelectricity introduces the additional term $\epsilon_x m$ in the right-hand side of (4.4)/(TE modes), as compared to (4.4)/(TM modes). Moreover, the fractions of Bessel and Hankel functions in (4.4)/(TE modes) are multiplied by x. It is also known that gyroelectricity lifts m-degeneracy, i.e., x_l for (4.4)/(TE modes) are different in value when $m \lessgtr 0$—while, for TM modes, they have the same value and thus in that case they degenerate vs m. Therefore, one has to derive two closed-form expressions for the TE case, one when $m > 0$ and one when $m < 0$. Overall, these factors complicate the asymptotic analysis for TE modes.

In general, WGMs are TE_{ml} or TM_{ml} modes when $|m|$ acquires large values. For a homogeneous resonator, index l of a TE/TM WGM denotes the number of cumulatively localized peaks and valleys of H_z/E_z along the radial direction $0 \leqslant \rho \leqslant a$ of the resonator, while index m denotes either the number of peaks or the number of valleys along the circumference $0 \leqslant \varphi < 2\pi$ of the resonator.

For WGM studies, the condition $1 \ll u < m$—when $m > 0$—must hold, where $u \equiv u_l$ for simplicity. In this case the fraction $H'_m(u)/H_m(u)$ can be simplified using the fact that $|Y_m(u)| \gg |J_m(u)|$, where Y_m is Neumann function. By the aid of Wronskian of Bessel functions, $H'_m(u)/H_m(u) \approx Y'_m(u)/Y_m(u) - i2/[\pi u Y_m^2(u)]$, where Y'_m is the derivative of Y_m with respect to its argument and $Y_m^2(u) \equiv [Y_m(u)]^2$. This latter relation states that u can be obtained from (4.4) if x is replaced by u, and H_m and H'_m are replaced by Y_m and Y'_m, respectively. These modified equations are referred to, below, as large-m characteristic equations.

4.2.2   Asymptotic solution for TE modes

In this Subsection we derive asymptotic closed-form expressions for the complex x as $|m| \to \infty$. In particular, we assume $m > 0$ and after each result we briefly denote the differences for $m < 0$. We separate the analysis in two parts: first, we asymptotically expand u up to $O(|m|^{-2/3})$ and second we construct a first-order expansion for v—where $v \equiv v_l$ for simplicity.

Asymptotic expansion for the real part   We begin with the derivation of the asymptotic solution for u by employing the large-m characteristic equation

$$\epsilon_\perp \frac{u}{\sqrt{\epsilon_\perp}} \frac{J'_m(u/\sqrt{\epsilon_\perp})}{J_m(u/\sqrt{\epsilon_\perp})} = \epsilon_x m + u \frac{Y'_m(u)}{Y_m(u)}. \tag{4.5}$$

Numerical solution of (4.5) reveals that $u/\sqrt{\epsilon_\perp} > m$ while $u < m$—but not $u \ll m$. This instructs that J_m, J'_m must be expanded in the transition region by [144, entries 9.3.23, 9.2.27]. Setting $u/\sqrt{\epsilon_\perp} = m + zm^{1/3}$, to expand u up to $O(m^{-2/3})$, J_m, J'_m must be expanded as

$$J_m(u/\sqrt{\epsilon_\perp}) \underset{m\to\infty}{\sim} \frac{2^{1/3}}{m^{1/3}} \mathrm{Ai}(-2^{1/3}z)\left[1 - \frac{z}{5m^{2/3}}\right]$$
$$+ \frac{2^{2/3}3z^2}{10m} \mathrm{Ai}'(-2^{1/3}z),$$
$$J'_m(u/\sqrt{\epsilon_\perp}) \underset{m\to\infty}{\sim} - \frac{2^{2/3}}{m^{2/3}} \mathrm{Ai}'(-2^{1/3}z)\left[1 - \frac{4z}{5m^{2/3}}\right], \tag{4.6}$$

where Ai is Airy function, Ai′ is its derivative with respect to the argument, and z is a parameter with $O(1)$ first-order Maclaurin series term. The appropriate expansion of z in Maclaurin series will be discussed below. On the contrary, since $u < m$—but not $u \ll m$—Y_m, Y'_m must be expanded using Debye's first-order asymptotic expansions [144, entries 9.3.8, 9.3.12]. Setting $u = m \operatorname{sech} \alpha$, $\alpha > 0$, these expansions read

$$Y_m(u) \underset{m\to\infty}{\sim} - \frac{e^{m(\alpha-\tanh\alpha)}}{\sqrt{\pi m/2 \tanh\alpha}},$$
$$Y'_m(u) \underset{m\to\infty}{\sim} \sqrt{\frac{\sinh(2\alpha)}{\pi m}} e^{m(\alpha-\tanh\alpha)}. \tag{4.7}$$

To yield the $O(m^{-2/3})$ asymptotic solution for u, the z parameter appearing in (4.6) must be expanded in Maclaurin series in the form $2^{1/3}z = z_0 - c_1 m^{-1/3} - c_2 m^{-2/3} - c_3 m^{-1} + O(m^{-4/3})$, with $z_0 = O(1)$ and c_1, c_2, c_3 unknown expansion coefficients to be determined. To determine z_0, we first recognize that $Y'_m(u)/Y_m(u) \sim -\sqrt{\cosh^2\alpha - 1}$, $m \to \infty$, and $\cosh\alpha = [\sqrt{\epsilon_\perp}(1 + zm^{-2/3})]^{-1}$. Then, performing a low-order analysis—i.e., keeping only the first-order terms in

(4.6)—for the characteristic equation (4.5), it turns out that the $O(m)$ terms in (4.5) balance only if $z_0 = \alpha_l$, where $-\alpha_l$, $l = 1, 2, \ldots$, are the roots of Ai. With this selection, Ai, Ai$'$ appearing in (4.6) are expanded in Maclaurin series as

$$
\mathrm{Ai}(-2^{1/2}z_l) \underset{m\to\infty}{\sim} c_1 \mathrm{Ai}'(-\alpha_l)\frac{1}{m^{1/3}} + c_2 \mathrm{Ai}'(-\alpha_l)\frac{1}{m^{2/3}}
$$
$$
+ \left[c_3 \mathrm{Ai}'(-\alpha_l) - \frac{1}{6}c_1^3\alpha_l \mathrm{Ai}'(-\alpha_l) \right]\frac{1}{m},
$$
$$
\mathrm{Ai}'(-2^{1/2}z_l) \underset{m\to\infty}{\sim} \mathrm{Ai}'(-\alpha_l) - \frac{1}{2}c_1^2\alpha_l \mathrm{Ai}'(-\alpha_l)\frac{1}{m^{2/3}}
$$
$$
+ \left[\frac{1}{3}c_1^3 \mathrm{Ai}'(-\alpha_l) - c_1 c_2 \alpha_l \mathrm{Ai}'(-\alpha_l) \right]\frac{1}{m}. \tag{4.8}
$$

To obtain (4.8), the properties $\mathrm{Ai}''(\xi) = \xi\mathrm{Ai}(\xi)$ and $\mathrm{Ai}'''(\xi) = \mathrm{Ai}(\xi) + \xi\mathrm{Ai}'(\xi)$ have been used, where the double and triple prime denote second- and third-order derivatives with respect to the argument.

Substituting the expansions (4.6)–(4.8) into (4.5), we obtain the expansion given by (4.9), shown below.

$$
-\frac{2^{1/3}\epsilon_\perp}{c_1}m + \frac{(2^{2/3}3\alpha_l^2 + 20c_2)\epsilon_\perp}{2^{2/3}10c_1^2}m^{2/3}
$$
$$
-\frac{(2^{2/3}27\alpha_l^4 + 600\alpha_l c_1^2 - 2^{1/3}200\alpha_l c_1^4 + 360\alpha_l^2 c_2 + 2^{1/3}600c_2^2 - 2^{1/3}600c_1 c_3)\epsilon_\perp}{600c_1^3}m^{1/3}
$$
$$
+ O(1) = (\epsilon_x - \sqrt{1-\epsilon_\perp})m + \frac{\alpha_l\epsilon_\perp}{2^{1/3}\sqrt{1-\epsilon_\perp}}m^{1/3} + O(1). \tag{4.9}
$$

Equating the orders in (4.9), we determine c_1, c_2, and c_3 in closed-form by:

$$
c_1 = \frac{2^{1/3}\epsilon_\perp}{\sqrt{1-\epsilon_\perp} - \epsilon_x},
$$
$$
c_2 = -\frac{2^{2/3}3\alpha_l^2}{20} \equiv c_{2,l},
$$
$$
c_3 = \frac{c_1^2}{2^{1/3}}\left(\frac{\alpha_l}{2^{1/3}\sqrt{1-\epsilon_\perp}} + \frac{2^{2/3}9\alpha_l^4}{200}\frac{1}{c_1^3} + \alpha_l\frac{1}{c_1} - \frac{2^{1/3}\alpha_l}{3}c_1 \right.
$$
$$
\left. + \frac{3\alpha_l^2}{5}\frac{c_{2,l}}{c_1^3} + 2^{1/3}\frac{c_{2,l}^2}{c_1^3} \right) \equiv c_{3,l}. \tag{4.10}
$$

Since $u_l/\sqrt{\epsilon_\perp} = m + z_l m^{1/3}$ and $z_l \sim 2^{-1/3}(\alpha_l - \sum_{j=1}^3 c_j\, m^{-j/3})$, $m \to \infty$, u_l is given, up to $O(m^{-2/3})$, by the closed-form expression

$$
u_l \underset{m\to\infty}{\sim} \sqrt{\epsilon_\perp}\Big(m + 2^{-1/3}\alpha_l m^{1/3} - 2^{-1/3}c_1
$$
$$
- 2^{-1/3}c_{2,l}\frac{1}{m^{1/3}} - 2^{-1/3}c_{3,l}\frac{1}{m^{2/3}} \Big). \tag{4.11}
$$

By the properties $Z_{-|m|}(\xi) = (-1)^{|m|}Z_{|m|}(\xi)$, $Z \equiv J, H$, it is concluded that for $m < 0$, u_l is again given by (4.11) but now m is replaced by $|m|$, while ϵ_x in c_1 of (4.10) is replaced by $-\epsilon_x$.

Asymptotic expansion for the imaginary part The asymptotic expansion for v is derived by first defining the characteristic equation (4.4) for TE modes as a complex-valued function $F(x) = \epsilon_x m + x H'_m(x)/H_m(x) - \epsilon_\perp/\sqrt{\epsilon_\perp}\, x J'_m(x/\sqrt{\epsilon_\perp})/J_m(x/\sqrt{\epsilon_\perp})$. Then, if $u + iv$ is a complex root of $F(x)$, we expand it in Taylor series around $u + iv$ as $F(x) \sim [x - (u + iv)][\mathrm{d}F(x)/(\mathrm{d}x)]_{x=u+iv}$, $x \to u + iv$. Using Bessel's differential equation, it can be worked out that

$$\left.\frac{\mathrm{d}F(x)}{\mathrm{d}x}\right|_{x=u+iv} = \frac{1 - \epsilon_\perp - \epsilon_x^2}{u + iv} m^2$$
$$+ \frac{2\epsilon_\perp \epsilon_x}{\sqrt{\epsilon_\perp}} \frac{J'_m((u+iv)/\sqrt{\epsilon_\perp})}{J_m((u+iv)/\sqrt{\epsilon_\perp})} m$$
$$- (u+iv)(\epsilon_\perp - 1)\left[\frac{J'_m((u+iv)/\sqrt{\epsilon_\perp})}{J_m((u+iv)/\sqrt{\epsilon_\perp})}\right]^2. \tag{4.12}$$

Keeping the dominant $O(m^2)$ term and neglecting the $O(m)$ and $O(1)$ terms in (4.12), we may evaluate $\mathrm{Im}\{F(x)\}$ at $x = u$, from its second-order Taylor expansion, as

$$\mathrm{Im}\{F(u)\} \underset{x \to u+iv}{\sim} -\frac{uv}{u^2 + v^2}(1 - \epsilon_\perp - \epsilon_x^2)m^2. \tag{4.13}$$

Since WGMs' x obey $u \gg v$, v^2 in the denominator of (4.13) can be neglected. Then, equating (4.13) with $\mathrm{Im}\{F(u)\} \approx -2/[\pi Y_m^2(u)]$—as obtained from the analysis of Section 4.2.1—finally yields

$$v_l = \frac{2u_l}{\pi(1 - \epsilon_\perp - \epsilon_x^2)Y_m^2(u_l)} \frac{1}{m^2}. \tag{4.14}$$

For $m < 0$, v_l is again given by (4.14) but now m is replaced by $|m|$ and u_l are given by the modified expressions for $m < 0$, as explained above.

4.2.3   Asymptotic solution for TM modes

The derivation of the asymptotic closed-form expressions for the complex x of TM modes, requires a simplified procedure, as compared to the one followed in Section 4.2.2. In particular, concerning the real part u, the large-m characteristic equation is now given by $\sqrt{\epsilon_{3r}} J'_m(u\sqrt{\epsilon_{3r}})/J_m(u\sqrt{\epsilon_{3r}}) = Y'_m(u)/Y_m(u)$. This form is similar to the large-m characteristic equation for TE modes of isotropic spherical resonators, as given in [142, eq. (2.1b)], with the difference that the order of Bessel and Neumann functions in [142] is fractional. In the present case, $u\sqrt{\epsilon_{3r}} > m$ and $u < m$. Therefore, setting $u\sqrt{\epsilon_{3r}} = m + zm^{1/3}$, $u = m\,\mathrm{sech}\,\alpha$, and employing the same expansion for z_l as in Section 4.2.2, as well as the expansions (4.6)–(4.8), and upon substitution into the above mentioned characteristic equation for TM modes, we may determine the unknown expansion coefficients c_1 and $c_{3,l}$ by

$$c_1 = \frac{2^{1/3}\sqrt{\epsilon_{3r}}}{\sqrt{\epsilon_{3r} - 1}},$$
$$c_{3,l} = \frac{c_1^2}{2^{1/3}}\left(\frac{\alpha_l \sqrt{\epsilon_{3r}}}{2^{1/3}\sqrt{\epsilon_{3r} - 1}} + \frac{9\alpha_l^4}{2^{1/3}100}\frac{1}{c_1^3} - \frac{2^{1/3}\alpha_l}{3}c_1\right.$$
$$\left. + \frac{3\alpha_l^2}{5}\frac{c_{2,l}}{c_1^3} + 2^{1/3}\frac{c_{2,l}^2}{c_1^3}\right), \tag{4.15}$$

while $c_{2,l}$ is the same with $c_{2,l}$ of (4.10) for TE modes. Then, u_l is again asymptotically expanded, up to $O(m^{-2/3})$, by (4.11), with the difference that $\sqrt{\epsilon_\perp}$ in (4.11) is replaced by $1/\sqrt{\epsilon_{3r}}$.

Regarding the asymptotic expansion of the imaginary part v, following the analysis of Section 4.2.2, we in sequence obtain $[\mathrm{d}F(x)/(\mathrm{d}x)]_{x=u+iv} = \epsilon_{3r} - 1$, $\mathrm{Im}\{F(u)\} \sim -v(\epsilon_{3r} - 1)$, $x \to u + iv$, and finally

$$v_l = \frac{2}{\pi(\epsilon_{3r} - 1)u_l Y_m^2(u_l)}. \tag{4.16}$$

In the case of TM modes, x_l degenerate for $\pm|m|$. Therefore, the results of this Subsection do not alter for $m < 0$.

4.3   Inhomogeneous gyroelectric resonators

4.3.1   VIE-based characteristic equations

For inhomogeneous gyroelectric resonators, the complex normalized wavenumbers x_l are derived through a VIE in absence of external excitation, given by [119]

$$\mathbf{E}(\boldsymbol{\rho}) = \left(k_0^2\mathbb{I} + \nabla\nabla^T\right)\int_{\boldsymbol{\rho}'\in S} g(\boldsymbol{\rho},\boldsymbol{\rho}')\mathbb{X}_{\mathrm{e}}(\boldsymbol{\rho}')\mathbf{E}(\boldsymbol{\rho}')\mathrm{d}\boldsymbol{\rho}'. \tag{4.17}$$

In (4.17), $\mathbf{E}(\boldsymbol{\rho})$ is the total electric field, $\boldsymbol{\rho}$ is the position vector in the polar coordinate system, $\mathbb{I}$ is the unity dyadic, T denotes transposition, $S = \{(\rho,\varphi) \in \mathbb{R}^2 | \rho \in [0,a], \varphi \in [0,2\pi)\}$ is the cross-sectional domain of the circular cylinder, $g(\boldsymbol{\rho},\boldsymbol{\rho}')$ is the two-dimensional free space Green's function, and $\mathbb{X}_{\mathrm{e}}(\rho) = \boldsymbol{\epsilon}(\rho)/\epsilon_0 - \mathbb{I}$ is the normalized tensorial electric contrast function. In particular, (4.17) defines two homogeneous systems $\mathbb{A}^{\mathrm{TE}}(x_l)\mathbf{u}_l = 0$ and $\mathbb{A}^{\mathrm{TM}}(x_l)\mathbf{v}_l = 0$—with $\mathbf{u}_l$, $\mathbf{v}_l$, $l = 1, 2, \ldots$, the eigenvectors corresponding to each x_l—where the x_l are determined via the determinantal equations $\det\{\mathbb{A}^{\mathrm{TE,TM}}(x_l)\} = 0$. These determinantal equations are the characteristic equations for TE/TM modes for inhomogeneous gyroelectric resonators. For gyroelectric cylinders studied here, matrix $\mathbb{A}^{\mathrm{TE}}(x_l)$ is composed by [119, eqs (16) and first of (20)], by setting the expansion coefficients A_m^{inc}, Λ_{mp} and T_{mp} appearing in [119, eq. (16)], equal to zero. Similarly, the matrix $\mathbb{A}^{\mathrm{TM}}(x_l)$ is composed by [119, eqs (17) and second of (20)], by setting the expansion coefficients B_m^{inc}, K_{mp} and Σ_{mp} appearing in [119, eq. (17)], equal to zero.

To solve (4.17), $\mathbf{E}(\boldsymbol{\rho})$ is expanded in Dini series as [119]

$$\mathbf{E}(\boldsymbol{\rho}) = \sum_{m=-\infty}^{\infty}\sum_{l=1}^{\infty}\left[\Gamma_{ml}\mathbf{M}_{ml}\left(\frac{\gamma_{ml}^M}{a},\boldsymbol{\rho}\right) + \Delta_{ml}\mathbf{N}_{ml}\left(\frac{\gamma_{ml}^N}{a},\boldsymbol{\rho}\right) + Z_{ml}\mathbf{L}_{ml}\left(\frac{\gamma_{ml}^L}{a},\boldsymbol{\rho}\right)\right], \tag{4.18}$$

where $\mathbf{M}_{ml}$, $\mathbf{N}_{ml}$, $\mathbf{L}_{ml}$ are Dini-type CVWFs [119] and Γ_{ml}, Δ_{ml}, Z_{ml} unknown expansion coefficients. In order for the eigenbasis defined by the $\mathbf{M}_{ml}$, $\mathbf{N}_{ml}$, $\mathbf{L}_{ml}$ vectors to be orthogonal, the sets γ_{ml}^M, γ_{ml}^N, γ_{ml}^L must satisfy certain conditions. In particular, γ_{ml}^M and γ_{ml}^N must be selected as the roots of the eigenequations [119, eqs (A.7) and (A.10)]

$$\frac{1}{\gamma_{ml}^M}\frac{J_m'(\gamma_{ml}^M)}{J_m(\gamma_{ml}^M)} - t_m^M = 0,$$

$$\gamma_{ml}^N\frac{J_m'(\gamma_{ml}^N)}{J_m(\gamma_{ml}^N)} - t_m^N = 0, \tag{4.19}$$

with t_m^M, t_m^N arbitrary complex numbers, while γ_{ml}^L as the roots of [119, eq. (A.13)]. γ_{ml}^L, however, do not appear in the composition of $\mathbb{A}^{\mathrm{TE,TM}}$, therefore they are

ignored in the remaining analysis. It should be noted that (16) and (17) of [119], which are introduced above and contribute in $\mathbb{A}^{\mathrm{TE,TM}}$, stem from the analytical reduction of the original VIE (4.17) by expanding the unknown $\mathbf{E}(\boldsymbol{\rho})$ in Dini series as in (4.18). This means that the two-dimensional volumetric integral in (4.17) is firstly carried out analytically, and the $k_0^2\mathbb{I} + \nabla\nabla^T$ operator is secondly taken into account by utilizing the properties $\nabla^T\mathbf{M}_{ml}(k,\boldsymbol{\rho}) = \nabla^T\mathbf{N}_{ml}(k,\boldsymbol{\rho}) = 0$, $\nabla\nabla^T\mathbf{L}_{ml}(k,\boldsymbol{\rho}) + k^2\mathbf{L}_{ml}(k,\boldsymbol{\rho}) = 0$, $\nabla \times \mathbf{M}_{ml}(k,\boldsymbol{\rho}) = k\mathbf{N}_{ml}(k,\boldsymbol{\rho})$, $\nabla \times \mathbf{N}_{ml}(k,\boldsymbol{\rho}) = k\mathbf{M}_{ml}(k,\boldsymbol{\rho})$, and $\nabla \times \mathbf{L}_{ml}(k,\boldsymbol{\rho}) = 0$ [145], where $k \equiv k_0, \gamma_{ml}^M/a, \gamma_{ml}^N/a, \gamma_{ml}^L/a$. The interested reader is referred to [119] for the details.

Currently, $\gamma_{ml}^{M,N}$ are numerically retrieved via (4.19) by the application of a real-root finding algorithm, by defining $t_m^M, t_m^N \in \mathbb{R}$. To apply (4.17) for the calculation of large order WGM frequencies, however, the computation of the aforementioned real roots for very large m is required, a time consuming and demanding task for any root finding algorithm due to the loss of roots when m is very large. This means that the $\mathbf{M}_{ml}$-, $\mathbf{N}_{ml}$-part of the vectorial eigenbasis is not orthogonal anymore, an undesired situation for the VIE which in sequence does not yield the expected complex roots from $\det\{\mathbb{A}^{\mathrm{TE,TM}}(x_l)\} = 0$. To overpass this obstacle, we apply large-m order expansions in (4.19), which allow for the instant computation of $\gamma_{ml}^{M,N}$ by closed-form expressions, and render the VIE suitable for WGM studies of continuously varying highly inhomogeneous gyroelectric cylindrical resonators.

4.3.2   Asymptotic-based vectorial eigenbasis

Herein we apply large-m order expansions in (4.19) for the determination of $\gamma_{ml}^{M,N}$ by closed-form expressions up to $O(m^{-1})$. It should be clarified that $\gamma_{ml}^{M,N}$ do not need to be complex, therefore the below analysis is restricted to the computation of real roots. In addition, the roots obtained from (4.19) for $m > 0$ are the same when $m < 0$, therefore in what follows we keep $m > 0$. Respective large order expansions were applied in the vectorial eigenbasis of the VIE for WGM lasing in gyroelectric spherical resonators [136]. That eigenbasis involved the computation of the real roots $\gamma_{mn\ell}^M$ [136, see eigenequation (2)] and $\gamma_{mn\ell}^N$ [136, see eigenequation (3)].

We begin with the determination of γ_{ml}^M from the first of (4.19). From Dini theory [119], we know that the first root $\gamma_{m1}^M < m$—but not $\gamma_{m1}^M \ll m$—while higher-order roots satisfy $\gamma_{ml}^M > m$, $l = 2, 3, \ldots$. This instructs us that, for the asymptotic determination of γ_{m1}^M, we must apply Debye's first-order asymptotic expansions for J_m, J_m' [144, entries 9.3.7, 9.3.11], and not the standard asymptotic form [144, entry 9.3.1] and its derivative, which hold when the argument is much lesser than the order, and were used in [136] for the calculation of γ_{mn1}^N of [136, eq. (3)]. Setting $\gamma_{m1}^M = m\,\mathrm{sech}\,\alpha$, $\alpha > 0$, we obtain

$$\frac{J_m'(\gamma_{m1}^M)}{\gamma_{m1}^M J_m(\gamma_{m1}^M)} \underset{m\to\infty}{\sim} \cosh\alpha\sqrt{\cosh^2\alpha - 1}\,\frac{1}{m}. \qquad (4.20)$$

Substituting this result into the first of (4.19), along with $\cosh\alpha = m/\gamma_{m1}^M$, we finally obtain

$$\gamma_{m1}^M \underset{m\to\infty}{\sim} \sqrt{\zeta_m/2},$$

$$\zeta_m \equiv -\frac{1}{(t_m^M)^2} + \frac{1}{t_m^M}\sqrt{\frac{1}{(t_m^M)^2} + (2m)^2}. \qquad (4.21)$$

For the determination of γ_{ml}^M, $l = 2, 3, \ldots$, we note that the first of (4.19) is the same with (13) of [136], without the fractional term $1/[2(\gamma_{mn\ell}^N)^2]$. This fraction,

however, only contributes to the asymptotic expansion in terms with order lower than $O(m^{-1})$. Therefore, the results of Section II.C of [136] for the higher-order roots—and not for the first root—can be adapted to the present problem. For completeness, we report here the final results, i.e.,

$$\gamma_{ml}^{M} \underset{m\to\infty}{\sim} m + 2^{-1/3}\alpha_l m^{1/3} - 2^{-1/3}c_{2,l}\frac{1}{m^{1/3}}$$
$$- 2^{-1/3}c_{4,l}\frac{1}{m}, \quad l = 2, 3, \ldots,$$
$$c_{2,l} = -\frac{3\alpha_l^2}{2^{1/3}10}, \quad c_{4,l} = \frac{7t_m^M/4 - 2^{1/3}5}{350}. \tag{4.22}$$

Next, we proceed with the determination of γ_{ml}^{N} from the second of (4.19). This eigenequation has all of its roots in the region $\gamma_{ml}^{N} > m$, a behavior similar to [136, eq. (4)]. Specifically, we note that the second of (4.19) is the same with (4) of [136] without the $1/2$ term. Following similar steps as in Section II.B of [136], we conclude for the present problem that

$$\gamma_{ml}^{N} \underset{m\to\infty}{\sim} m + 2^{-1/3}\alpha_l' m^{1/3} - 2^{-1/3}c_{2,l}\frac{1}{m^{1/3}}$$
$$- 2^{-1/3}c_{4,l}\frac{1}{m}, \quad l = 1, 2, \ldots,$$
$$c_{2,l} = \frac{10t_m^N + 2 - 3(\alpha_l')^3}{2^{1/3}10\alpha_l'},$$
$$c_{4,l} = [2^{2/3}56\alpha_l' + 2^{2/3}151(\alpha_l')^4 + 1400(\alpha_l')^2 c_{2,l}$$
$$+ 2^{1/3}1400c_{2,l}^2]/(2^{1/3}2800\alpha_l'), \tag{4.23}$$

where $-\alpha_l'$, $l = 1, 2, \ldots$, are the roots of Ai'.

4.4   Numerical results and discussion

Herein we validate the asymptotic closed-form expressions derived in Sections 4.2 and 4.3 and we demonstrate the calculation of very high order WGM frequencies for cylindrical resonators composed of homogeneous and continuously varying highly inhomogeneous permittivity profiles. In particular, we compare the complex WGM frequencies for homogeneous gyroelectric resonators, for both TE/TM modes, utilizing three different methods. The first method relies on the calculation of x by the asymptotic expressions (4.11), (4.14), and (4.16). In the second method the x are numerically retrieved by VIE's determinantal equations, using the asymptotic-based vectorial eigenbasis constructed via (4.21)–(4.23). Finally, in the third method, the x are extracted from the numerical solution of the characteristic equations (4.4) using complex root finding techniques.

To implement the above comparison, however, we first need to validate the asymptotics (4.21)–(4.23) that will ensure a proper large-m orthogonal vectorial eigenbasis for the accurate solution of the VIE. In Table 4.1 we demonstrate the correctness of (4.21)–(4.23), by computing the first ten sequential roots γ_{ml}^{M}, γ_{ml}^{N}, for $m = 100$ and $m = 1000$. The numerical evaluation of the roots, as given in Table 4.1, is based on the numerical solution of (4.19). Since γ_{ml}^{M}, γ_{ml}^{N} are real numbers, these equations are solved using Brent's real root finding technique [146]. The agreement between the asymptotic and numerical solution is evident, especially when $m = 1000$. Concerning the first root γ_{m1}^{M}, in particular, it satisfies the

Table 4.1 γ_{ml}^M and γ_{ml}^N using $t_m^M = 0.2$ and $t_m^N = -0.2$. Top: $m = 100$; bottom: $m = 1000$.

	γ_{ml}^M		γ_{ml}^N	
l	Asymptotic	Numerical	Asymptotic	Numerical
1	22.082940	22.085739	103.79531	103.79531
2	108.83638	108.88207	112.39536	112.39521
3	115.74069	115.78252	118.70157	118.70086
4	121.57894	121.61643	124.24894	124.24707
5	126.87795	126.91014	129.36630	129.36253
6	131.83615	131.86184	134.19670	134.19016
7	136.55450	136.57232	138.81843	138.80815
8	141.09286	141.10127	143.28001	143.26494
9	145.49019	145.48757	147.61408	147.59305
10	149.77358	149.75818	151.84380	151.81559
	γ_{ml}^M		γ_{ml}^N	
l	Asymptotic	Numerical	Asymptotic	Numerical
1	70.622345	——	1008.1058	1008.1058
2	1018.6609	1018.6658	1025.9803	1025.9803
3	1032.7619	1032.7667	1038.6961	1038.6960
4	1044.3927	1044.3972	1049.6357	1049.6357
5	1054.7366	1054.7409	1059.5395	1059.5395
6	1064.2453	1064.2492	1068.7340	1068.7339
7	1073.1514	1073.1548	1077.4000	1077.3998
8	1081.5940	1081.5969	1085.6510	1085.6506
9	1089.6650	1089.6673	1093.5639	1093.5634
10	1097.4287	1097.4303	1101.1942	1101.1935

condition $\gamma_{m1}^M < m$, while its agreement with the numerical solution of the first of (4.19) successfully establishes the validity of the closed-form expression (4.21). The efficiency of the asymptotic calculation is superior than that of the numerical extraction on (4.19). For instance, the numerical calculation of all γ_{ml}^M, γ_{ml}^N roots appearing in Table 4.1/bottom, requires 41 s of CPU time on a 2.1 GHz double octa-core equipped machine, when increasing the points by 0.002 each time in the incremental step algorithm, to detect the change of sign. In case of a finer incremental step, say 0.001, 94 s of CPU time are needed. Yet, this inefficient calculation must be repeated for different values of m. Contrariwise, the asymptotic calculation is instant for every value of m. It should be emphasized that, when m acquires large values, the numerical root extraction procedure in the first of (4.19) is prone to lose roots. This is depicted in Table 4.1/bottom where γ_{m1}^M is missing from eigenequation's root sequence. To locate this root, we have used small steps to detect a change of sign on the real axis, by incrementally increasing the points by 0.001 each time, yet unsuccessfully. The absence of this root constitutes the vectorial eigenbasis non-orthogonal and as a consequence the VIE does not yield the expected complex roots for TE modes. On the contrary, the asymptotic calculation does not lose roots and ensures the proper extraction of complex x via the VIE.

  Having established the validity for the large-m vectorial eigenbasis, we proceed to the comparison of the x for homogeneous isotropic resonators. In Table 4.2 we establish the validity of the asymptotic closed-form expressions (4.11) and (4.14) for TE modes using $m = 50$ and $m = 200$, as well as of the asymptotic-based VIE by the numerical solution of determinantal equation $\det\{\mathbb{A}^{TE}(x_l)\} = 0$, via a

Table 4.2   Complex x for TE_{ml} modes of homogeneous isotropic resonator with $\epsilon_{1r} = 2.54$ and $\epsilon_{2r} = 0$. Top: $m = 50$; bottom: $m = 200$.

l	Asymptotic	VIE	SVM
1	$35.457 + 2.6813 \cdot 10^{-08}i$	$35.485 + 9.5654 \cdot 10^{-09}i$	$35.446 + 1.1786 \cdot 10^{-08}i$
2	$38.981 + 1.4487 \cdot 10^{-05}i$	$38.988 + 6.7080 \cdot 10^{-06}i$	$38.938 + 6.9445 \cdot 10^{-06}i$
3	$42.014 + 1.0649 \cdot 10^{-03}i$	$41.973 + 5.5020 \cdot 10^{-04}i$	$41.912 + 5.5947 \cdot 10^{-04}i$
4	$44.803 + 2.1013 \cdot 10^{-02}i$	$44.661 + 1.2869 \cdot 10^{-02}i$	$44.599 + 1.2482 \cdot 10^{-02}i$
5	$47.444 + 1.3539 \cdot 10^{-01}i$	$47.117 + 1.0360 \cdot 10^{-01}i$	$47.080 + 9.3302 \cdot 10^{-02}i$

l	Asymptotic	VIE	SVM
1	$132.07 + 9.2091 \cdot 10^{-40}i$	$132.09 + 4.0478 \cdot 10^{-09}i$	$132.07 + 2.6039 \cdot 10^{-15}i$
2	$137.37 + 1.0558 \cdot 10^{-34}i$	$137.40 + 3.9315 \cdot 10^{-09}i$	$137.37 + 8.6932 \cdot 10^{-15}i$
3	$141.81 + 9.4989 \cdot 10^{-31}i$	$141.84 + 1.5809 \cdot 10^{-11}i$	$141.80 + 8.5444 \cdot 10^{-15}i$
4	$145.80 + 2.1202 \cdot 10^{-27}i$	$145.83 + 3.9246 \cdot 10^{-09}i$	$145.78 + 1.1747 \cdot 10^{-14}i$
5	$149.50 + 1.8347 \cdot 10^{-24}i$	$149.53 + 4.7578 \cdot 10^{-09}i$	$149.48 + 3.6666 \cdot 10^{-14}i$

global complex root finding algorithm [147]. Both methods are compared vs SVM, whose x are obtained from the numerical solution of the first of (4.4) using Müller's complex root finding method [148]. In addition, Table 4.3 shows the validity of the asymptotic closed-form expressions (4.11) and (4.16) for TM modes, as well as of the asymptotic-based VIE by the numerical solution of $\det\{\mathbb{A}^{TM}(x_l)\} = 0$. Both cases are compared vs SVM, by the numerical solution of the second of (4.4). As it is evident from x depicted in Tables 4.2, 4.3, for the lower order case of $m = 50$, the asymptotic and VIE solutions yield accurate results for $\text{Re}\{x\}$ up to three significant figures, as compared to the SVM solution. For $m = 200$, the accuracy increases up to five significant figures for the asymptotic solution and up to four significant figures for VIE. All in all, the application of the asymptotic formulas may be appreciated by the fact that a systematic application of Müller's method on (4.4) would lead to loss of roots. In addition, the $\text{Im}\{x\}$ for large-m has extremely small values, yet it decreases as m increases, a typical behavior of high-Q WGMs. This is evident from both Tables 4.2, 4.3. It should be clarified, however, that the agreement of $\text{Im}\{x\}$ for the asymptotic solution, as compared to the SVM, is better for TM modes, than that for TE modes. For example, $\text{Im}\{x_1\} = 8.1230 \cdot 10^{-9}$/asymptotic for $TM_{50,1}$ of Table 4.3 meets one significant digit with $\text{Im}\{x_1\} = 8.0526 \cdot 10^{-9}$/SVM. On the contrary, $\text{Im}\{x_1\} = 2.6813 \cdot 10^{-8}$/asymptotic for $TE_{50,1}$ of Table 4.2 is of the same order and very close to $\text{Im}\{x_1\} = 1.1786 \cdot 10^{-8}$/SVM. The better agreement for TM modes is due to the fact that the term $[\mathrm{d}F(x)/(\mathrm{d}x)]_{x=u+iv}$ in Taylor series expansion of $F(x)$ for TM modes, is calculated exactly and given by $\epsilon_{3r} - 1$—see Section 4.2.3. Instead, this term for TE modes is given exactly by (4.12), but only the dominant $O(m^2)$ term is used in the closed-form determination of $\text{Im}\{x\}$. Another issue concerning the $\text{Im}\{x\}$ that needs clarification, for both TE/TM modes, is that, as m acquires very large values, as for instance $m = 200$ in Tables 4.2/bottom, 4.3/bottom, $\text{Im}\{x\}$ is almost nil. The very small order of $\text{Im}\{x\}$ in the asymptotic solution, as for instance 10^{-40} for $\text{Im}\{x_1\}$ in Tables 4.2/bottom, 4.3/bottom, is due to the presence of $Y_m^2(u_l)$ in the denominators of (4.14), (4.16). However, one should expect an exponential decrease with m for the $\text{Im}\{x\}$, as was deduced in [149].

In addition, we note that the respective 10^{-9} and 10^{-15} orders of VIE and SVM, are due to the stop criteria used in the complex root finding algorithms [147, 148]. Overall, the asymptotic calculation of $\text{Im}\{x\}$ for both TE/TM modes is acceptable, if one considers the very low values of $\text{Im}\{x\}$. Moreover, WGM

Table 4.3 Complex x for TM_{ml} modes of homogeneous isotropic resonator with $\epsilon_{3r} = 2.54$. Top: $m = 50$; bottom: $m = 200$.

l	Asymptotic	VIE	SVM
1	$34.972+8.1230\cdot10^{-09}i$	$34.973+8.2695\cdot10^{-09}i$	$34.968+8.0526\cdot10^{-09}i$
2	$38.499+4.4156\cdot10^{-06}i$	$38.487+4.3718\cdot10^{-06}i$	$38.483+4.3029\cdot10^{-06}i$
3	$41.533+3.2997\cdot10^{-04}i$	$41.499+3.2012\cdot10^{-04}i$	$41.496+3.1463\cdot10^{-04}i$
4	$44.325+6.7882\cdot10^{-03}i$	$44.250+6.4242\cdot10^{-03}i$	$44.248+6.3240\cdot10^{-03}i$
5	$46.968+4.6067\cdot10^{-02}i$	$46.834+4.2802\cdot10^{-02}i$	$46.833+4.2302\cdot10^{-02}i$
l	Asymptotic	VIE	SVM
1	$131.58+2.7537\cdot10^{-40}i$	$131.62+4.9860\cdot10^{-09}i$	$131.58+2.3019\cdot10^{-15}i$
2	$136.89+3.1600\cdot10^{-35}i$	$136.92+4.9941\cdot10^{-09}i$	$136.89+4.7817\cdot10^{-16}i$
3	$141.32+2.8439\cdot10^{-31}i$	$141.35+7.2236\cdot10^{-10}i$	$141.32+3.4965\cdot10^{-14}i$
4	$145.32+6.3485\cdot10^{-28}i$	$145.34+5.6127\cdot10^{-09}i$	$145.31+1.1389\cdot10^{-14}i$
5	$149.02+5.4951\cdot10^{-25}i$	$149.03+8.3052\cdot10^{-10}i$	$149.01+9.2869\cdot10^{-14}i$

Table 4.4 Complex x for TE_{ml} modes of homogeneous gyroelectric resonator with $\epsilon_{1r} = 2.54$ and $\epsilon_{2r} = 0.5$. From top to bottom: first subtable: $m = 50$; second subtable: $m = -50$; third subtable: $m = 200$; fourth subtable: $m = -200$.

l	Asymptotic	VIE	SVM
1	$36.092+9.6058\cdot10^{-08}i$	$36.083+4.9076\cdot10^{-08}i$	$36.078+5.4208\cdot10^{-08}i$
2	$39.676+4.4115\cdot10^{-05}i$	$39.626+2.6596\cdot10^{-05}i$	$39.617+2.6868\cdot10^{-05}i$
3	$42.760+2.7042\cdot10^{-03}i$	$42.635+1.7514\cdot10^{-03}i$	$42.621+1.7715\cdot10^{-03}i$
4	$45.597+4.2135\cdot10^{-02}i$	$45.336+2.9926\cdot10^{-02}i$	$45.313+3.0196\cdot10^{-02}i$
5	$48.283+2.1574\cdot10^{-01}i$	$47.843+1.6370\cdot10^{-01}i$	$47.811+1.6376\cdot10^{-01}i$
l	Asymptotic	VIE	SVM
1	$36.183+1.1413\cdot10^{-07}i$	$36.175+3.7090\cdot10^{-08}i$	$36.172+4.2435\cdot10^{-08}i$
2	$39.780+5.1577\cdot10^{-05}i$	$39.742+2.0848\cdot10^{-05}i$	$39.736+2.1109\cdot10^{-05}i$
3	$42.875+3.0849\cdot10^{-03}i$	$42.780+1.3880\cdot10^{-03}i$	$42.770+1.4109\cdot10^{-03}i$
4	$45.722+4.6351\cdot10^{-02}i$	$45.522+2.4461\cdot10^{-02}i$	$45.505+2.4941\cdot10^{-02}i$
5	$48.417+2.3002\cdot10^{-01}i$	$48.078+1.4050\cdot10^{-01}i$	$48.051+1.4344\cdot10^{-01}i$
l	Asymptotic	VIE	SVM
1	$134.64+3.0164\cdot10^{-37}i$	$134.67+8.4212\cdot10^{-10}i$	$134.64+5.0032\cdot10^{-15}i$
2	$140.05+2.8368\cdot10^{-32}i$	$140.08+4.5380\cdot10^{-09}i$	$140.04+6.3572\cdot10^{-15}i$
3	$144.57+2.1388\cdot10^{-28}i$	$144.60+2.7793\cdot10^{-10}i$	$144.56+1.6153\cdot10^{-15}i$
4	$148.63+4.0329\cdot10^{-25}i$	$148.67+5.0011\cdot10^{-09}i$	$148.61+2.7561\cdot10^{-14}i$
5	$152.41+2.9571\cdot10^{-22}i$	$152.44+3.0343\cdot10^{-09}i$	$152.38+3.8419\cdot10^{-14}i$
l	Asymptotic	VIE	SVM
1	$134.72+3.5922\cdot10^{-37}i$	$134.74+4.9384\cdot10^{-09}i$	$134.72+3.8712\cdot10^{-15}i$
2	$140.13+3.3725\cdot10^{-32}i$	$140.16+4.9978\cdot10^{-09}i$	$140.13+4.6659\cdot10^{-15}i$
3	$144.66+2.5363\cdot10^{-28}i$	$144.69+3.4807\cdot10^{-10}i$	$144.65+2.3624\cdot10^{-14}i$
4	$148.73+4.7679\cdot10^{-25}i$	$148.76+5.6833\cdot10^{-09}i$	$148.71+5.4930\cdot10^{-14}i$
5	$152.51+3.4837\cdot10^{-22}i$	$152.53+7.3131\cdot10^{-10}i$	$152.48+1.8881\cdot10^{-14}i$

applications such as lasing, refractometric sensing and magneto-optic coupling, are focused on the positions of the more accurate $\mathrm{Re}\{x\}$, which in sequence yield the natural frequencies of the resonators.

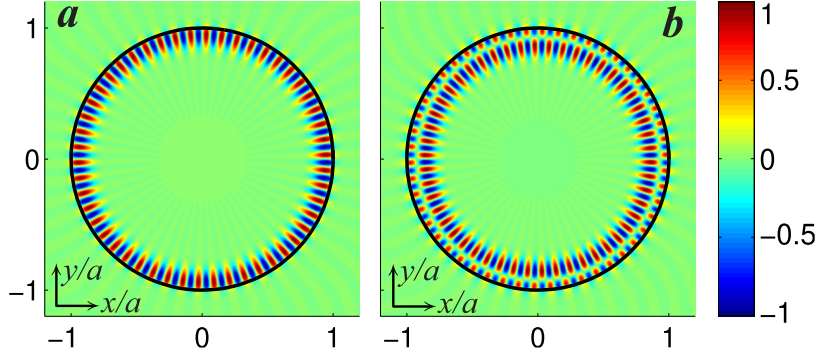In Table 4.4 we show x for TE modes for a homogeneous gyroelectric res-

Figure 4.1 $\mathrm{Re}\{H_z\}/\max\{\mathrm{Re}\{H_z\}\}$ on xy-plane for the first two $\mathrm{TE}_{50,l}$ mode frequencies of the gyroelectric resonator of Table 4.4. (a)$\mathrm{TE}_{50,1}$ (b)$\mathrm{TE}_{50,2}$

onator. Now, due to the lift of m-degeneracy, results for $m \lessgtr 0$ are given, therefore we present frequencies for $m = \pm 50, \pm 200$. Comparing the x of the gyroelectric case with those from the isotropic case for the same value of m—say, for instance, Table 4.4/third and fourth subtables with Table 4.2/bottom—we conclude that the presence of the gyroelectric element ϵ_{2r} splits the original x into two new values. That is, for example, $x_1 = 132.07 + 9.2091 \cdot 10^{-40}i$ of $\mathrm{TE}_{200,1}$ mode/isotropic resonator is split into two frequencies, $x_1 = 134.64 + 3.0164 \cdot 10^{-37}i$ of $\mathrm{TE}_{200,1}$ mode and $x_1 = 134.72 + 3.5922 \cdot 10^{-37}i$ of $\mathrm{TE}_{-200,1}$ mode, with the latter two being frequencies of the gyroelectric resonator. In addition, we note that the x in Table 4.4 for $m = -200$ are slightly greater than the respective ones for $m = 200$. Same observations hold true for $m = \pm 50$. In Figure 4.1 we depict the field pattern of the normalized $\mathrm{Re}\{H_z\}$ for the first two $\mathrm{TE}_{50,l}$ mode frequencies of the gyroelectric resonator of Table 4.4, i.e., for $x_1 = 36.078 + 5.4208 \cdot 10^{-8}i$ and $x_2 = 39.617 + 2.6868 \cdot 10^{-5}i$. As it is indicative for WGM patterns, the $\mathrm{TE}_{50,1}$ mode depicts one localized peak or valley along the radial direction and 50 peaks and 50 valleys along the circumference—see Figure 4.1a. In addition, the $\mathrm{TE}_{50,2}$ mode depicts one localized peak and one localized valley along the radial direction, while the number of peaks/valleys along the circumference does not change—see Figure 4.1b.

Next we demonstrate, by the VIE, the calculation of high and very high order WGMs in resonators composed of a continuously varying highly inhomogeneous permittivity profile. Since the whispering gallery-type localization is based on the principle of quasi-total internal reflection, the refractive index of a homogeneous resonator must be higher than that of the free space background. For inhomogeneous isotropic resonators, one must ensure that $n(\rho = a^-) > 1$, where $n(\rho)$ is the inhomogeneous refractive index of the resonator. To demonstrate the applicability of the VIE for WGM calculations in inhomogeneous resonators, we employ the continuously varying permittivity profile given by $\epsilon_{1r}(\rho) = \epsilon_{3r}(\rho) = \{4/[1 + (\rho/a)^2]\}^2 \equiv \epsilon_r(\rho)$, $0 \leqslant \rho \leqslant a$, while $\epsilon_{2r} = 0$. With this selection, $\epsilon_r(\rho = a^-) = 4 > 1$, thus the above condition is met. In Table 4.5 we give the first WGM frequency x for each mode family, for three different values of m, namely, for high $m = 25$ order, and for very high $m = 100, 200$ orders. From Table 4.5 it is evident that $\mathrm{Re}\{x\}_{\mathrm{TM}} < \mathrm{Re}\{x\}_{\mathrm{TE}}$, for every order m, meaning that the TM frequencies precede the TE ones in the frequency spectrum. In addition, we note the low $\mathrm{Im}\{x\}$ which is indicative of the supported high-Q resonances. In case the above criterion for quasi-total internal reflection is not met, as for instance for a fish-eye lens profile

Table 4.5 Complex x for TM_{m1}, TE_{m1} modes of a continuously varying highly inhomogeneous resonator with $\epsilon_{1r} = \epsilon_{3r} = \{4/[1 + (\rho/a)^2]\}^2$ and $\epsilon_{2r} = 0$.

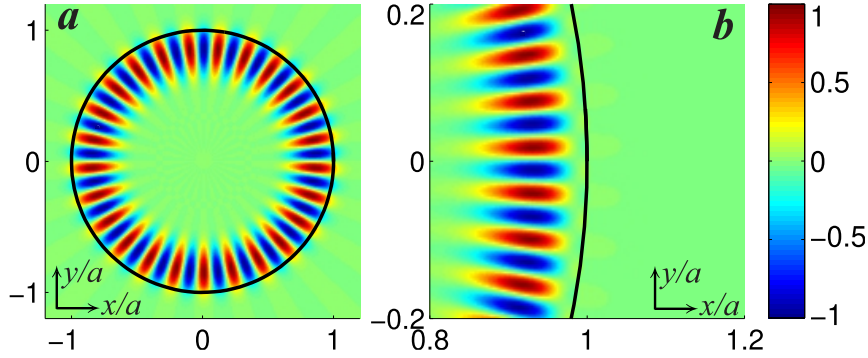| m	l	VIE/TM_{ml}	VIE/TE_{ml}
25	1	$13.129 + 3.3273 \cdot 10^{-09}i$	$13.230 + 9.4892 \cdot 10^{-10}i$
100	1	$50.689 + 3.0646 \cdot 10^{-09}i$	$50.738 + 6.1155 \cdot 10^{-10}i$
200	1	$100.15 + 4.9997 \cdot 10^{-09}i$	$100.74 + 1.3834 \cdot 10^{-09}i$

Figure 4.2 $\text{Re}\{E_z\}/\max\{\text{Re}\{E_z\}\}$ on xy-plane for $\text{TM}_{25,1}$ and $\text{TM}_{100,1}$ WGM frequencies of the continuously varying highly inhomogeneous resonator of Table 4.5. (a)$\text{TM}_{25,1}$ (b)$\text{TM}_{100,1}$

$\epsilon_r(\rho) = \{2/[1 + (\rho/a)^2]\}^2$ where $n(\rho = a^-) = 1$, the respective x in Table 4.5 feature strong imaginary parts, which lead to leaky modes with spatial distribution outside the resonator. In Figure 4.2 we plot the normalized $\text{Re}\{E_z\}$ for the $\text{TM}_{25,1}$ and $\text{TM}_{100,1}$ modes, for the continuously varying profile of Table 4.5. Although the $\text{TM}_{25,1}$ mode depicts 25 peaks and 25 valleys along the circumference—see Figure 4.2a—the $\text{TM}_{100,1}$ mode experiences 100 peaks and valleys, however, in Figure 4.2b we have focused on the area about $x = a$ to clearly visualize the localized resonances.

Finally, in Figure 4.3 we examine how the gyroelectric element ϵ_{2r} affects $\text{Re}\{x\}$, with the latter being a key quantity in magneto-optic coupling applications. In particular, we set equal diagonal elements $\epsilon_{1r} = \epsilon_{3r} \equiv \epsilon_r$ in (4.1), and vary ϵ_{2r} from zero—i.e., an isotropic resonator—up to 3. In Figure 4.3a we plot $\text{Re}\{x_1\}$ of $\text{TE}_{1000,1}$ mode, for various diagonal elements $\epsilon_r = 4.5$, 5.5, and 6.5, using the asymptotic closed-form expression (4.11). From the curves it turns out that $\text{Re}\{x_1\}$ increases as ϵ_{2r} increases, furthermore, $\text{Re}\{x_1\}$ acquires smaller values as the diagonal permittivity elements increase in value. Since this example studies a gyroelectric resonator, $\text{Re}\{x_1\}$ of $\text{TE}_{-1000,1}$ mode have different values than the ones depicted in Figure 4.3a. Nevertheless, the variations of $\text{Re}\{x_1\}$ vs ϵ_{2r} for $m = -1000$ have similar trends as the ones for $m = 1000$, with $\text{Re}\{x_1\}_{m<0} > \text{Re}\{x_1\}_{m>0}$. For this reason, explicit curves for $m = -1000$, as those in Figure 4.3a, are not depicted. To further investigate the split of $\text{Re}\{x_1\}$ due to the lift of degeneration, in Figure 4.3b we plot $\Delta x_1 = |\text{Re}\{x_1\}_{m<0} - \text{Re}\{x_1\}_{m>0}|$ for various orders $|m|$. In particular, we keep fixed the $\epsilon_r = 4.5$, vary ϵ_{2r} from zero up to 3, and repeat this study for $|m| = 100$, 1000, and 10000. Obviously, for the isotropic case, $\Delta x_1 = 0$. However, the split increases as ϵ_{2r} increases, yet, for constant ϵ_{2r}, Δx_1 gets smaller when $|m|$ increases. Notably, the change in Δx_1 is small as $|m|$ jumps from 1000 to 10000.
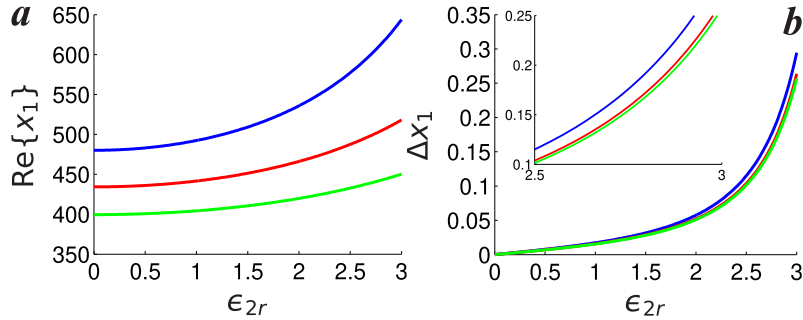
Figure 4.3 Effect of ϵ_{2r} on $\text{Re}\{x_1\}$ and Δx_1 for various gyroelectric resonators. (a)Blue: $\epsilon_r = 4.5$; red: $\epsilon_r = 5.5$; green: $\epsilon_r = 6.5$. In all cases $m = 1000$. (b)Blue: $|m| = 100$; red: $|m| = 1000$; green: $|m| = 10000$. In all cases $\epsilon_r = 4.5$. Inset: Same as in b but $\epsilon_{2r} \in [2.5, 3]$.

To better capture this small change, in the inset of Figure 4.3b we have focused on the region $\epsilon_{2r} \in [2.5, 3]$. In conclusion, if one wants to restrict the gap between $\text{Re}\{x_1\}_{m<0}$ and $\text{Re}\{x_1\}_{m>0}$ when $\epsilon_{2r} \neq 0$, the use of extremely large order modes is necessary, contrariwise, low order modes are requisite for a notable separation.

4.5   Conclusion

We derived asymptotic closed-form expressions for the calculation of the complex WGM frequencies in homogeneous and inhomogeneous gyroelectric cylindrical resonators. For homogeneous resonators, we applied asymptotic expansions on the exact characteristic equations of TE/TM modes. In addition, for inhomogeneous resonators, we extended a VIE by asymptotically expanding its vectorial eigenbasis to support the prediction of large order WGM frequencies. We validated the complex frequencies obtained from the asymptotic closed-form expressions, as well as from the VIE, for the case of a homogeneous gyroelectric resonator, by comparisons with the complex roots extracted by the numerical solution of the TE/TM characteristic equations. We demonstrated the calculation of high and very high order WGMs for a continuously varying highly inhomogeneous permittivity profile. Overall, the developed asymptotic theory constitutes a rigorous tool which may serve for verification of MAR-based numerical solutions for other non-circular inhomogeneous cylinders, as well as for the interpretation of experimental data for applications such as WGM lasing, refractometric sensing, and magneto-optic coupling.

Bibliography

[1] C. Liu, Y. X. Guo, and S. Xiao, "A review of implantable antennas for wireless biomedical devices," in *Forum for electromagnetic research methods and application technologies (FERMAT)*, pp. 1–11, 2016.

[2] K. Psathas, A. Kiourti, and K. Nikita, "Biocompatibility of implantable antennas: Design and performance considerations," in *The 8th European Conference on Antennas and Propagation (EuCAP 2014)*, (Hague), pp. 1566–1570, 2014.

[3] A. Kiourti and K. S. Nikita, "A review of in-body biotelemetry devices: Implantables, ingestibles, and injectables," *IEEE Transactions on Biomedical Engineering*, vol. 64, pp. 1422–1430, 2017.

[4] E. Y. Chow, M. M. Morris, and P. P. Irazoqui, "Implantable rf medical devices: The benefits of high-speed communication and much greater communication distances in biomedical applications," *IEEE Microwave Magazine*, vol. 14, pp. 64–73, 2013.

[5] R. Warty, M. R. Tofighi, U. Kawoos, and A. Rosen, "Characterization of implantable antennas for intracranial pressure monitoring: Reflection by and transmission through a scalp phantom," *IEEE Transactions on Microwave Theory and Techniques*, vol. 56, pp. 2366–2376, 2008.

[6] K. E. Toghill and R. G. Compton, "Electrochemical nonenzymatic glucose sensors: a perspective and an evaluation," *International journal of electrochemical science*, vol. 5, pp. 1246–1301, 2010.

[7] M. Allen, "Pacemaker and implantable cardioverter defibrillators," *Anaesthesia*, vol. 61, pp. 883–890, 2006.

[8] M. D. Weiss, J. L. Smith, and J. Bach, "Rf coupling in a 433 mhz biotelemetry system for an artificial hip," *IEEE Antennas and Wireless Propagation Letters*,

vol. 8, pp. 916–919, 2009.

[9] R. A. Gaunt and A. Prochazka, "Control of urinary bladder function with devices: successes and failures," *Progress in brain research*, vol. 152, pp. 163–194, 2006.

[10] S. Klauke, M. Goertz, S. Rein, D. Hoehl, U. Thomas, R. Eckhorn, F. Bremmer, and T. Wachtler, "Stimulation with a wireless intraocular epiretinal implant elicits visual percepts in blind humans," *Investigative Ophthalmology and Visual Science*, vol. 52, pp. 449–455, 2011.

[11] M. R. Yuce and T. Dissanayake, "Easy-to-swallow wireless telemetry," *IEEE Microwave magazine*, vol. 13, pp. 90–101, 2012.

[12] X. Li, W. A. Serdijn, W. Zheng, Y. Tian, and B. Zhang, "The injectable neurostimulator: an emerging therapeutic device," *Trends in biotechnology*, vol. 33, pp. 388–394, 2015.

[13] P. Valdastri, A. Menciassi, A. Arena, C. Caccamo, and P. Dario, "An implantable telemetry platform system for in vivo monitoring of physiological parameters," *IEEE Transactions on Information Technology in Biomedicine*, vol. 8, p. 271278, 2004.

[14] "European radiocommunications commission (erc), erc recommendation 7003 relating to the use of short range devices. in proceedings of the european conference of postal and telecommunications administration, cept/erc 7003, annex 12., 1997.,"

[15] "Federal communications commission (fcc), medical implant communications service (mics) federal register. rules regulation, 64(240): 6992669934., 1999.,"

[16] T. Karacolak, A. Z. Aaron, and E. Topsakal, "Design of a dual-band implantable antenna and development of skin mimicking gels for continuous glucose monitoring," *IEEE Transactions on Microwave Theory and Techniques*, vol. 56, pp. 1001–1008, 2008.

[17] P. Soontornpipit, C. M. Furse, and Y. C. Chung, "Design of implantable microstrip antenna for communication with medical implants," *IEEE Transactions on Microwave Theory and Techniques*, vol. 52, pp. 1944–1951, 2004.

[18] T. Karacolak, R. Cooper, J. Butler, S. Fisher, and E. Topsakal, "In vivo verification of implantable antennas using rats as model animals," *IEEE Antennas and Wireless Propagation Letters*, vol. 9, pp. 334–337, 2010.

[19] J. Abadia, F. Merli, J. F. Zurcher, J. R. Mosig, and A. K. Skrivervik, "3d-spiral small antenna design and realization for biomedical telemetry in the mics band," *Radioengineering*, vol. 18, pp. 359–367, 2009.

[20] K. Ide, S. Ijiguchi, and T. Fukusako, "Gain enhancement of low-profile, electrically small capacitive feed antennas using stacked meander lines," *International Journal of Antennas and Propagation*, vol. 2010, pp. 1–9, 2010.

[21] K. Jaehoon and Y. Rahmat-Samii, "Sar reduction of implanted planar inverted f antennas with non-uniform width radiator," in *2006 IEEE Antennas and Propagation Society International Symposium*, pp. 1091–1094, 2006.

[22] W. C. Liu, S. H. Chen, and C. M. Wu, "Implantable broadband circular stacked pifa antenna for biotelemetry communication," *Journal of Electromagnetic Waves and Applications*, vol. 22, pp. 1791–1800, 2008.

[23] A. A. Amor, P. Padilla, J. M. Fernandez, and M. S. Castaner, "A miniaturized ultrawidebandarchimedean spiral antennafor low-power sensorapplications in energyharvesting," *Microw Opt Technol Lett.*, vol. 61, pp. 211–216, 2019.

[24] S. A. R. Parizi, "Bandwidth enhancement techniques," pp. 1–36, 2017.

[25] N. G. Kwan, "Non-ionizing radiations–sources, biological effects, emissions and exposures," in *Proceedings of the international conference on non-ionizing radiation at UNITEN*, pp. 1–16, 2003.

[26] R. Buckus, B. Strukcinskiene, J. Raistenskis, and R. Stukas, "Modelling and assessment of the electric field strength caused by mobile phone to the human head," *VOJNOSANITETSKI PREGLED*, vol. 74, pp. 538–543, 2016.

[27] Z. Tang, B. Smith, J. H. Schild, and P. H. Peckham, "Data transmission from an implantable biotelemeter by load-shift keying using circuit configuration modulator," *IEEE Transactions on Biomedical Engineering*, vol. 42, pp. 524–528, 1995.

[28] A. Kiourti and K. S. Nikita, "A review of implantable patch antennas for biomedical telemetry: Challenges and solutions," *IEEE Antennas and Propagation Magazine*, vol. 54, pp. 210–228, 2012.

[29] A. Peyman, C. Gabriel, E. H. Grant, G. Vermeeren, and L. Martens, "Variation of the dielectric properties of tissues with age: the effect on the values of sar in children when exposed to walkie-talkie devices," *Physics in Medicine and Biology,*, vol. 54, pp. 227–241, 2009.

[30] X. Y. Liu, Z. T. Wu, Y. Fan, and E. M. Tentzeris, "A miniaturized csrr loaded wide-beamwidth circularly polarized implantable antenna for subcutaneous real-time glucose monitoring," *IEEE Antennas and Wireless Propagation Letters*, vol. 16, pp. 577–580, 2017.

[31] H. Li, Y. X. Guo, C. Liu, S. Xiao, and L. Li, "A miniature-implantable antenna for medradio-band biomedical telemetry," *IEEE Antennas and Wireless Propagation Letters*, vol. 14, pp. 1176–1179, 2015.

[32] "Ansoft high frequency structure simulator (hfss), ver. 11. pittsburgh, pa: Ansoft corporation, 2008.,"

[33] "Institute of electrical and electronics engineers, ieee standard for safety levels with respect to human exposure to radiofrequency electromagnetic fields, 3khz to 300 ghz, ieee standard c95.11999., 1999,"

[34] "Institute of electrical and electronics engineers, ieee standard for safety levels with respect to human, exposure to radiofrequency electromagnetic fields 3khz to 300 ghz, ieee standard c95.12005, 2005.,"

[35] Y. Cho and H. Yoo, "Miniaturised dual-band implantable antenna for wireless biotelemetry," *Electronics Letters*, vol. 52, pp. 1005–1007, 2016.

[36] A. Basir, A. Bouazizi, M. Zada, A. Iqbal, S. Ullah, and U. Naeem, "A dual-band implantable antenna with wide-band characteristics at mics and ism bands," *Microwave and Optical Technology Letters*, vol. 60, pp. 2944–2949, 2018.

[37] X. Zhang, L. Li, X. Zhang, Q. Zhao, and X. Lu, "A dual band implantable antenna," in *2018 International Applied Computational Electromagnetics Society Symposium-China (ACES)*, pp. 1–2, 2018.

[38] Y. Liu, Y. Chen, H. Lin, and F. H. Juwono, "A novel differentially fed compact dual-band implantable antenna for biotelemetry applications," *IEEE Antennas and Wireless Propagation Letters*, vol. 15, pp. 1791–1794, 2016.

[39] A. Kumar, N. Gupta, and P. Gautam, "Gain and bandwidth enhancement techniques in microstrip patch antennas-a review," *International Journal of Computer Applications*, vol. 148, 2016.

[40] A. S. Mekki, M. N. Mohd, A. Ismail, and A. R. H. Alhawari, "Gain enhancement of a microstrip patch antenna using a reflecting layer," *International Journal of Antennas and Propagation*, vol. 2015, 2015.

[41] S. P. Skobelev, "Propagation of electromagnetic waves through an invisible gradient-index lens with negative refractive index," *IEEE Trans. Antennas Propag.*, vol. 67, pp. 2095–2102, 2019.

[42] T. Tyc, H. Chen, A. Danner, and Y. Xu, "Invisible lenses with positive isotropic refractive index," *Phys. Rev. A*, vol. 90, p. 053829, 2014.

[43] M. Q. Liu, C. Y. Zhao, and B. X. Wang, "Active tuning of directional scattering by combining magneto-optical effects and multipolar interferences," *Nanoscale*, vol. 10, pp. 18282–18290, 2018.

[44] W. J. M. Kort-Kamp, F. S. S. Rosa, F. A. Pinheiro, and C. Farina, "Molding the flow of light with a magnetic field: plasmonic cloaking and directional scattering," *J. Opt. Soc. Am. A*, vol. 31, pp. 1969–1976, 2014.

[45] T. J. Arruda, A. S. Martinez, and F. A. Pinheiro, "Electromagnetic energy and negative asymmetry parameters in coated magneto-optical cylinders: Applications to tunable light transport in disordered systems," *Phys. Rev. A*, vol. 94, p. 033825, 2016.

[46] Y. Huang, Y. Shen, C. Min, and G. Veronis, "Switching photonic nanostructures between cloaking and superscattering regimes using phase-change materials [Invited]," *Opt. Mat. Expr.*, vol. 8, pp. 1672–1685, 2018.

[47] W. Liu, "Superscattering pattern shaping for radially anisotropic nanowires," *Phys. Rev. A*, vol. 96, p. 023854, 2017.

[48] S. I. Valvis, A. K. Ram, K. Hizanidis, P. Papagiannis, A. Papadopoulos, A. Zisis, I. G. Tigelis, and E. Glytsis, "Scattering of radio frequency waves by cylindrical filaments with general orientation relative to the magnetic field," *J. Plasma Phys.*, vol. 84, p. 745840604, 2018.

[49] A. K. Ram and K. Hizanidis, "Scattering of radio frequency waves by cylindrical density filaments in tokamak plasmas," *Phys. Plasmas*, vol. 23, p. 022504, 2016.

[50] W. J. M. Kort-Kamp, F. S. S. Rosa, F. A. Pinheiro, and C. Farina, "Tuning plasmonic cloaks with an external magnetic field," *Phys. Rev. Lett.*, vol. 111, p. 215504, 2013.

[51] H. W. Wu, F. Wang, Y. Q. Dong, F. Z. Shu, K. Zhang, R. W. Peng, X. Xiong, and M. Wang, "Cavity modes with optical orbital angular momentum in a metamaterial ring based on transformation optics," *Opt. Expr.*, vol. 23, pp. 32087–32097, 2015.

[52] K. Vynck, D. Felbacq, E. Centeno, A. I. Căbuz, D. Cassagne, and B. Guizal, "All-dielectric rod-type metamaterials at optical frequencies," *Phys. Rev. Lett.*, vol. 102, p. 133901, 2009.

[53] Y. I. Chizhevskaya and S. P. Skobelev, "Comparative features of cylindrical electromagnetic black holes with positive and negative refractive indexes," in *European Conference on Antennas and Propagation EuCAP 2019*, (Krakow), pp. 1–5, 31 March–5 April 2019.

[54] H. Wang and L. Chen, "A cylindrical optical black hole using graded index photonic crystals," *J. Appl. Phys.*, vol. 109, p. 103104, 2011.

[55] W. Lu, J. Jin, Z. Lin, and H. Chen, "A simple design of an artificial electromagnetic black hole," *J. Appl. Phys.*, vol. 108, p. 064517, 2010.

[56] A. V. Kildishev, L. J. Prokopeva, and E. E. Narimanov, "Cylinder light concentrator and absorber: theoretical description," *Opt. Express*, vol. 18, pp. 16646–16662, 2010.

[57] Q. Cheng, T. J. Cui, W. X. Jiang, and B. G. Cai, "An omnidirectional electromagnetic absorber made of metamaterials," *New J. Phys.*, vol. 12, p. 063006, 2010.

[58] J. R. Wait, "Some boundary value problems involving plasma media," *J. Res. Nat. Bur. Stand.*, vol. 65B, pp. 137–150, 1961.

[59] J. C. Palais, "Scattering from a gyrotropic cylinder," *IEEE Trans. Antennas Propag.*, vol. 11, pp. 505–506, 1963.

[60] N. Okamoto, "Matrix formulation of scattering by a homogeneous gyrotropic cylinder," *IEEE Trans. Antennas Propag.*, vol. 18, pp. 642–649, 1970.

[61] R. D. Graglia and P. L. E. Uslenghi, "Electromagnetic scattering from anisotropic materials, part i: General theory," *IEEE Trans. Antennas Propag.*, vol. 32, pp. 867 – 869, 1984.

[62] R. B. Wu and C. H. Chen, "Variational reaction formulation of scattering problem for anisotropic dielectric cylinders," *IEEE Trans. Antennas Propag.*, vol. AP-34, pp. 640–645, 1986.

[63] J. C. Monzon and N. J. Damaskos, "Two-dimensional scattering by a homogeneous anisotropic rod," *IEEE Trans. Antennas Propag.*, vol. AP-34, pp. 1243–1249, 1986.

[64] J. C. Monzon, "Three-dimensional scattering by an infinite homogeneous anisotropic circular cylinder: A spectral approach," *IEEE Trans. Antennas Propag.*, vol. 35, pp. 670–682, 1987.

[65] J. C. Monzon, "On a surface integral representation for homogeneous anisotropic regions: Two-dimensional case," *IEEE Trans. Antennas Propag.*, vol. 10, pp. 1401–1406, 1988.

[66] B. Beker and K. Umashankar, "Analysis of electromagnetic scattering by arbitrarily shaped two-dimensional anisotropic objects: combined field surface integral equation formulation," *Electromagnetics*, vol. 9, pp. 215–229, 1989.

[67] B. Beker, K. R. Umashankar, and A. Taflove, "Numerical analysis and validation of the combined field surface integral equations for electromagnetic scattering by arbitrarily shaped two-dimensional anisotropic objects," *IEEE Trans. Antennas Propag.*, vol. 37, pp. 1573–1581, 1989.

[68] B. Beker, K. R. Umashankar, and A. Taflove, "Electromagnetic scattering by arbitrarily shaped two-dimensional perfectly conducting objects coated with homogeneous anisotropic materials," *Electromagnetics*, vol. 10, pp. 387–406, 1990.

[69] J. Wu and K. A. Michalski, "Hybrid FEM-MFCM for 2-D scattering by inhomogeneous anisotropic material cylinders," *IEEE Trans. Magn.*, vol. 31, pp. 1558–1561, 1995.

[70] Z. N. Chen, W. Hong, and W. X. Zhang, "Application of FD-MEI to electromagnetic scattering from transversally anisotropic inhomogeneous cylinders," *IEEE Trans. Electromagn. Compat.*, vol. 40, pp. 103–110, 1998.

[71] J. L. Tsalamengas, "Oblique scattering from radially inhomogeneous dielectric cylinders: An exact Volterra integral equation formulation," *J. Quant. Spectr. Rad. Trans.*, vol. 213, pp. 62–73, 2018.

[72] K. Wang, J.-J. Laurin, and K. Wu, "Two-dimensional scattering from ho-

mogenous anisotropic cylinders using a multifilament current method," *IEEE Trans. Antennas Propag.*, pp. 1–11, 2020. Accepted for publication.

[73] P. M. Morse and H. Feshbach, *Methods of Theoretical Physics.* New York: McGraw-Hill, 1953.

[74] G. P. Zouros and G. C. Kokkorakis, "Electromagnetic scattering by an inhomogeneous gyroelectric sphere using volume integral equation and orthogonal Dini-type basis functions," *IEEE Trans. Antennas Propag.*, vol. 63, pp. 2665–2676, 2015.

[75] G. P. Zouros and G. C. Kokkorakis, "Electromagnetic scattering by a general rotationally symmetric inhomogeneous anisotropic sphere," *IEEE Trans. Microw. Theory Techn.*, vol. 63, pp. 3054–3065, 2015.

[76] C.-T. Tai, *Dyadic Green's Functions in Electromagnetic Theory.* New York: IEEE, 1994.

[77] W. C. Chew, *Waves and Fields in Inhomogeneous Media.* New York: Van Nostrand Reinhold, 1990.

[78] G. Han, Y. Han, and H. Zhang, "Relations between cylindrical and spherical vector wavefunctions," *J. Opt. A: Pure Appl. Opt.*, vol. 10, p. 015006, 2008.

[79] C. A. Balanis, *Advanced Engineering Electromagnetics.* New York: John Wiley & Sons, Inc., 1989.

[80] A. D. Greenwood and J.-M. Jin, "A field picture of wave propagation in inhomogeneous dielectric lenses," *IEEE Antennas Propag. Mag.*, vol. 41, pp. 9–18, 1999.

[81] G. N. Watson, *A Treatise on the Theory of Bessel Functions.* Cambridge, England: Cambridge University Press, 1958.

[82] S. B. Sharma, V. K. Singh, and S. Chakrabarty, "Multifrequency waveguide orthomode transducer," *IEEE Trans. Microw. Theory Techn.*, vol. 53, pp. 2604–2609, Aug. 2005.

[83] S. Cogollos, M. Brumos, V. E. Boria, C. Vicente, J. Gil, B. Gimeno, and M. Guglielmi, "A systematic design procedure of classical dual-mode circular waveguide filters using an equivalent distributed model," *IEEE Trans. Microw. Theory Techn.*, vol. 60, pp. 1006–1017, 2012.

[84] H. Hu, K. L. Wu, and R. J. Cameron, "Stepped circular waveguide dual-mode filters for broadband contiguous multiplexers," *IEEE Trans. Microw. Theory Techn.*, vol. 61, pp. 139–145, 2013.

[85] Q. X. Chu, D. Y. Mo, and Q. S. Wu, "An isolated radial power divider via circular waveguide TE_{01}-mode transducer," *IEEE Trans. Microw. Theory Techn.*, vol. 63, pp. 3988–3996, 2015.

[86] A. Alù and N. Engheta, "Guided modes in a waveguide filled with a pair of single-negative (SNG), double-negative (DNG), and/or double-positive (DPS) layers," *IEEE Trans. Microw. Theory Techn.*, vol. 52, pp. 199–210, 2004.

[87] J. G. Pollock and A. K. Iyer, "Below-cutoff propagation in metamaterial-lined circular waveguides," *IEEE Trans. Microw. Theory Techn.*, vol. 61, pp. 3169–3178, 2013.

[88] J. G. Pollock and A. K. Iyer, "Miniaturized circular-waveguide probe antennas using metamaterial liners," *IEEE Trans. Antennas Propag.*, vol. 63, pp. 428–433, 2015.

[89] N. Raveu, B. Byrne, L. Claudepierre, and N. Capet, "Modal theory for waveguides with anisotropic surface impedance boundaries," *IEEE Trans. Microw.*

Theory Techn., vol. 64, pp. 1153–1162, 2016.

[90] T. B. MacA and H. C. Minnett, "Modes of propagation in cylindrical waveguides with anisotropic walls," *IEE Proc.*, vol. 125, pp. 929–932, 1978.

[91] Z. Luo, T. J. Cui, and H. F. Ma, "Cutoff manipulation of anisotropic reactance lining in circular waveguides," *Int. J. Microw. Wirel. Technol.*, vol. 11, pp. 334–340, 2018.

[92] V. I. Shcherbinin, B. A. Kochetov, A. V. Hlushchenko, and V. I. Tkachenko, "Cutoff frequencies of a dielectric-loaded rectangular waveguide with arbitrary anisotropic surface impedance," *IEEE Trans. Microw. Theory Techn.*, vol. 67, pp. 577–583, 2019.

[93] V. Lombardi, M. Bozzi, and L. Perregrini, "An improved meshless method for waveguide eigenvalue problems," *IEEE Microw. Wireless Compon. Lett.*, vol. 27, pp. 1047–1049, 2017.

[94] V. Lombardi, M. Bozzi, and L. Perregrini, "A novel variational meshless method with radial basis functions for waveguide eigenvalue problems," *IEEE Trans. Microw. Theory Techn.*, vol. 66, pp. 3714–3723, 2018.

[95] T. C. K. Rao, "Propagation characteristics of a circular waveguide coated inside with a metamaterial," *Int. J. Elect.*, vol. 94, pp. 935–942, 2007.

[96] V. Lombardi, M. Bozzi, and L. Perregrini, "Evaluation of the dispersion diagram of inhomogeneous waveguides by the variational meshless method," *IEEE Trans. Microw. Theory Techn.*, vol. 67, pp. 2105–2113, 2019.

[97] E. J. Rothwell and L. L. Frasch, "Propagation characteristics of dielectric rod-loaded waveguides," *IEEE Trans. Microw. Theory Techn.*, vol. 36, pp. 594–600, 1988.

[98] S. P. Yeo, "Application of least-squares boundary residua method to the analysis of a circular waveguide loaded with a nonconcentric dielectric rod," *IEEE Trans. Microw. Theory Techn.*, vol. 38, pp. 1092–1095, 1990.

[99] J. A. Roumeliotis, A. B. M. Siddique Hossain, and J. G. Fikioris, "Cutoff wavenumbers of eccentric circular and concentric circular-elliptic metallic waveguides," *Radio Sci.*, vol. 15, pp. 923–937, 1980.

[100] A. D. Kotsis and J. A. Roumeliotis, "Cutoff wavenumbers of eccentric circular metallic waveguides," *IET Microw. Antennas Propag.*, vol. 8, pp. 104–111, 2014.

[101] M. Gholizadeh, M. Baharian, and F. H. Kashani, "A simple analysis for obtaining cutoff wavenumbers of an eccentric circular metallic waveguide in bipolar coordinate system," *IEEE Trans. Microw. Theory Techn.*, vol. 67, pp. 837–844, 2019.

[102] M. Gholizadeh and F. H. Kashani, "A new analytical method for calculating the cutoff frequencies of an eccentrically dielectric-loaded circular waveguide," *IEEE Microw. Wireless Compon. Lett.*, vol. 30, pp. 453–456, 2020.

[103] R. P. Owens, J. E. Aitken, and T. C. Edwards, "Quasi-static characteristics of microstrip on an anisotropic sapphire substrate," *IEEE Trans. Microw. Theory Techn.*, vol. 24, pp. 499–505, 1976.

[104] N. G. Alexopoulos and C. M. Krowne, "Characteristics of single and coupled microstrips on anisotropic substrates," *IEEE Trans. Microw. Theory Techn.*, vol. 26, pp. 387–393, 1978.

[105] D. M. Pozar, "Radiation and scattering from a microstrip patch on a uniaxial substrate," *IEEE Trans. Antennas Propag.*, vol. 35, pp. 613–621, 1987.

[106] A. M. A. E. Sherbiny, "Hybrid mode analysis of microstrip lines on anisotropic substrates," *IEEE Trans. Microw. Theory Techn.*, vol. 29, pp. 1261–1266, 1981.

[107] N. G. Alexopoulos, "Integrated-circuit structures on anisotropic substrates," *IEEE Trans. Microw. Theory Techn.*, vol. 33, pp. 847–851, 1985.

[108] H. Xu, Z. Wang, J. Hao, J. Dai, L. Ran, J. A. Kong, and L. Zhou, "Effective-medium models and experiments for extraordinary transmission in metamaterial-loaded waveguides," *Appl. Phys. Lett.*, vol. 92, p. 041122, 2008.

[109] R. Marques, J. Martel, F. Mesa, and F. Medina, "Left-handed-media simulation and transmission of em waves in subwavelength split-ring-resonator-loaded metallicwaveguides," *Phys. Rev. Lett.*, vol. 89, p. 183901, 2002.

[110] N. J. Damaskos, R. B. Mack, A. L. Maffett, W. Parmon, and P. L. E. Uslenghi, "The inverse problem for biaxial materials," *IEEE Trans. Microw. Theory Techn.*, vol. 32, pp. 400–405, 1984.

[111] M. Norgren and S. He, "Reconstruction of the constitutive parameters for an/spl omega/material in a rectangular waveguide," *IEEE Trans. Microw. Theory Techn.*, vol. 43, pp. 1315–1321, 1995.

[112] J. B. Davies, "Propagation in rectangular waveguide filled with skew uniaxial dielectric," *IEEE Trans. Microw. Theory Techn.*, vol. 15, pp. 372–376, 1967.

[113] K. Sun, J. K. Lee, and J. W. Graham, "Fields and wave modes analysis of rectangular waveguide filled with uniaxial medium," *IEEE Trans. Microw. Theory Techn.*, vol. 64, pp. 3429–3440, 2016.

[114] K. S. Champlin and G. H. Glover, ""Twist" modes in magnetoplasma-filled circular waveguides," *IEEE Trans. Microw. Theory Techn.*, vol. MTT-18, pp. 566–570, 1970.

[115] B. J. Hu and C. L. Ruan, "Propagation properties of a plasma waveguide in an external magnetic field," *J. Phys. D*, vol. 31, pp. 2151–2154, 1998.

[116] S. Liu, L. W. Li, M. S. Leong, and T. S. Yeo, "Theory of gyroelectric waveguides," *PIER*, vol. 29, pp. 231–259, 2000.

[117] H. J. Kuno and W. D. Hershberger, "Microwave Faraday effect and propagation in a circular solid-state plasma waveguide," *IEEE Trans. Microw. Theory Techn.*, vol. MTT-15, pp. 661–668, 1967.

[118] V. I. Shcherbinin, G. I. Zaginaylov, and V. I. Tkachenko, "Analogy between circular core-cladding and impedance waveguides and their membrane functions," *PIER*, vol. 53, pp. 111–120, 2017.

[119] K. Katsinos, G. P. Zouros, and J. A. Roumeliotis, "An entire domain CFVIE-CDSE method for EM scattering on electrically large highly inhomogeneous gyrotropic circular cylinders," *IEEE Trans. Antennas Propag.*, 2020. Accepted for publication. DOI: 10.1109/TAP.2020.3026860.

[120] G. P. Zouros, "Analysis of multilayered gyroelectric spherical cavities by weak form VIE formulation," *IEEE Trans. Microw. Theory Techn.*, vol. 65, pp. 4029–4036, 2017.

[121] G. D. Kolezas and G. P. Zouros, "Eigenfrequencies in gyrotropic-metallic cavities," *IEEE Microw. Compon. Lett.*, vol. 28, pp. 197–199, 2018.

[122] J.-M. L. Floch, Y. Fan, G. Humbert, Q. Shan, D. Férachou, R. Bara-Maillet, M. Aubourg, J. G. Hartnett, V. Madrangeas, D. Cros, J.-M. Blondy, J. Krupka, and M. E. Tobar, "Invited article: Dielectric material characterization techniques and designs of high-q resonators for applications from micro to

millimeter-waves frequencies applicable at room and cryogenic temperatures," *Rev. Sci. Instr.*, vol. 85, p. 031301, 2014.

[123] A. B. Matsko and V. S. Ilchenko, "Optical resonators with whispering-gallery modes-Part I: Basics," *IEEE J. Sel. Topics Quantum Electron.*, vol. 12, pp. 3–14, 2006.

[124] A. B. Matsko and V. S. Ilchenko, "Optical resonators with whispering-gallery modes-Part II: Applications," *IEEE J. Sel. Topics Quantum Electron.*, vol. 12, pp. 15–32, 2006.

[125] L. He, Ş. K. Özdemir, and L. Yang, "Whispering gallery microcavity lasers," *Laser Photon. Rev.*, vol. 7, pp. 60–82, 2013.

[126] J. R. Wait, "Electromagnetic whispering gallery modes in a dielectric rod," *Radio Sci.*, vol. 2, pp. 1005–1017, 1967.

[127] J. Zhang and D. Grischkowsky, "Whispering-gallery-mode cavity for terahertz pulses," *J. Opt. Soc. Am. B*, vol. 20, pp. 1894–1904, 2003.

[128] S. Deng, W. Cai, and V. N. Astratov, "Numerical study of light propagation via whispering gallery modes in microcylinder coupled resonator optical waveguides," *Opt. Expr.*, vol. 12, pp. 6468–6480, 204.

[129] S. V. Boriskina, T. M. Benson, P. Sewell, and A. I. Nosich, "Effect of a layered environment on the complex natural frequencies of two-dimensional WGM dielectric-ring resonators," *J. Lightwave Technol.*, vol. 20, pp. 1563–1572, 2002.

[130] A. V. Boriskin and A. I. Nosich, "Whispering-gallery and Luneburg-lens effects in a beam-fed circularly layered dielectric cylinder," *IEEE Trans. Antennas Propag.*, vol. 50, pp. 1245–1249, 2002.

[131] K. Okazaki, T. Shimogaki, K. Fusazaki, M. Higashihata, D. Nakamura, N. Koshizaki, and T. Okada, "Ultraviolet whispering-gallery-mode lasing in ZnO micro/nano sphere crystal," *Appl. Phys. Lett.*, vol. 101, p. 211105, 2012.

[132] R. S. Moirangthem and A. Erbe, "Interfacial refractive index sensing using visible-excited intrinsic zinc oxide photoluminescence coupled to whispering gallery modes," *Appl. Phys. Lett.*, vol. 103, p. 051108, 2013.

[133] M. Ornigotti and A. Aiello, "Theory of anisotropic whispering-gallery-mode resonators," *Phys. Rev. A*, vol. 84, p. 013828, 2011.

[134] J. A. Haigh, S. Langenfeld, N. J. Lambert, J. J. Baumberg, A. J. Ramsay, A. Nunnenkamp, and A. J. Ferguson, "Magneto-optical coupling in whispering-gallery-mode resonators," *Phys. Rev. A*, vol. 92, p. 063845, 2015.

[135] X. Zhang, N. Zhu, C.-L. Zou, and H. X. Tang, "Optomagnonic whispering gallery microresonators," *Phys. Rev. Lett.*, vol. 117, p. 123605, 2016.

[136] G. P. Zouros, "Full-wave theory for WGM lasing of fully anisotropic nanoparticles," *J. Appl. Phys.*, vol. 124, p. 174301, 2018.

[137] J. Carbonell, A. Díaz-Rubio, D. Torrent, F. Cervera, M. A. Kirleis, A. Piqué, and J. Sánchez-Dehesa, "Radial photonic crystal for detection of frequency and position of radiation sources," *Sci. Rep.*, vol. 2, p. 558, 2012.

[138] J. Carbonell, D. Torrent, and J. Sánchez-Dehesa, "Radial photonic crystal shells and their application as resonant and radiating elements," *IEEE Trans. Antennas Propag.*, vol. 61, pp. 755–767, 2013.

[139] W. Liu, A. E. Miroshnichenko, and Y. S. Kivshar, "q-factor enhancement in all-dielectric anisotropic nanoresonators," *Phys. Rev. B*, vol. 94, p. 195436, 2016.

[140] M. E. Tobar and A. G. Mann, "Resonant frequencies of higher order modes in cylindrical anisotropic dielectric resonators," *IEEE Trans. Microw. Theory Techn.*, vol. 39, pp. 2077–2082, 1991.

[141] A. Díaz-Rubio, J. Carbonell, D. Torrent, and J. Sánchez-Dehesa, "Low-Q whispering gallery modes in anisotropic metamaterial shells," *Phys. Rev. B*, vol. 88, p. 115118, 2013.

[142] C. C. Lam, P. T. Leung, and K. Young, "Explicit asymptotic formulas for the positions, widths, and strengths of resonances in Mie scattering," *J. Opt. Soc. Am. B*, vol. 9, pp. 1585–1592, 1992.

[143] E. Almpanis, G. P. Zouros, and N. Papanikolaou, "Spherical optomagnonic resonators," in *Optomagnonic Structures: Novel Architectures for Simultaneous Control of Light and Spin Waves* (E. Almpanis, ed.), ch. 6, Singapore: World Scientific Publishing Co Pte Ltd, 2020.

[144] M. Abramowitz and I. A. Stegun, *Handbook of Mathematical Functions*. New York: Dover, 1972.

[145] J. A. Stratton, *Electromagnetic Theory*. New York: McGraw-Hill, 1941.

[146] R. P. Brent, *Algorithms for Minimization without Derivatives*. New Jersey: Prentice-Hall, 1973.

[147] G. P. Zouros, "CCOMP: An efficient algorithm for complex roots computation of determinantal equations," *Comput. Phys. Comm.*, vol. 222, pp. 339–350, 2018.

[148] D. E. Müller, "A method of solving algebraic equations using an automatic computer," *Mathematical Tables and Other Aids to Computation*, vol. 10, pp. 208–215, 1956.

[149] J. R. Probert-Jones, "Resonance component of backscattering by large dielectric spheres," *J. Opt. Soc. Am. B*, vol. 1, pp. 822–830, 1984.